Fundamental Models for Fuel Cell Engineering

Chao-Yang Wang*

Departments of Mechanical Engineering and Materials Science and Engineering, Electrochemical Engine Center (ECEC), The Pennsylvania State University, University Park, Pennsylvania 16802

Contents

* To whom correspondence should be addressed. E-mail: cxw31@psu.edu.

1. Introduction

Owing to their high energy efficiency, low pollution, and low noise, fuel cells are widely regarded as 21st century energy-conversion devices for mobile, stationary, and portable power. Through tremendous progress made in the past decade, currently available fuel cell materials appear to be adequate for near-term markets with highest cost entry points. As a result, industries are currently placing their focus on fuel cell design and engineering for better performance, improved durability, cost reduction, and better cold-start characteristics. This new focus has led to an urgent need for identification, understanding, prediction, control, and optimization of various transport and electrochemical processes that occur on disparate length scales in fuel cells.

The purpose of the present review is to summarize the current status of fundamental models for fuel cell engineering and indicate where this burgeoning field is heading. By choice, this review is limited to hydrogen/air polymer electrolyte fuel cells (PEFCs), direct methanol fuel cells (DMFCs), and solid oxide fuel cells (SOFCs). Also, the review does not include microscopic, first-principle modeling of fuel cell materials, such as proton conducting membranes and catalyst surfaces. For good overviews of the latter fields, the reader can turn to Kreuer,[1] Paddison,[2] and Koper,[3] for example.

The review is organized as follows. Section 2 defines a systematic framework for fuel cell modeling research, called computational fuel cell dynamics (CFCD), and outlines its four essential elements. Sections 3−5 review work performed in the past decade on PEFCs, DMFCs, and SOFCs, respectively. Future research needs and directions of the three types of fuel cells are pointed out wherever applicable and summarized separately at the end of each section.

2. Computational Fuel Cell Dynamics

Fuel cell science and technology cuts across multiple disciplines, including materials science, interfacial science, transport phenomena, electrochemistry, and catalysis. Because of the diversity and complexity of electrochemical and transport phenom-

Figure 1. Local current density profiles along a straight-channel fuel cell as predicted by the same computer model for two cases differing only in two model parameters.[6]

Chao-Yang Wang received his Ph.D. degree in Mechanical Engineering from the University of Iowa in 1994, and he is currently a Professor of Mechanical Engineering and Materials Science & Engineering at The Pennsylvania State University. He has been the founding director of the Penn State Electrochemical Engine Center (ECEC) since 1997. His research interests include fundamental modeling and experimental diagnostics of various fuel cell/battery systems and their materials.

ena involved in a fuel cell and occurring at disparate length and time scales, fuel cell modeling and simulation requires a systematic framework parallel to computational fluid dynamics (CFD), here termed computational fuel cell dynamics (CFCD). CFCD deals with the coupling of multidimensional transport phenomena with electrochemical kinetics and the transport of charge (electrons and ions) to provide a comprehensive understanding of fuel cell dynamics. CFCD is envisioned to consist of (1) physicochemical model development, (2) advanced numerical algorithms, (3) materials characterization, and (4) model validation at detailed levels.

Section 2.1 gives a generalized summary of fuel cell models, while section 2.2 discusses the need for employing large numerical meshes and hence advanced numerical algorithms for efficient fuel cell simulations. Section 2.3 briefly reviews the efforts, in the literature, to measure basic materials and transport properties as input to fuel cell models.

The need for the fourth element, i.e., model validation against detailed distribution data, has been increasingly acknowledged in the past few years.[4−6] This is because the global $I-V$ curve is largely inadequate to validate comprehensive CFCD models. This inadequacy can perhaps best be illustrated by a numerical experiment shown in Figure 1. In this experiment, a three-dimensional (3-D) PEFC model (as described in section 3.1) is applied to a single-channel fuel cell using Gore-Select 18 μm membrane with an anode/cathode stoichiometry of 3/2 and anode/cathode inlet relative humidity of 42%/0% at a cell temperature of 80 °C. Two cases are simulated using the same model for a cell voltage of 0.75 V. In Case 1, the ionic resistance in two catalyst layers is included, and the kinetic constant of oxygen reduction reaction (ORR) is estimated from the Pt loading. This case yields an average current density of 0.24 A/cm^2 at 0.75 V. In Case 2 (which is hypothetical), however, we neglect the ionic resistance in two catalyst layers (amounting to approximately twice that of the membrane) and then reduce the kinetic
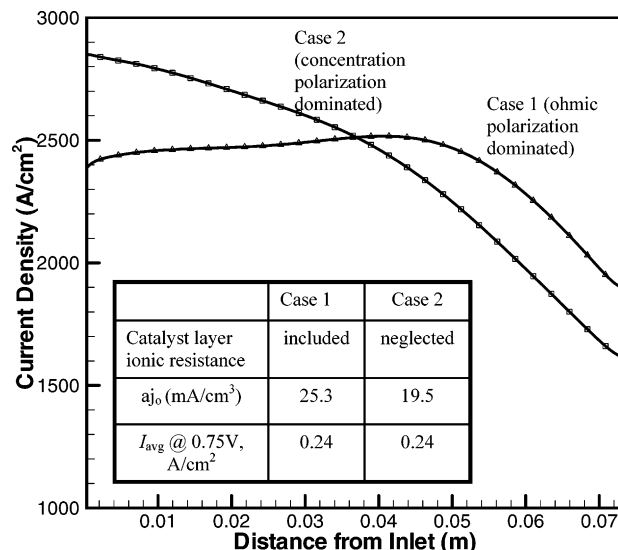
constant by 23%. By changing only two parameters (i.e., catalyst layer resistance and kinetic constant of ORR), Case 2 produces exactly the same average current density as Case 1, despite that the two cases fundamentally differ in limiting mechanisms. Case 1 is dominated more by ohmic polarization, thereby exhibiting a slight increase in the local current density near the dry inlet as the membrane becomes more hydrated, and a fall only close to the outlet where oxygen depletion starts to take control. On the other hand, Case 2 is dominated more by concentration polarization with little ohmic loss. As a result, the current distribution in Case 2 closely follows the decline of oxygen concentration due to the stoichiometric effect. Literature efforts involving detailed diagnostics aiming to create benchmark-quality data for CFCD model validation are reviewed in section 3.8 for the PEFC system.

2.1. CFCD Model Equations

A fundamental fuel cell model consists of five principles of conservation: mass, momentum, species, charge, and thermal energy. These transport equations are then coupled with electrochemical processes through source terms to describe reaction kinetics and electro-osmotic drag in the polymer electrolyte. Such convection−diffusion−source equations can be summarized in the following general form

$$\frac{\partial(\rho\phi)}{\partial t} + \nabla(\rho v \phi) = \nabla(\Gamma\nabla\phi) + S \qquad (1)$$

where ϕ is a general variable to be solved, ρ the density, v the velocity vector, Γ the diffusion coefficient, and S a source term which includes all terms that cannot be included in the previous terms. For instance, the Darcy's drag exerted on gas flow through porous electrodes of fuel cells is typically accounted for through a source term in the momentum equation. The electro-osmotic drag of water

through a polymer electrolyte can also be formulated as a source term in the water species equation since it differs from conventional mechanisms of transport by diffusion and convection and arises only from an electrochemical system.

Setting $\phi = 1$, the above general transport equation is reduced to

$$\frac{\partial \rho}{\partial t} + \nabla(\rho v) = S_m \tag{2}$$

This equation is usually referred to as the continuity equation or mass conservation equation.[7] The source term, S_m, in the continuity equation is commonly caused by mass consumption or production from electrochemical reactions as well as mass loss/gain through phase transformation.

Main source terms prevailing in most transport equations for a fuel cell model are due to electrochemical reactions occurring in the electrode comprised of three phases: electronic (s), electrolyte (e), and gas (g). Electrochemical reactions occur at the triple-phase boundary according to the following general formula

$$\sum_k s_k M_k^z = ne^- \tag{3}$$

where the summation is over all species involved in a reaction. M_k is a chemical symbol for species k participating in the electrochemical reaction, z and s are the charge number and stoichiometric coefficient of the species, and n is the number of electrons transferred in the reaction. The values of s_k, z, and n can readily be determined by comparing a specific electrode reaction to this general form. For example, for the oxygen reduction reaction, $2H_2O - O_2 - 4H^+ = 4e^-$, one has that $s_{H_2O} = 2$, $s_{O_2} = -1$, $s_{H^+} = -4$, and $n = 4$.

The volumetric production rate of species k due to electrochemical reaction occurring at the triple-phase boundary is given by Faraday's law

$$S_k = -\frac{s_k j}{nF} \tag{4}$$

with

$$j = ai_o\left[\exp\left(\frac{\alpha_a F}{RT}\eta\right) - \exp\left(-\frac{\alpha_c F}{RT}\eta\right)\right] \tag{5}$$

where j is the volumetric transfer current of the reaction, a is the electrochemically active area per unit of electrode volume, i_o is the exchange current density, α_a and α_c are the anodic and cathodic transfer coefficients, respectively, F is Faraday's constant, R is the universal gas constant, and T is the cell temperature. Equation 5, commonly known as the Butler–Volmer equation, describes a large class of electrode reactions.[8] Under facile and sluggish kinetics, the Butler–Volmer equation is further reduced to linear and Tafel expressions, respectively.

The exchange current density for a reaction, i_o, depends strongly on the compositions and temperature at the reaction interface. The surface over-potential for an electrochemical reaction, η, is defined as

$$\eta = \Phi_s - \Phi_e - U_o \tag{6}$$

where Φ_s and Φ_e are the electric potentials of the electronic phase and electrolyte, respectively, at the triple-phase interface. The last term in eq 6, U_o, is the thermodynamic equilibrium potential of the reaction, which is, in turn, a function of the reactant and product concentrations at the interface as generally expressed by the Nernst equation. Note that the surface overpotential, η, represents the driving force for an electrochemical reaction.

2.2. Computational Aspects

2.2.1. General

The advection–diffusion equation with a source term can be solved by CFD algorithms in general. Patankar[9] provided an excellent introduction to numerical fluid flow and heat transfer. Oran and Boris[10] discussed numerical solutions of diffusion–convection problems with chemical reactions. Since fuel cells feature an aspect ratio of the order of 100, O(100), the upwind scheme for the flow-field solution is applicable and proves to be very effective.[9] Unstructured meshes are commonly employed in commercial CFD codes.

2.2.2. Solution Algorithms for Coupled Potential Equations

A numerical problem unique to the modeling of electrochemical systems in general and fuel cells in particular is the strong coupling between the potentials for the electronic and electrolyte phases. The two potential equations are dependent on each other through the reaction current, where the surface overpotential appears in the exponential terms of Butler–Volmer kinetics. Advanced iterative algorithms are required in order to ensure efficient and converging solutions.[8,11–13] It appears that the most efficient technique is to solve the two discretized algebraic equations *simultaneously* using Newton's method.[8,11] For one-dimensional problems, such a direct solution method results in the often-used Band-J subroutine developed by Newman[8] in the 1960s, in which the Jacobian matrix resulting from Newton's procedure is inverted using LU factorization in each Newton iteration. However, the direct solution is computationally inefficient for a large sparse Jacobian matrix arising from two- and three-dimensional problems. Recently, Wu et al.[11] presented a set of modern numerical algorithms to efficiently solve the two strongly coupled potential equations. A Krylov iterative solver, the generalized minimal residual subroutine (GMRES), was used instead of the direct solver (Gauss elimination) to improve solution efficiency of the large, nonsymmetric Jacobian system. In addition, a nonlinear Gauss–Seidel method provided the initial guess for the Newton iteration, and the GMRES solver was preconditioned with a block Gauss–Seidel and multigrid algorithm with a smoother based on the tridiagonal matrix algorithm (TDMA).
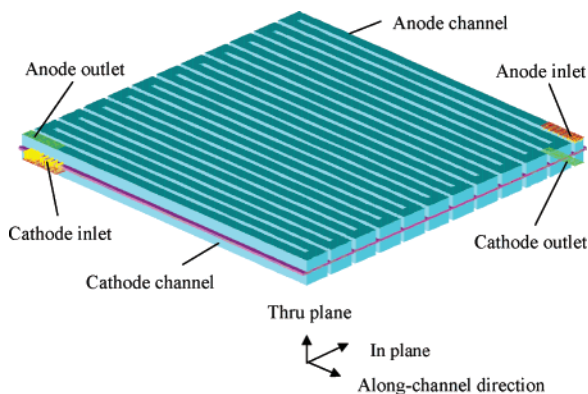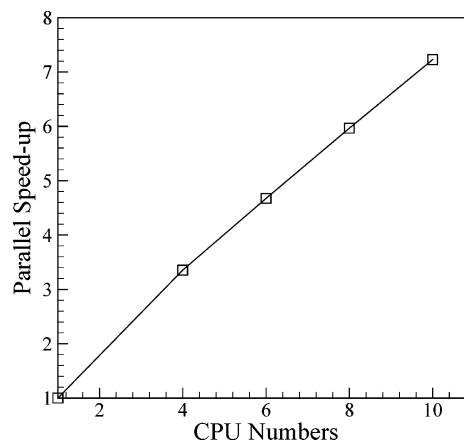
Figure 2. PEFC configuration for numerical modeling.

Figure 3. Speedup of a massively parallelized PEFC model.[15]

Within the framework of commercial CFD codes where sequential solution methods are standard, as they need to solve a number of user-specified transport equations, the two potential equations must then be solved through innovative source term linearization.[14]

2.2.3. Mesh Requirement and Parallel Computing

Another computational challenge in fuel cell modeling is the need for large meshes for simulation of industrial-scale cells. To fully appreciate the large mesh required, consider a typical geometry of a large-scale PEFC displayed in Figure 2, where the anode flow field (top) and cathode flow field (bottom) sandwich a membrane−electrode assembly (MEA) with two gas diffusion layers (GDL). Let us define the through-plane direction to be perpendicular to the MEA, the along-channel direction to be of gas flow, and the in-plane direction to be across channels through the land area. Suppose that 6−8 grid points are needed to sufficiently resolve each of the five distinctive regions of MEA and two GDLs, with 10 grid points needed in each of the two gas channels, the minimum number of grid points in the through-plane dimension is thus between 50 and 60. In the along-channel direction, 100 grid points are typically required since fuel cell channels are long and exhibit a large aspect ratio (>100). In the in-plane direction, 10 nodal points are needed for a channel and a land, respectively, thus giving rise to 20 grid points per channel within a flow field. For large-scale fuel cells featuring 20−60-channel flow field, a mesh consisting of 2−6 million grid points is needed.

The majority of numerical work published to date has used no more than a few hundred thousand grid points; that is, there is still 1 order of magnitude gap existing between the current computational capability and that required for high-fidelity PEFC simulation. Meng and Wang[15] made one of the first attempts to bridge this gap by developing a massively parallel computational methodology based on an efficient domain decomposition method. The computational domain is divided into a number of subdomains along the flow direction. Each subdomain is assigned to one processor with proper load balancing. Each processor computes and stores variable solutions within its own subdomain with necessary interactions on subdomain boundaries through communication between proces-

sors. As a fuel cell features a minimal degree of interactions between subdomains along the flow direction, this problem is inherently suited for parallel computing with low communication cost. Benchmark calculations were carried out in a Linux PC cluster comprised of 50 processors of 1.4 GHz AMD Athlon Thunderbird CPU and 512 MB DDR SDRAM. A local 100 Mbps switched Ethernet network was used for message communication. Figure 3 displays the computational performance of the PC cluster, demonstrating greater than 7× speed-up by 10 CPUs running the massively parallelized PEFC model. Roughly 300 iterations are needed for a typical case run, requiring about 1.5 h of computational time using 10 CPUs. This clearly demonstrates the effectiveness of parallel computing in reducing actual computing time for these intensive simulations.

Large-scale calculations using 1−10 million computational cells are presently being carried out in several industrial and academic organizations using the parallel computing method and multiprocessor computers; see section 3.6 for further detail.

2.3. Material Property Characterization

The importance of materials characterization in fuel cell modeling cannot be overemphasized, as model predictions can be only as accurate as their material property input. In general, the material and transport properties for a fuel cell model can be organized in five groups: (1) transport properties of electrolytes, (2) electrokinetic data for catalyst layers or electrodes, (3) properties of diffusion layers or substrates, (4) properties of bipolar plates, and (5) thermodynamic and transport properties of chemical reactants and products.

The most important electrolyte property is ionic conductivity. For the PEFC system, water and proton transport in the polymer electrolyte occurs concurrently. Springer et al.[16] correlated the proton conductivity (in S/cm) in the polymer membrane with its water content as follows

$$\kappa_e = \exp\left[1268\left(\frac{1}{303} - \frac{1}{T}\right)\right](0.005139\lambda - 0.00326) \quad (7)$$

The strong dependence of electrolyte conductivity on
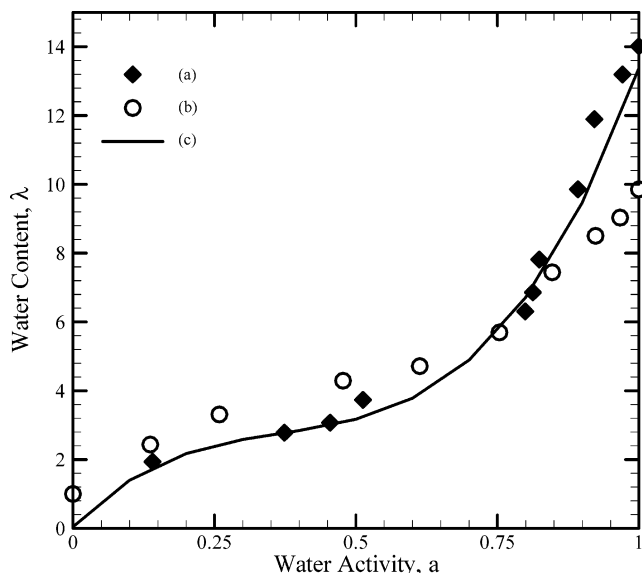
Figure 4. Equilibrium water uptake curve for Nafion membrane: (a) measurement at 30 °C,[18] (b) measurement at 80 °C,[17] (c) Springer's expression, eq 8.

Figure 5. Electro-osmotic drag coefficient and water diffusivity as functions of water content in Nafion membranes.[23,27]

water content is evident from the above correlation. Several studies[17−22] have been carried out to define the relation between membrane water content and moisture of the surrounding environment, called the water uptake curve as shown in Figure 4. Zawodzinski et al.[17,18] measured water content of membranes immersed in liquid water and membranes exposed to water vapor at variable activities. It is seen that there is a discontinuity in the membrane water content between equilibration of the membrane with liquid water and with saturated water vapor, both of which correspond to unit water activity. This phenomenon, called "Schröeder's paradox", is observed in a wide variety of polymer/solvent combinations. Water content in the membrane (i.e., the number of H_2O molecules per sulfonic group), λ, depends on the water activity, a, according to the following fit of the experimental data[16]
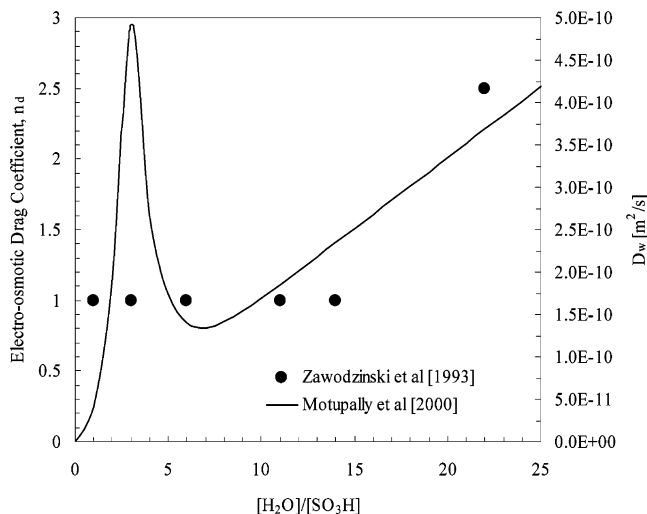
$$\lambda = \begin{cases} 0.043 + 17.81a - 39.85a^2 + 36.0a^3 & \text{for } 0 < a \leq 1 \\ 14 + 1.4(a - 1) & \text{for } 1 \leq a \leq 3 \end{cases} \tag{8}$$

where the water activity is in turn calculated by the ratio of the water partial pressure to the saturated pressure, corresponding to the cell temperature, T. Apparently, the water activity and water content all vary spatially; thus, the proton conductivity κ_e also varies throughout the membrane and catalyst layer. In the catalyst layer, the effective proton conductivity is further modified by Bruggmann factor based on the ionomer content

$$\kappa_e^{\text{eff}} = \epsilon_e^{1.5}\kappa_e \tag{9}$$

where ϵ_e is the ionomer volume fraction.

Two other important electrolyte properties for the PEFC system are the water diffusion coefficient and electro-osmotic drag coefficient. These two param-

eters dictate the water content profile within the membrane and thus design of a proper water management scheme for the fuel cell. Water content dependence of diffusion coefficient and electro-osmotic drag coefficient has also been extensively studied.[23−27] Figure 5 indicates that the electro-osmotic drag coefficient is roughly a constant at unity when $\lambda < 14$ and then linearly increases for water content between 14 and 22. The water diffusion coefficient in the membrane is highly nonlinear and shows a distinctive peak at $\lambda \approx 3$. The nonlinearity in membrane-transport properties excludes analytical solutions and increases the level of difficulty in numerical solutions.

Kreuer[1] presented an excellent discussion of materials and transport properties of proton conducting membranes other than Nafion.

The most important electrokinetic data pertinent to fuel cell models are the specific interfacial area in the catalyst layer, a, the exchange current density of the oxygen reduction reaction (ORR), i_o, and Tafel slope of ORR. The specific interfacial area is proportional to the catalyst loading and inversely proportional to the catalyst layer thickness. It is also a strong function of the catalyst layer fabrication methods and procedures. The exchange current density and Tafel slope of ORR have been well documented in refs 28−31.

Diffusion medium properties for the PEFC system were most recently reviewed by Mathias et al.[32] The primary purpose of a diffusion medium or gas diffusion layer (GDL) is to provide lateral current collection from the catalyst layer to the current collecting lands as well as uniform gas distribution to the catalyst layer through diffusion. It must also facilitate the transport of water out of the catalyst layer. The latter function is usually fulfilled by adding a coating of hydrophobic polymer such as poly(tetrafluoroethylene) (PTFE) to the GDL. The hydrophobic polymer allows the excess water in the cathode catalyst layer to be expelled from the cell by gas flow in the channels, thereby alleviating flooding. It is known that the electric conductivity of GDL is

typically an order of magnitude higher in the in-plane direction than the through-plane direction due to the strong anisotropy of GDL fibrous structures. By analogy between electric and heat conduction, it can be expected that the thermal conductivity of GDL exhibits the same degree of anisotropy. Pore size distribution, porosity, and gas permeability were characterized by Mathias et al., albeit without compression, which should add a strong effect on the GDL-transport properties. In addition, the interfacial wetting property, both in the interior and on the surface of porous GDL, was recognized as an important material property of GDL. Mathias et al.[32] and Lim and Wang[33] independently performed surface contact angle measurements, based on variants of the capillary rise method. Lim and Wang[33] further reported a strong temperature dependence of water contact angle on GDL, thereby establishing a link to the realistic thermal environment in an operating PEFC. The literature, however, lacks experimental data on the porosity and permeability of GDL under compression or more broadly the quantification of GDL deformation under stress and subsequently GDL structure−flow interactions.

Three properties of the current collector plate are particularly important for CFCD models. One is electric conductivity, the second is thermal conductivity, and the third is surface wettability. These properties for materials such as graphite and metals are well documented in standard textbooks.

The species diffusivity, D_k, varies in different subregions of a PEFC depending on the specific physical phase of component k. In flow channels and porous electrodes, species k exists in the gaseous phase and thus the diffusion coefficient corresponds with that in gas, whereas species k is dissolved in the membrane phase within the catalyst layers and the membrane and thus assumes the value corresponding to dissolved species, usually a few orders of magnitude lower than that in gas. The diffusive transport in gas can be described by molecular diffusion and Knudsen diffusion. The latter mechanism occurs when the pore size becomes comparable to the mean free path of gas, so that molecule-to-wall collision takes place instead of molecule-to-molecule collision in ordinary diffusion. The Knudsen diffusion coefficient can be computed according to the kinetic theory of gases as follows

$$D_{K,k} = \frac{2}{3}\left(\frac{8RT}{\pi M_k}\right)^{1/2} r_p \qquad (10)$$

where r_p is the mean pore radius and M_k the molecular weight of the diffusing gas.

The binary diffusion coefficient, $D_{i,k}$, can be either experimentally measured or calculated using the Chapman−Enskog equation.[34] The dependence of the diffusion coefficient on temperature and pressure is generally given by[7]

$$D_{i,k}(T,p) = D_{i,k,0}\left(\frac{T}{T_o}\right)^{3/2}\left(\frac{p_o}{p}\right) \qquad (11)$$

The combined diffusivity of species k in gas, due to

ordinary and Knudsen diffusion, is then calculated from

$$D_k = \left(\frac{1}{D_{K,k}} + \frac{1}{D_{i,k}}\right)^{-1} \qquad (12)$$

In the PEFC system, the mean pore radii of catalyst layers are of the order of 0.1 μm. The Knudsen diffusion coefficients at 80 °C for O_2 and H_2O through the catalyst layer are thus estimated to be 0.32 and 0.43 cm²/s, respectively. These values are comparable to the respective ordinary diffusion coefficients, indicating that Knudsen diffusion further restricts the rates of oxygen and water transport through the cathode catalyst layer in PEFCs and should be taken into account.

Thermodynamic and transport properties of liquids relevant to the DMFC system can be found in Reid et al.[35]

Key material properties for SOFC, such as the ionic conductivity as a function of temperature, are available in refs 36−39. In addition, Todd and Young[40] compiled extensive data and presented estimation methods for the calculation of diffusion coefficients, thermal conductivities, and viscosities for both pure components and mixtures of a wide variety of gases commonly encountered in SOFCs. Another excellent source of transport properties for gases and mixtures involved in a SOFC is the CHEMKIN thermodynamic database.[41]

3. Polymer Electrolyte Fuel Cells

Polymer electrolyte fuel cells (PEFC) are considered the most promising alternative power plant for transportation because of their high efficiency, low emissions, low operation temperature, and low noise. In the past decade, significant improvements have been achieved in PEFC technology, including improved MEA technology and lowered platinum catalyst loading. Excellent reviews of hydrogen PEFC research up to the mid-1990s were presented by Prater[42] and Gottesfeld and Zawodzinski,[30] and new advances were reported in the most recent compilation of Vielstich et al.[43]

Much effort has been expended in the last 5 years upon development of numerical models with increasingly less restrictive assumptions and more physical complexities. Current development in PEFC modeling is in the direction of applying computational fluid dynamics (CFD) to solve the complete set of transport equations governing mass, momentum, species, energy, and charge conservation.

Modeling and computer simulation of PEFC began with the pioneering work of Bernardi and Verbrugge[44,45] and Springer et al.,[46,47] whose models are essentially one-dimensional. Fuller and Newman,[48] Nguyen and White,[49] and Yi and Nguyen[50,51] subsequently developed pseudo-two-dimensional models accounting for compositional changes along the flow path. While such models are useful for small cells, their applicability to large-scale fuel cells, particularly under high fuel utilization and low humidity conditions, is limited. Nevertheless, the one-dimensional models of Bernardi and Verbrugge[44,45] and

Springer et al.[46,47] provided a fundamental framework to build multidimensional, multiphysics models that followed. The pseudo-two-dimensional models developed by Fuller and Newman,[48] Nguyen and White,[49] and later Yi and Nguyen[50,51] further demonstrated the important roles played by water and heat management in maintaining high performance of PEFCs. Effects of anisotropy and inhomogeneity on mass transport through GDL were also numerically investigated.[52,53]

Gurau et al.[54] presented a two-dimensional model of transport phenomena in PEFC. This work illustrated the utility of a multidimensional model in the understanding of the internal conditions of a fuel cell, such as the reactant and water distributions. In a separate development, Yi and Nguyen[50,51] formulated a two-dimensional model to explore hydrodynamics and multicomponent transport in the air cathode of PEFC with an interdigitated flow field. The concept of modeling PEFC within the CFD framework was proposed shortly thereafter.[55−58] Two-dimensional simulations of coupled electrochemical and transport processes were carried out in using a CFD code,[55] and the three-dimensional version of the same model was also demonstrated.[56,59] Independently, Dutta et al.[57] presented three-dimensional simulation of PEFC using Fluent, a commercial CFD package. Subsequent work was presented in Dutta et al.[58] and Lee et al.[60] In the model of Dutta et al.[57,58] and Lee et al.,[60] the membrane electrode assembly (MEA) is not included in the computational domain but rather simplified as an interface without thickness. As such, water transport and ohmic potential drop across the membrane are treated using simplified linear relationships as in the early work of Nguyen and White.[49]

Additional work on general-purpose, fully three-dimensional CFCD models was performed by Zhou and Liu[61] using an in-house CFD code, Berning et al.[62] using the commercial package CFX, and Mazumder and Cole[63] using the commercial package CFD-ACE+. Most recently, both STAR−CD and Fluent packages have been applied to large-scale fuel cell modeling through their user-coding capability.[6,14,15,64−67] Sections 3.1−3.7 will review these works in more detail as well as in the context of various important issues pertinent to the PEFC system.

Efforts have also been made to model two-phase flow and transport in a PEFC, a critical but difficult issue that has repeatedly been emphasized in the literature. To treat liquid water formation in a PEFC, there are two types of models. The simplest approach is a single-phase model in which the gas and liquid are considered a single-fluid mixture and thus share the same velocity field. Also, the interfacial tension effect is completely ignored. In this case, the total amount of water can be obtained by solving a single equation without distinguishing water vapor from liquid water. Once the total water concentration field is obtained, one may allow for the water concentration going beyond the saturation level, essentially assuming supersaturation in the gas phase.[16,55,59] Alternately, one can truncate the water concentration

at the gas saturation level and account for the extra water in the form of liquid water in a postprocessing manner.[57,58,60] Sections 3.1−3.6 are devoted to reviewing this class of single-phase models.

The more rigorous approach to liquid water transport is a true two-phase model in which the two phases travel at different velocities. At the same time, the interfacial tension effect and GDL wettability, essential for successful PEFC operation, are fully accounted for. The work of Wang et al.,[68] Nguyen et al.,[69−71] You and Liu,[72] Mazumder and Cole,[73] Berning and Djilali,[74] and Pasaogullari and Wang[67,75] falls into this category. These two-phase models are reviewed in section 3.7.

Another classification of PEFC models is in terms of volume-averaged (i.e., macrohomogeneous) models or pore-level models. Macroscopic models assume local interfacial equilibrium, namely, electrical, chemical, and thermal equilibrium at the pore level. Conditions of validity of local interfacial equilibrium were carefully defined.[76] All of the above-cited CFCD models are, strictly speaking, macroscopic models, although theoretical inconsistency may exist in some work. In the two-phase models of Nguyen et al.,[69−71] Mazumder and Cole,[63] and Berning and Djilali,[62] the water condensation/evaporation rate was expressed according to the local nonequilibrium condition of water vapor in the gas phase, but such a treatment was merely a numerical trick without physical significance. All simulation results in these works virtually corresponded to the local chemical equilibrium condition. Moreover, no dispersion effect arising from the interaction of local fluctuations in velocity and species concentration at the pore level was included in their water vapor transport equation, indicative of an equilibrium macroscopic model. It is interesting to note that a different approach to treating phase change was used for related problems such as drying of porous materials,[77,78] steam injection for enhanced oil recovery, and groundwater contamination and remediation.[79]

In the following section we will present first a general single-phase model along with detailed discussions on several critical issues in PEFC modeling (i.e., sections 3.1−3.6). This is followed by two-phase modeling of liquid water transport in section 3.7. In section 3.8 we will describe experimental diagnostics which can be used to probe the validity of such models as well as identify future modeling needs. Finally, in section 3.9 we will review work on pore-level modeling of the PEFC catalyst layer.

3.1. Single-Phase Conservation Equations

Various forms of governing equations have been used in PEFC modeling, although all fall under the single-phase assumption. To clarify important subtleties with theoretical rigor, in this subsection we summarize a set of conservation equations and provide detailed comments of various terms that should be used.

The single-phase model described herein considers the total water amount without distinguishing liquid water from water vapor. This approach is valid under the condition that liquid saturation within the gas
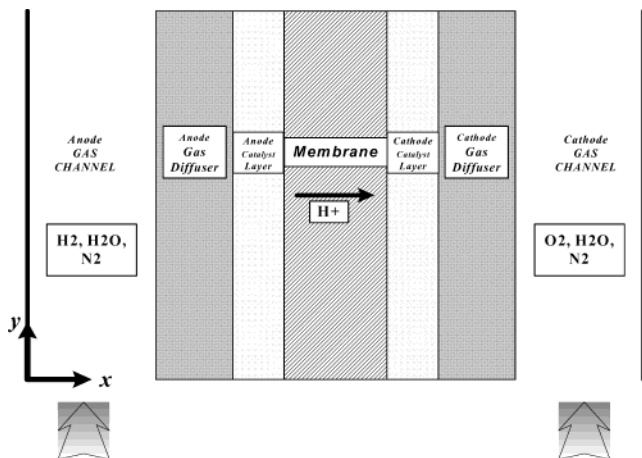
Figure 6. Schematic diagram of a polymer electrolyte fuel cell.

diffusion layer (GDL) is low (e.g., lower than the irreducible liquid saturation s_{ir}) or liquid droplets are small and disperse in gas flow to form a mist flow. This approach is particularly well suited for fuel cell simulations under low humidity operation, a major application of single-phase models.

The fuel cell to be modeled is schematically shown in Figure 6 and divided into seven subregions: the anode gas channel, anode GDL, anode catalyst layer (CL), ionomeric membrane, cathode CL, cathode GDL, and cathode gas channel. The present model considers the anode feed consisting either of hydrogen, water vapor, and nitrogen or hydrogen/water binary gas, whereas humidified air is fed into the cathode channel. Hydrogen oxidation and oxygen reduction reactions are considered to occur only within the active catalyst layers where Pt/C catalysts are intermixed uniformly with recast ionomer.

As explained in section 2, a fundamental PEFC model consists of five principles of conservation: mass, momentum, species, electric charge, and thermal energy. These five balance equations are now summarized in Table 1 with their source terms identified for various regions of a fuel cell. The central idea of this model is to employ a single set of governing equations in all regions throughout a fuel cell. The main assumptions invoked in the model are (1) ideal gas mixtures and (2) incompressible and laminar gas flow due to small pressure gradients and Reynolds numbers. More explanation of each of the five conservation equations follows.

In the mass and momentum equations for both gas channels and GDL, the superficial velocity is used in order to automatically ensure the normal mass

flux continuity at the channel/GDL interface. In addition, the permeability in the membrane is assumed to be very small, say 10^{-30} m^2, which effectively renders the fluid velocity zero. The momentum source term represents Darcy's drag for flow through a porous medium, which reduces the momentum equation to the Navier–Stokes equation in gas channels, where $K \rightarrow \infty$, and to Darcy's law in GDL and catalyst layers when K is small.

There is a nonzero mass source in the continuity equation, S_m, arising from the summation of all species equations. A general form of this source term is given in Table 1. Use has been made of the assumption that summation of interspecies diffusion within the gas phase is equal to zero. Specifically, one has

$$S_m =$$
$$\begin{cases} -M_{H_2}\dfrac{j}{2F} + M_{H_2O}\left[\nabla(D_{w,m}\nabla C_{H_2O}) - \nabla\left(n_d\dfrac{i_e}{F}\right)\right] \\ \qquad\qquad\qquad\qquad\qquad \text{in anode CL} \\[4pt] M_{O_2}\dfrac{j}{4F} - M_{H_2O}\dfrac{j}{2F} + M_{H_2O}\left[\nabla(D_{w,m}\nabla C_{H_2O}) - \nabla\left(n_d\dfrac{i_e}{F}\right)\right] \\ \qquad\qquad\qquad\qquad\qquad \text{in cathode CL} \end{cases}$$
$$(13)$$

In the above, $D_{w,m}$ is the water diffusion coefficient through the membrane phase only. Note also that the water fluxes through the membrane phase, via electro-osmotic drag and molecular diffusion, represent a source/sink term for the gas mixture mass in the anode and cathode, respectively.

The general species equation can be applied to three species, H$_2$, O$_2$, and H$_2$O, with nitrogen being the remaining species of the gas mixture. The species concentration of N$_2$ can thus be simply calculated from the fact that all species mole fractions sum up to be unity. Species diffusion can be modeled by Fick's law, which is exact for binary gases but a good approximation for multicomponent gases.[53,80] The electro-osmotic drag coefficient, n_d, is only relevant to the water molecule; thus, its values for other species such as H$_2$ and O$_2$ are set to zero.

To close the equation set for mass, momentum, and species conservation, one needs the ideal gas law that describes the gas density varying with its compositions. That is

$$\rho = \sum M_k C_k \qquad (14)$$

where the N$_2$ molar concentration can be calculated

Table 1. Single-Phase PEFC Model: Governing Equations with Source Terms Identified in Various Regions[a]

| | conservation equations | source terms | | |
		diffusion layers	catalyst layers	membrane
mass	$\partial(\epsilon\rho)/\partial t + \nabla(\rho\vec{u}) = S_m$		$S_m = \sum_k M_k S_k + M_{H_2O}\nabla(D_{w,m}\nabla C_{H_2O})$	
momentum	$1/\epsilon[\partial(\rho\vec{u})/\partial t + 1/\epsilon\nabla(\rho\vec{u}\vec{u})] = -\nabla p + \nabla\tau + S_u$	$S_u = (-\mu/K)\vec{u}$	$S_u = (-\mu/K)\vec{u}$	$\vec{u} = 0$
species	$\partial(\epsilon C_k)/\partial t + \nabla(\vec{u} C_k) = \nabla(D_k^{eff}\nabla C_k) + S_k$		$S_k = -\nabla[(n_d/F)i_e] - (s_k j/nF)$	$S_k = -\nabla[(n_d/F)i_e]$
charge	$\nabla(\kappa^{eff}\nabla\Phi_e) + S_\Phi = 0$		$S_\Phi = j$	
	$\nabla(\sigma^{eff}\nabla\Phi_s) - S_\Phi = 0$			
energy	$\partial[(\rho c_p)_m T]/\partial t + \nabla(\rho c_p \vec{u}T) = \nabla(k^{eff}\nabla T) + S_T$		$S_T = j[\eta + T(dU_o/dT)] + (i_e^2/\kappa^{eff})$	$S_T = i_e^2/\kappa^{eff}$

[a] Electrochemical reaction $\sum_k s_k M_k^z = ne^-$, where $M_k \equiv$ chemical formula of species k, $s_k \equiv$ stoichiometry coefficient, and $n \equiv$ number of electrons transferred. In PEM fuel cells there are (anode) H$_2$ − 2H$^+$ = 2e$^-$ and (cathode) 2H$_2$O − O$_2$ − 4H$^+$ = 4e$^-$.

by $C_{N_2} = p/RT - C_{H_2O} - C_{O_2}$ (or C_{H_2}). In the case of H_2/H_2O binary gas in the anode, the H_2 species transport equation does not need to be solved; instead, its concentration is calculated by $C_{H_2} = p/RT - C_{H_2O}$.

Note that the single-phase model described above fully couples the mass, momentum, and species conservation equations through various source terms. One elegant simplification of this full model is to neglect the mass source term in the continuity equation and assume a constant gas density in the momentum equation. The approximation of constant density is well supported by the study of Dutta et al.,[58] which predicted a density variation smaller than 5% using a variable-density model, as seen in Figure 7. This simplification thus yields decoupling of the flow field from the species, electric potential, and temperature fields, thereby significantly accelerating the calculations. Possible inaccuracy introduced by this splitting of the problem may occur on the anode side; however, the hydrogen concentration profile is relatively unimportant as the anode overpotential is typically negligible. Therefore, under common operating conditions, this reduced model yields <10% and 14% error in the current distribution for anode stoichiometries of 2.0 and 1.2, respectively.[81] In addition to reducing memory and computational requirements, this splitting of the fuel cell problem has the added advantage of allowing for consideration of different cell voltages/current densities for the same flow field.

The charge-transport equation includes the electrochemical kinetics for both anode and cathode catalyst layers. If we assume an infinitely large electric conductivity of the electronic phase, the electrode becomes an equipotential line, such that

$$\Phi_s = 0 \text{ on the anode}$$

$$\Phi_s = V_{cell} \text{ on the cathode}$$

If the electric conductivity of electrode matrixes and plates is limited, an additional equation governing charge transport in the electronic phase would have to be solved. This issue is separately addressed in section 3.4.

The source term in the charge equation is used to describe the transfer current between the electronic and electrolyte phases inside of each anode and cathode catalyst layer. The transfer current densities are expressed as follows

$$\text{anode: } j = ai_{o,a}^{ref}\left(\frac{C_{H_2}}{C_{H_2,ref}}\right)^{1/2}\left(\frac{\alpha_a + \alpha_c}{RT}F\eta\right) \quad (15)$$

$$\text{cathode: } j = -ai_{o,c}^{ref}\left(\frac{C_{O_2}}{C_{O_2,ref}}\right)\exp\left(-\frac{\alpha_c}{RT}F\eta\right) \quad (16)$$

These kinetic expressions represent the hydrogen oxidation reaction (HOR) in the anode catalyst layer and oxygen reduction reaction (ORR) in the cathode catalyst layer, respectively. These are simplified from the general Butler−Volmer kinetics, eq 5. The HOR
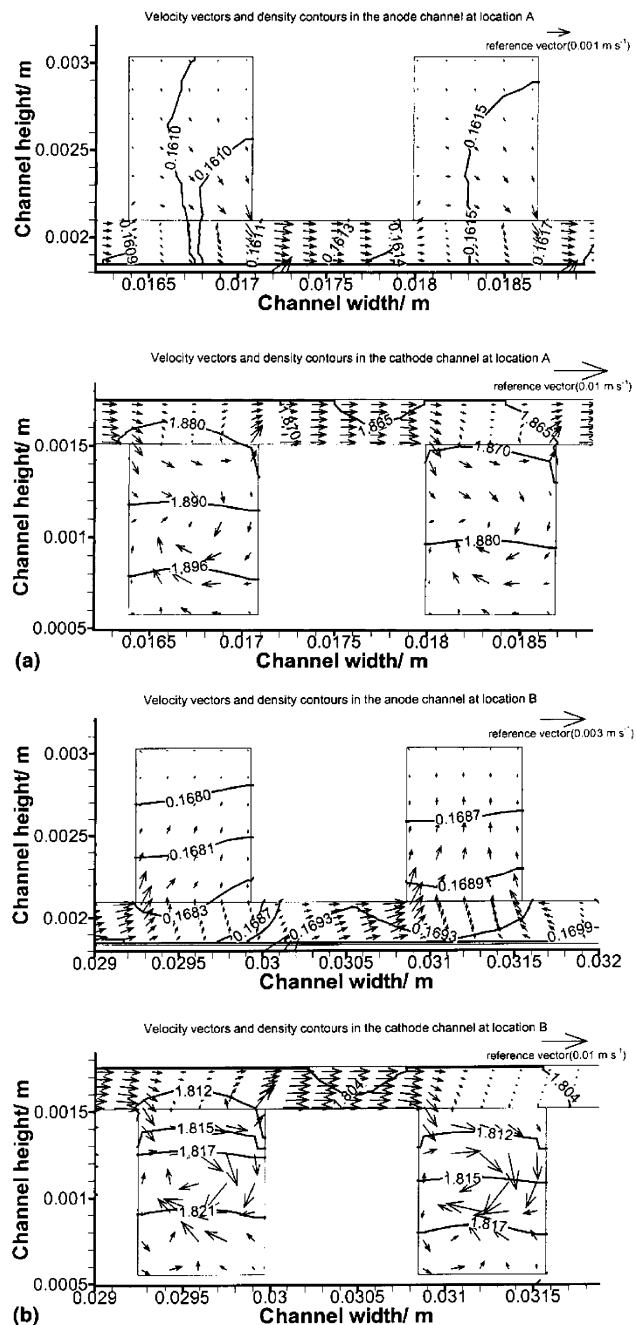
Figure 7. Velocity vectors and gas density contours under very low humidity operation: (a) in the middle and (b) at the exit of a 10 cm² PEFC.[58]

kinetic expression is derived by linearizing the Butler−Volmer equation on the assumption that the HOR reaction is facile and hence the surface overpotential is small. On the other hand, the ORR kinetic reaction is slow, causing high overpotential. Therefore, the ORR kinetic expression is obtained by neglecting the anodic reaction term of the Butler−Volmer equation. It should be noted that the ORR is assumed to be the first-order reaction based on early experimental work of Bernardi and Verbrugge[45] and Gottesfeld and Zawodzinski.[30] The value of $(\alpha_a + \alpha_c)$ in HOR kinetics should be equal to 2, while $\alpha_c = 1$ in ORR corresponds to a Tafel slope of approximately 60 mV/decade. The thermodynamic equilibrium po-

tentials of anode and cathode are assumed to be zero and a function of temperature, respectively, as[82]

$$U_o = 1.23 - 0.9 \times 10^{-3}(T - 298.15) + \frac{RT}{2F}\left(\ln p_{H_2} + \frac{1}{2}\ln p_{O_2}\right) \quad (17)$$

This equilibrium open-circuit potential for a H_2/air fuel cell is calculated from thermodynamic data of reaction enthalpy and entropy changes.

The energy equation entails a detailed account of heat generation due to irreversible heat of the electrochemical reaction, reversible (or entropic) heat, and Joule heating.[83] The heat generation term in a CFCD model must be unambiguous and location specific. More discussion is deferred to section 3.3. In addition, the heat accumulation in a porous material consisting of the matrix and fluid is given by

$$(\rho c_p)_m = \epsilon(\rho c_p) + (1 - \epsilon)(\rho c_p)_s \quad (18)$$

where the heat capacitance (ρc_p) without subscript refers to the fluid and with subscript "s" refers to the solid matrix.

Six coupled governing equations listed in Table 1 are valid in all regions of a PEFC, and fluxes at an internal boundary between two adjacent regions are automatically continuous. Such a single-domain model is well suited for CFD implementation. In contrast, multidomain models, such as the one developed by Dutta et al.,[57,58] compute separate solutions for the anode and cathode subdomains, respectively, and then patch the two solutions through the water transport flux across the MEA interface. Numerically, this model is characterized as a solver-in-solver situation.

3.2. Water Transport

Water management is one of the most critical and widely studied issues in PEFC. Water management is referred to as balancing membrane hydration with flooding avoidance. These are two conflicting needs: to hydrate the polymer electrolyte and to avoid flooding in porous electrodes and GDL for reactant/product transport.

Early modeling studies[16,44,48,49,54,55,57,84,85] have focused on fully humidified fuel/air streams, which ensures a hydrated ionomer membrane, thus yielding a constant proton conductivity and the least ohmic loss. Under those full humidification conditions, however, the gas inside the fuel cell becomes oversaturated and water condensation may occur on the cathode side even at low operating current densities. The ensuing cathode flooding by liquid water subsequently hampers the access of oxygen to the cathode catalyst layer, resulting in a significant concentration polarization. In addition, full humidification of the reactant gases externally requires additional parasitic volume and power in a fuel cell system. Therefore, the recent trend in the industry is to operate PEFC under low humidity conditions while still maintaining an adequately hydrated polymer membrane. Such low humidity operating strategies will
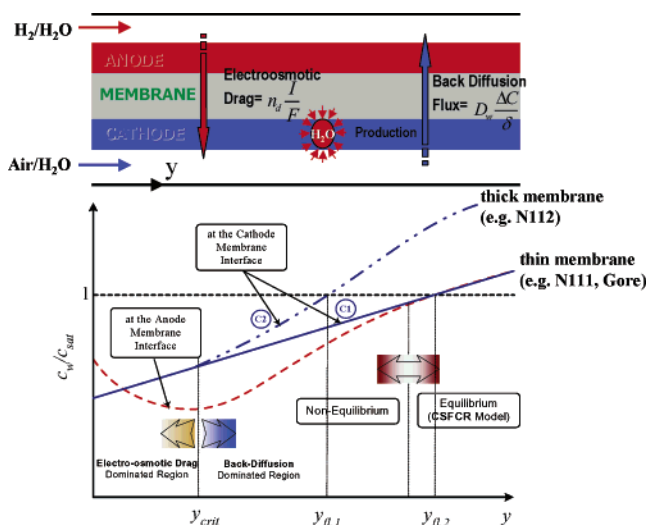
Figure 8. Two-dimensional sketch of water management in a PEM fuel cell whereby the membrane−electrode assembly separates the anode feed channel from the cathode, and a diagram of water uptake profiles in anode and cathode channels.

also reduce cathode flooding and volume as well as cost of the external humidifier. Obviously, this operating regime hinges upon a good understanding of water generation, transport, and distribution within PEFCs.

General features of water transport in a PEFC under low humidity operation is schematically shown in Figure 8. Water is produced in the cathode catalyst layer as a result of ORR or can be brought into the cell by humidified reactant gases represented by anode/cathode inlet relative humidity. Through the electrolyte between the anode and cathode, two modes of water transport are operative: the electro-osmotic drag effect and diffusion driven by the concentration gradient. The water flux due to the electro-osmotic drag is directly proportional to the protonic flux (I_{cell}/F). The diffusion flux of water in the membrane is usually described by a water diffusion coefficient and the gradient in molar concentration of water.

Typical water concentration profiles in the anode and cathode flow channels are also depicted in Figure 8. The water concentration at the anode/membrane interface first decreases along the flow and then reaches the minimal point at which the net water flux across the membrane becomes zero, implying that the electro-osmotic drag is balanced by the back-diffusion of water. Thus, this location also represents a boundary between drag- and diffusion-dominated regimes. The anode water concentration increases after this minimum point due to enhanced back-diffusion driven under a larger cathode water concentration resulting from ORR. On the cathode side, the water concentration profile can take two routes, depending on the membrane thickness. For thin membranes such as Nafion 111 or Gore membranes, water exchange between the anode and cathode via diffusion is so effective that both sides achieve equilibration sufficiently downstream. This is shown as curve C1 in Figure 8. However, thick membranes such as Nafion 112 will make the water concentrations on two sides

of the membrane further diverge, as shown as the curve C2 in Figure 8.

Figure 8 also nicely describes two possible scenarios for electrode flooding. Defining the onset of electrode flooding by the dimensionless water concentration reaching unity (i.e., gas becomes saturated), Figure 8 shows that both anode and cathode will be flooded by liquid water condensed from the gas for thin membranes, while for thick membranes only the cathode is susceptible to flooding.

Water-transport characteristics become quite intricate in low humidity PEFCs. For example, the variation in water concentration down the channel is pronounced as the cell is self-humidifying the inlet dry gases. The in-plane variation from channel to land is also substantial, giving rise to a fully three-dimensional distribution of water concentration. In addition, strong convection effect perpendicularly through the anode GDL, as induced by significant hydrogen consumption under low anode stoichiometry, challenges the conventional model based on diffusive transport. It seems that a comprehensive flow−transport−electrochemical coupled model is necessary to faithfully capture the water-transport characteristics in low humidity PEFCs.

Considerable efforts have been expended in the literature to simulate water management in PEFCs. These studies can be grossly divided into three groups. One group is focused on the physics of water transport and scrutinizes water transport through the polymer membrane. Notable work includes Springer et al.,[16] Fuller and Newman,[48] Nguyen and White,[49] Futerko and Hsing,[21] Hsing and Futerko,[86] Janssen,[87] and Kulikovsky.[80] Springer et al.[16] first introduced a diffusion model for Nafion 117 membrane and included the electro-osmotic drag term as well. They assumed equilibrium between the gas phase and the membrane phase of water in the Nafion membrane and then determined the membrane water content at the interface by the activity of water vapor. Hsing and Futerko[86] developed a two-dimensional finite element model for a PEFC without external humidification of the inlet gas streams. Flow field was approximated using the potential flow equation with a stream function. The membrane water content at the anode/membrane interface was calculated under the assumption of phase equilibrium between the vapor and membrane phases, and the cathode/membrane interface was assumed to be fully hydrated. More recently, Janssen[87] demonstrated 1-D and 2-D numerical models to account for water transport through the MEA under various humidification conditions of inlet gases. The computed results were compared with experimental data of Janssen and Overvelde.[88] In the model of Janssen,[87] it was assumed that the cell current density is constant everywhere, and the catalyst layers were excluded in the water-transport calculation. Reacting species along the channel and in the through-plane direction were calculated based on the one-dimensional mass-transport assumption. Kulikovsky[80] presented a multidomain model of water transport in which the diffusion and electro-osmotic drag coefficients through the polymer membrane are taken as

nonlinear functions of water content. It was found that the nonlinearity of the transport properties leads to the dryness on the anode side of the membrane, in accordance with the experimental observations of Buchi and Scherer.[89] While this group of models is fundamental in nature and reveals rich physics of water distribution through the polymer membrane, it is unable to capture all intricate features of water transport in a low humidity PEFC.

The second group attempted to model water transport throughout an entire fuel cell using the CFD approach.[62,63,90] These CFD models do not appear to properly model water transport through the polymer membrane. Berning et al.[62] indicated that no water diffusion in the membrane is included in their model, and thus it is restricted only to conditions with fully hydrated membranes. The single-phase model of Mazumder and Cole[63] used neither a water diffusion coefficient nor a drag coefficient in the membrane and therefore is expected to completely ignore any water transport across the membrane. Obviously, this group of models is unable to describe water-transport phenomena through the membrane in the single-phase regime (e.g., low humidity).

The last group of studies[55,57−59,91] strived to unite different modes of water transport in various parts of a PEFC and develop a comprehensive water-transport model that is both reflective of correct physics, particularly the water transport through the membrane by diffusion and electro-osmotic drag, as well as easy to implement for an entire cell using the CFD approach. This group of models is capable of simulating water management scenario in low humidity cells. Note that the model of Dutta et al.[57,58] uses an approximate analytical solution for water transport through the membrane by assuming a constant diffusion coefficient and drag coefficient and then embeds it into numerical solutions to the anode and cathode sides separately. This approach eliminates the MEA from the computational domain. However, such a model loses the ability to resolve increasingly important phenomena in MEA. For example, the ionic resistances in the two catalyst layers were treated by ad hoc assumption in this type of models. As PEFC technology moves toward the use of thinner membranes, the ionic resistance in the catalyst layer becomes important and comparable with that in the membrane and therefore must be accurately accounted for. In addition, a PEFC model treating the MEA as an interface without thickness essentially ignores the membrane water storage capacity and therefore cannot be used in simulating transient phenomena (see section 3.5).

In contrast, Wang and co-workers[55,56,59,91] developed a unified water-transport model applicable throughout a PEFC including the MEA region, thus enabling comprehensive CFCD simulations to be carried out. The model recognizes that there are different phases of water existing in various regions of the PEFC, i.e., water in the gas phase and in the membrane. As a result, phase equilibrium is considered and various modes of water transport, diffusion, convection, and electro-osmotic drag are incorporated in the unified
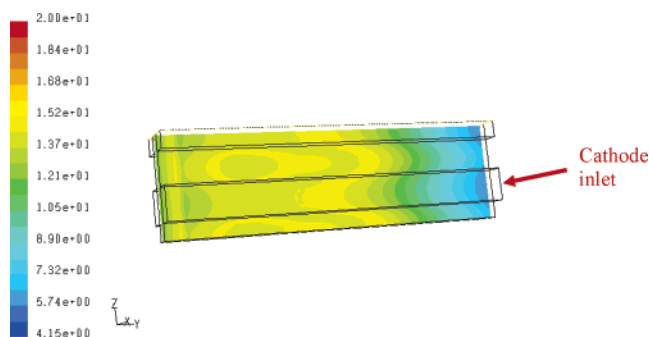
Figure 9. Membrane water content (λ) distribution in a three-straight channel fuel cell (only the half cell is shown due to symmetry) with anode and cathode counter-flow at 0.65 V or average current density of 1.1 A/cm^2. Anode and cathode feed conditions are humidification temperature = 50 °C, pressure = 2 atm, stoichiometry = 2, and the cell temperature = 80 °C.
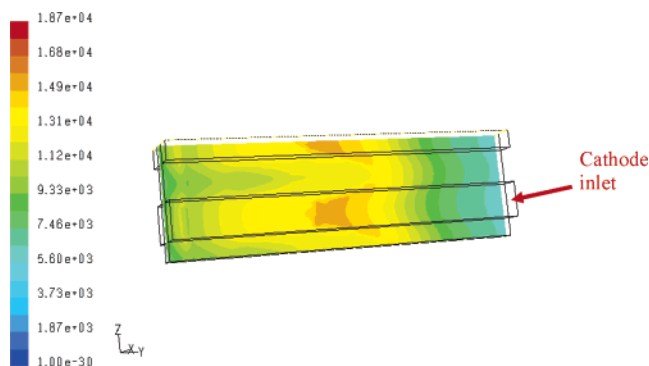
Figure 10. Current distribution (A/m^2) in a low humidity fuel cell at 0.65 V or average current density of 1.1 A/cm^2 with the same operating conditions as in Figure 9.

water-transport equation. A unified water-transport equation within the single-domain CFCD framework is developed with the aid of the equilibrium water uptake curve in the membrane phase. Details were provided by Um.[91] Figure 9 illustrates an example of membrane water content distribution for a low humidity, straight-channel cell with anode and cathode humidification temperatures equal to 50 °C for the 80 °C cell temperature. Figure 10 shows current distribution in the same cell.

Figure 11 displays calculation results of the current and water activity distributions in a 50 cm^2 fuel cell with serpentine flow field. The cell is operated under rather dry conditions with the anode and cathode relative humidity being 75% and 0, respectively. The line graphs are plotted along the center of the membrane in the cross-section, cutting through the middle of the cell. The simulation shown in Figure 11 exemplifies the present capability of a comprehensive water- and heat-transport model in providing fine details. It is clearly seen that the local current density varies from the channel to rib (or land) areas. Moreover, the current density above the rib is greater than the channel in the inlet portion of the fuel cell because the reactant gases are relatively dry and the ribs protect the membrane from losing water. In contrast, near the outlet portion of the fuel cell where gases become more humidified, the local current density begins to be controlled by oxygen transport,
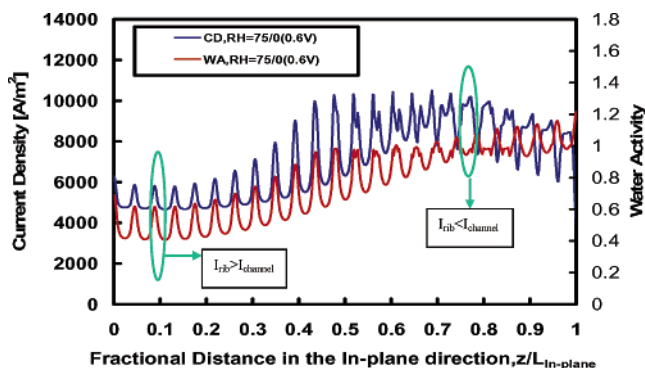
Figure 11. Current and water activity distributions in a low humidity 50 cm^2 fuel cell with serpentine flow field at 0.6 V or average current density of 0.71 A/cm^2. The membrane is 18 μm thick (EW < 1000). The anode/cathode feed conditions are pressure = 3/3 atm, relative humidity = 75%/dry, stoichiometry = 1.2/2, and cell temperature = 80 °C.

thereby showing a higher value in the channel area than the rib.

3.3. Heat Transport

A PEFC produces waste heat in an amount comparable to its electric power output (so that the energy-conversion efficiency is around 50%). Heat generation in PEFC stems from entropic heat of reactions, the irreversibility of the electrochemical reactions, and ohmic resistance (or Joule heating).[83] Roughly, the irreversible reaction heat, entropic heat, and Joule heating in a PEFC account for 55%, 35%, and 10% of total heat release, respectively. The last source of heat due to water condensation/evaporation will be discussed in section 3.7 as it is related to two-phase transport. In addition, the polymer membrane has low tolerance for temperature deviation from the operating point. Hydration of polymer membranes also strongly depends on the temperature as the water vapor saturation pressure is an exponential function of temperature. Thus, thermal management in PEFC is inherently coupled with water management and the two factors combine to ensure high performance and durability of a PEFC.

A number of PEFC thermal models have been published in the literature. Early efforts were made by Nguyen and White[49] and Fuller and Newman.[48] Nguyen and White[49] developed a two-dimensional PEFC model with one-dimensional heat transfer in the flow direction. The model considers phase change of water in the flow channel as the only heat source, allowing convective heat transfer between the gas and solid phases. On the other hand, Fuller and Newman[48] developed a pseudo-two-dimensional thermal PEFC model with one-dimensional mass transfer in the through-membrane direction and one-dimensional heat transfer in the flow direction. On the basis of the known enthalpy change of the overall electrochemical reaction, the model calculated the temperature rise of the flowing gas streams with various external heat transfer coefficients. However, in these early models the temperatures of membrane and electrodes were not differentiated, even though a significant temperature variation in those regions can

be expected in both the through-membrane and flow directions depending on the geometric and operating conditions. Furthermore, the major heat source terms, the entropic and irreversible reaction heats, were not specified in their models. Yi and Nguyen[50] extended Nguyen and White's[49] model to include the entropic and irreversible reaction heats along with the phase change heat. However, this model allowed the temperature variation of the solid phase in the flow direction only, assuming uniform temperature in the through-membrane direction.

Wöhr et al.[92] developed a one-dimensional thermal model for heat and mass transfer in the through-plane direction, particularly for PEFC stacks. Accounting for the entropic and irreversible reaction heats, they computed the temperature profile in the through-membrane direction and predicted the maximum temperature as a function of the number of cells contained in a stack. Rowe and Li[93] also developed a one-dimensional model in the through-membrane direction. Including entropic, irreversible, and phase change heats, they further took account of Joule heating in the membrane and anode/cathode catalyst layers. This work predicted the temperature variation in the through-membrane direction under the various current densities and electrode thermal conductivities. A major drawback of this model is the fact that the cathode catalyst layer is assumed to be fully hydrated and the membrane water content is linearly interpolated, indicating inapplicability of the model in low humidity operation.

Multidimensional thermal models were presented by many PEFC modeling groups. Maggio et al.[94] performed the pseudo-three-dimensional simulations, neglecting the temperature gradient in the flow direction. However they only considered the overall heat source term as $(U_o - V_{cell})I$. In the three-dimensional models developed by Shimpalee and Dutta[95] and Costamagna,[96] the heat source terms were also treated globally and not made location-specific. Berning et al.[62] presented a three-dimensional PEFC model including irreversible and entropic heat terms in the catalyst layers and Joule heating in the membrane. The main drawback of this model is assuming the membrane to be fully humidified, indicating limited applicability to low humidity operating conditions. Zhou and Liu[61] developed a three-dimensional PEFC model in which the entropic reaction heat (~35% of total heat) was ignored.

Accurate modeling of the temperature distribution in a PEFC requires accurate information in four areas: heat source, thermal properties of various components, thermal boundary conditions, and experimental temperature-distribution data for model validation. The primary mechanism of heat removal from the catalyst layers is through lateral heat conduction along the in-plane direction to the current collecting land (like a heat sink). Heat removed by gas convection inside the gas channel accounts for less than 5% under typical PEFC operating conditions.

The energy equation in Table 1 contains location-specific heat generation terms, including irreversible heat of the electrochemical reaction, reversible en-
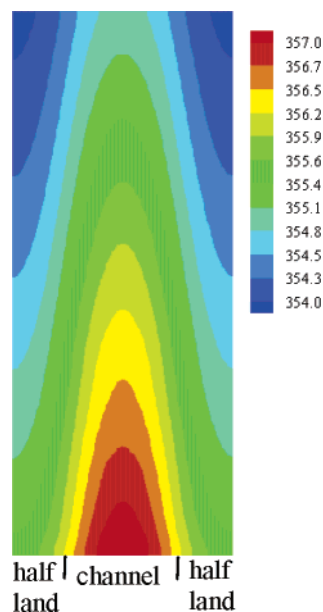
Figure 12. Temperature distribution (in K) in the middle of the membrane (EW < 1000) for a straight-channel PEM fuel cell (cell voltage = 0.6 V, average current density = 1.42A/cm²) with a cell temperature of 80 °C.

tropic heat, and Joule heating.[83] The reversible heat related to $T(\mathrm{d}U_o/\mathrm{d}T)$ was often overlooked in the majority of thermal modeling work in the literature. It represents the entropic heat produced by the cell even under thermodynamic equilibrium and is a significant contributor to overall heat generation.

Solving the energy equation provides prediction of the temperature distribution and its effect on cell performance in a PEFC. Figure 12 presents a temperature distribution in the middle of the membrane for a single-channel PEFC. The maximum temperature rise in this case is 4 °C, which will only affect cell performance slightly. However, the temperature variation depends strongly on the thermal conductivities of the GDL and flow plate as well as thermal boundary conditions.

Among the three heat-generation terms, the irreversible and reversible heat sources of ORR are dominant. For a straight-channel cell shown in Figure 12, the total amount of heat release is 2.57 W, of which the irreversible heat is 55.3%, the reversible heat 35.4%, and the Joule heat only 9.3%! The total heat released from the fuel cell can also be estimated from the overall energy balance, i.e.

$$Q_{\text{heat}} = (U_o - V_{\text{cell}})I_{\text{avg}}A + I_{\text{avg}}AT_{\text{avg}}\left(-\frac{\mathrm{d}U_o}{\mathrm{d}T}\right) = 2.56 \text{ (W)} \quad (19)$$

This is close to the simulated value of 2.57 W, including the irreversible, entropic, and Joule heat. The energy-conversion efficiency of this cell, defined as the ratio of the electric power ($I_{\text{avg}}V_{\text{cell}}A$) to the total energy consumption ($I_{\text{avg}}V_{\text{cell}}A + Q_{\text{heat}}$), is then calculated to be 40%. These simple calculations help demonstrate the validity and accuracy of a nonisothermal PEFC model.

Co-simulation of water and heat management in a 50 cm² cell can be seen from Figure 13. The
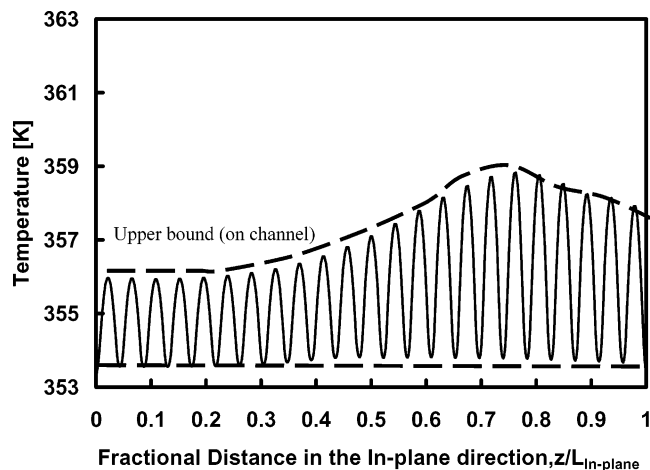
Figure 13. Temperature distribution in a low humidity 50 cm² fuel cell under the same operating conditions as in Figure 11.

membrane temperature fluctuates between channel and land areas. Furthermore, the membrane temperature is higher in the channel area due to lack of effective cooling, increases along the flow path due to higher current density, and then decreases near the outlet due to the current density lowered by oxygen depletion.

An important issue requiring future work is the consideration of anisotropic thermal transport since the thermal conductivity has an order of magnitude difference between the in-plane and through-phase directions as mentioned earlier.

3.4. Electron Transport

An important function of GDL is to provide electron lateral conduction, serving as a bridge between the catalyst layer and the current-collecting land. In nearly all the three-dimensional PEFC models published to date, electron transport in the catalyst layer/GDL as well as in the current collector plate is ignored by assuming a sufficiently large electric conductivity and, consequently, uniform electronic phase potential in these materials. The flow plate has an electric conductivity on the order of 2×10^4 S/m for graphite plates, but the effective electric conductivities of GDL and catalyst layers range only from 300 to 500 S/m (in the through-plane direction). These electronic resistances could significantly change the current distribution, both macroscopically along the flow direction and mesoscopically between the channel and land areas. Although the electron-transport equation was solved in the one-dimensional PEFC models of Bernardi and Verbrugge,[44,45] the lateral electronic resistance can only be assessed in a three-dimensional geometry. Furthermore, solving the electron-transport equation enables (1) direct incorporation of the contact resistance at interfaces between two mating components in the solution process, (2) direct implementation of the total current as a boundary condition instead of the cell voltage (permitting a true stoichiometry to be employed in PEFC modeling and thus consistency with typical fuel cell experiments), and (3) stack modeling with cells connected in series.

To calculate the electron-transport effect through GDL and flow plate, the charge conservation equation for the electronic phase must be solved additionally, namely

$$\nabla(\sigma^{\text{eff}}\nabla\Phi_s) - j = 0 \qquad (20)$$

where σ^{eff} is the conductivity of the electronic phase, Φ_s is the electronic phase potential, and j is the volumetric transfer current density inside the catalyst layer. When applied to the flow plate, eq 20 accounts for the ohmic loss occurring in plates with limited conductivity and small thickness (e.g., graphite plates used in fuel cell stacks).

Meng and Wang[14] performed a three-dimensional study of the effects of electron transport through the gas diffusion layer (GDL). Figure 14 displays the current density distributions in a single-channel fuel cell predicted by including lateral electron transport. As can be seen, without accounting for the lateral electron transport in GDL, the current density is highest in the middle of the channel because the reaction zone there has the easiest access to oxygen. However, once considering the electronic resistivity of GDL in the in-plane direction, the highest current density region is shifted toward the edges of the channel because these locations have the best combination of easy access to oxygen and short path for electron transport onto the current-collecting land. The effective electric conductivity of GDL used in this simulation was assumed to be isotropic and equal to 300 S/m, corresponding to carbon paper from SGL Group. This new finding clearly indicates the necessity to include the lateral electron transport in future CFCD models for high-fidelity computer simulations. Physically, this study revealed a new possibility to control the lateral current profile by tailoring the GDL electric property.

The effect of the flow plate electric conductivity on the axial current profile is shown in Figure 15.[97] It is seen that only with extremely conductive metal plates (i.e., $>2 \times 10^5$ S/m) does the constant current boundary condition also result in an equipotential line in the plate and hence the same current distribution. For graphite plates with an electric conductivity of $\sim 2 \times 10^4$ S/m, the potential drop in the plate between the inlet and outlet locations amounts to 27 mV under the constant current boundary condition, thereby causing a much flatter current density profile within the membrane than that observed when the plate is subject to constant voltage. The example shown in Figure 15 indicates the important impact of bipolar plate electric conductivity on current distribution, a new subject requiring attention in fuel cell engineering. Figure 15 also exemplifies a capability to simulate fuel cell performance under constant total current boundary condition instead of constant cell voltage. This approach is fundamentally different from the common practice in which the cell voltage is iterated until the resulting total current is matched with the prescribed value by running a number of cell simulations.

Meng and Wang[14] found that addition of numerical solution to eq 20 substantially increases computa-
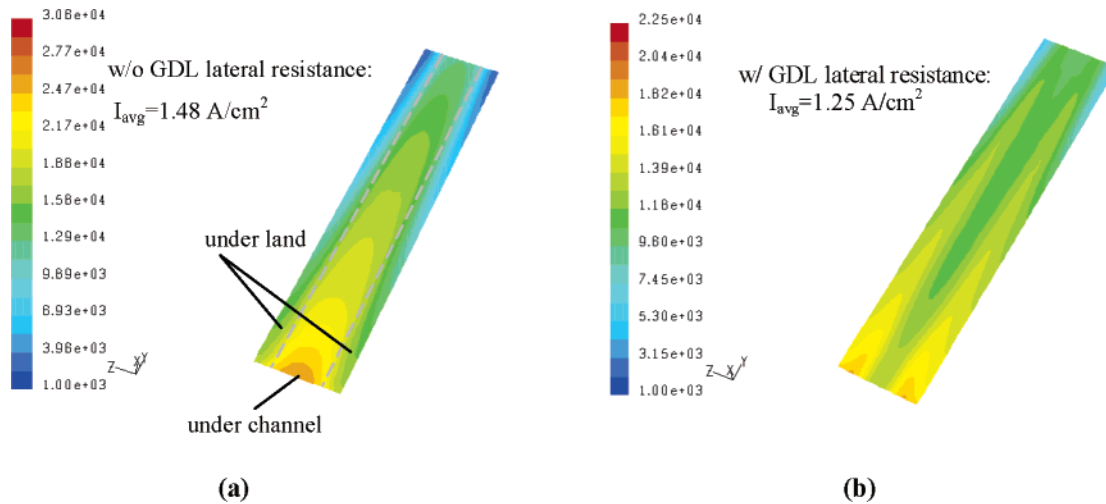
Figure 14. Current distribution in a straight-channel fuel cell at a cell voltage of 0.6 V: (a) without GDL electronic resistance and (b) with GDL electronic resistance.
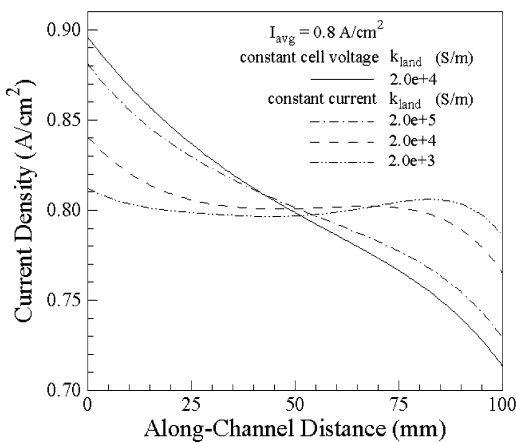
Figure 15. Current density profiles as a function of the flow plate electric conductivity (S/m) in a straight-channel fuel cell with an average current density of 0.8 A/cm^2.[97]

tional time. In the most recently released commercial CFCD code, CD-Adapco Japan apparently has developed a proprietary solution technique for eq 20 and the electrolyte potential equation together which does not incur any increase in computational time.[98] Moreover, their code, for the first time, accounts for anisotropic electric conductivity in the through-plane and in-plane directions. Future need certainly exists for more efficient numerical algorithms to solve eq 20 in a coupled fashion with the electrolyte potential equation, as described in section 2.2.2.

3.5. Transient Phenomena

Dynamic characteristics of a fuel cell engine are of paramount importance for automotive application. Three primary processes govern the time response of a PEFC. They are (1) electrochemical double-layer discharging, (2) gas transport through channel and GDL, and (3) membrane hydration or dehydration (i.e., between a dry and a hydrated state). The time constant of double-layer discharging is between micro- and milliseconds, sufficiently short to be safely ignored for automotive fuel cells. The time constant for a reactant gas to transport through GDL can be estimated simply by its diffusion time, i.e., δ^2_{GDL}/D_g.

This gives a time constant between 0.1 and 1 s. The slowest process, however, is membrane hydration, the time constant of which can be estimated by

$$\frac{\rho \delta_m \Delta \lambda}{EW} \Big/ \Big(\frac{I}{2F}\Big) \qquad (21)$$

This is to assume that a dry membrane is hydrated by production water generated at the current density, I. For Nafion 112 and a reference current density of 1 A/cm^2, this is about 25 s! Therefore, for low humidity cells where the membrane undergoes water content changes, the water accumulation term is essential for transient analyses.

Um et al.[55] were one of the first to study the transient response of a PEFC to a voltage step change. Due to the fully humidified gas feed on both the anode and cathode, the membrane hydration process no longer contributed to the cell transients; as such, it was sufficient to include gas-transport transients under these fully humidified conditions. For low humidity PEFC, Wang and Wang[66] further extended the work of Um et al.[55] to include the membrane hydration transient process. Figure 16 shows a time response of the average current density to a step change in cell voltage in a low humidity fuel cell. Overall, it can be seen that the current density does not simply follow a smooth variation from the steady state at 0.6 V to the steady state at 0.7 V. Instead, there exists significant undershoot and overshoot due, respectively, to the transient phenomena of gas transport and membrane hydration. In addition, with the inclusion of membrane hydration, the fuel cell transients occur over as long as 15 s, a magnitude needing careful attention for automotive application.

Specifically, Figure 16 shows that the current density in a cell with dry cathode gas feed drops nearly instantaneously once the cell voltage is relaxed from 0.6 to 0.7 V due to the fact that the electrochemical double-layer effect has a negligibly small time constant. Further, there exists undershoot in the current density as the oxygen concentration inside the cathode catalyst layer still remains low due to the larger consumption rate under 0.6 V. As the
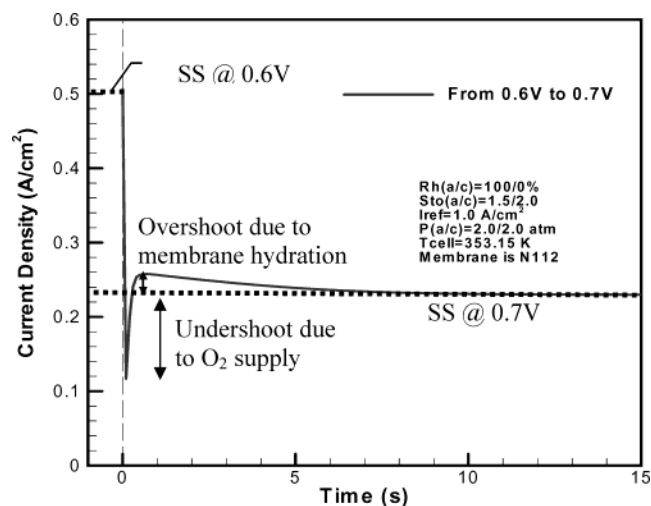
Figure 16. Transient response of current density to a step change of cell voltage from 0.6 to 0.7 V in a fuel cell with a fully humidified anode and dry cathode.[66]

O_2 consumption rate becomes smaller under 0.7 V, the O_2 concentration at the reaction surface recovers, thus leading to an increase in the cell current density. The current rise time corresponds well with the characteristic time scale of gas phase transport as analyzed above. The rise in the cell current, however, experiences an overshoot because the polymer membrane still maintains a higher water content corresponding to 0.6 V. It then takes about 15 s for the membrane to adjust its water content at the steady state corresponding to 0.7 V. This numerical example clearly illustrates the profound impact of water management on transient dynamics of low humidity PEFC engines where the polymer membrane relies on reaction water for hydration or dehydration.

3.6. Large-Scale Simulation

Large-scale simulation of a PEFC is needed in order to consider all three dimensions. The importance of parameter variations in the through-plane direction was first recognized in the earliest 1-D models. Subsequent 2-D models addressed the important facet of changes in reactant and water concentrations along the flow direction, especially when the modern designs of low humidity and low stoichiometry emerged. The third dimension, i.e., the in-plane direction from a channel to a land, has been recognized for its importance of the lateral transport of species and electrons. Here, we are primarily concerned with a mesoscopic scale of approximately 1 mm. On this mesoscale, nonuniform current distribution may result primarily from the low diffusion rate of oxygen in the restricted area covered by the land and GDL resistance to lateral electron motion.

Such a large-scale simulation resolving all three dimensions for industrial-scale fuel cells featuring tens of flow channels is now being made possible by parallel computing on PC clusters using millions of computational cells.[65] Figure 17 shows the current distribution in a 36-channel fuel cell predicted using 2 560 000 grid points. This 50 cm² fuel cell features a double-pass serpentine flow field on the cathode. To be able to operate under dry air feed, the two
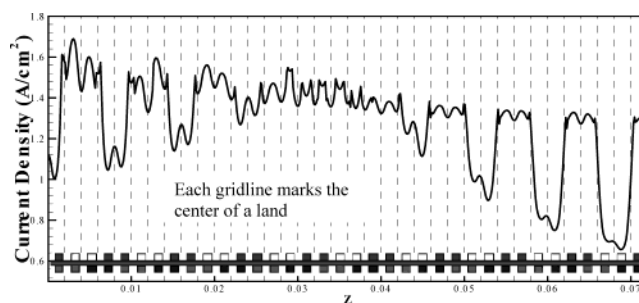
Figure 17. Current density profile in the midchannel cross-section of a 36-channel fuel cell.[65]

passes are made countercurrent with one air inlet on the left and the other air inlet on the right, following a patented idea of Qi and Kaufman.[99] Such a counterflow serpentine flow field is intended to promote lateral moisture transport between a dry gas channel (near the inlet pass) and its neighboring moist gas channel (near the exit pass) and hence cell internal humidification. Both large-scale variations and channel-to-land local oscillations are visible from the current distribution shown in Figure 17, where the anode feed is fully humidified. Figure 18 displays a profile of the net water-transport coefficient through the membrane in the same cross-section of the cell. This parameter, α, is a combined result of the electro-osmotic drag and molecular diffusion of water through the membrane and is defined as the ratio of the net water flux to the protonic flux; thus, the unit is the number of H_2O/H^+. As shown in Figure 18, α varies between -0.5 and 1.5 and changes rapidly between closely spaced channels, especially between a dry gas channel and a moist gas channel. The parameter critical to the choice of a suitable water management strategy reflects a complex interplay between the electro-osmotic drag and water diffusion through the membrane. α being positive means the dominance of electro-osmotic drag. Since the drag coefficient is constant at unity in the range of water content in question, α-values greater than unity indicate the electro-osmotic drag aided by the forward diffusion of water from the anode (fully humidified) to the relatively dry cathode. Negative α-values are indicative of the dominance of back diffusion of water from the cathode (high water concentration created byproduct water) to anode. Figures 17 and 18 clearly illustrate the need for large meshes in order to resolve sharp gradients in the channel-to-land direction in addition to the through-plane and flow directions.

Other work involving large-scale simulation of PEFCs was due to Meng and Wang[15] and Ju and Wang.[6,100]

3.7. Liquid Water Transport

High current density performance of PEFCs is known to be limited by transport of reactants and products. In addition, at high current densities, excess water is generated and condenses, filling the pores of electrodes with liquid water and hence limiting the reactant transport to catalyst sites. This phenomenon known as "flooding" is an important limiting factor of PEFC performance. A fundamental
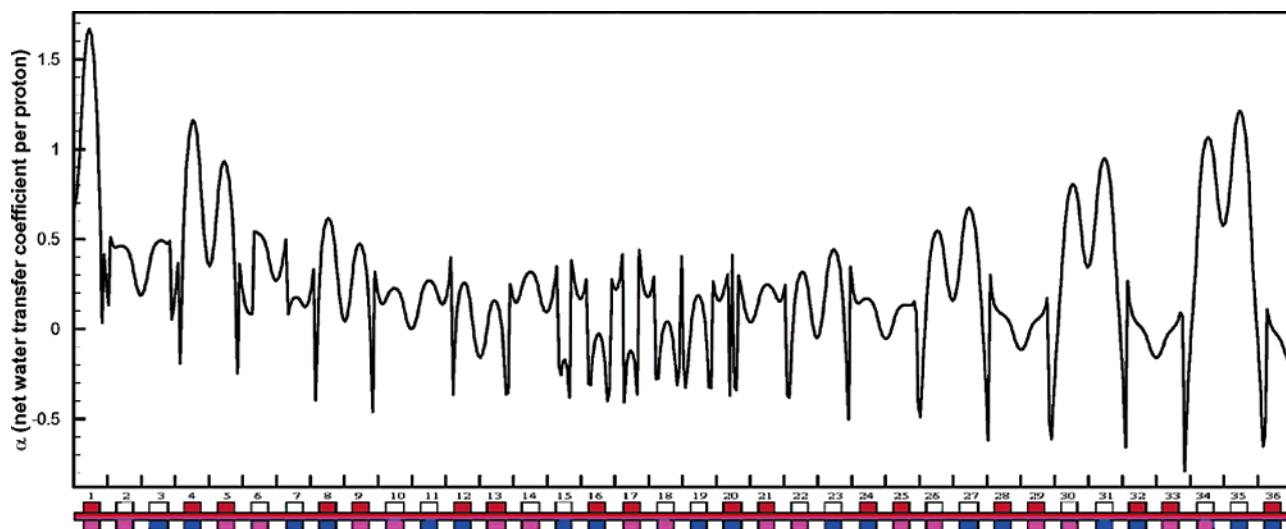
Figure 18. Profile of the net water transport coefficient through the membrane in the midchannel cross-section of a 36-channel fuel cell at $V_{cell} = 0.65$V and $I_{avg} = 0.91$ A/cm^2.[65]

understanding of two-phase transport in porous gas diffusion layers (GDL) of PEFC is essential in order to improve performance. Flooding of electrodes is generally linked to high current density operation that results in higher water production rate; yet, flooding can also be seen even at low current densities under certain operating conditions, such as low temperatures and low gas flow rates, due to faster saturation of the gas phase by water vapor. For instance, in automotive fuel cells, cell start-up is performed under ambient conditions in which the temperature is lower than the desired operating temperature, commonly referred as "cold start". At cold-start temperatures, the saturation vapor pressure of water is extremely low; therefore, saturation of the gas phase with water vapor, hence flooding, may occur even in relatively low current densities, greatly affecting the start-up characteristics and transient dynamics of PEFC operation.

While there exist several studies investigating the two-phase transport in a PEFC,[46,47,69–72,101,102] none considered the effect of GDL hydrophobicity. Some modeling studies were published in order to predict PEFC performance at given flooding levels without attempting to analyze the transport of liquid water.[46,47,101,102] He et al.[69] proposed a two-dimensional two-phase model for PEFC with interdigitated flow field in which they included capillary transport of liquid water in a completely hydrophilic GDL. Wang et al.[68] developed a two-phase model of the air cathode of PEFC also with a hydrophilic GDL based on the M² formulation (multiphase mixture model) of Wang et al.[79] Subsequently, You et al.[72] published a similar work investigating the effects of several operating parameters on two-phase transport. Most recently, Mazumder and Cole[73] presented a numerical study also based on the M² model of Wang and Cheng.[79] Mazumder and Cole's model appears to be valid only in the two-phase regime where there is liquid water. Under low humidity inlet conditions where the liquid saturation is zero, this model yielded zero electro-osmotic drag through the polymer membrane. Berning and Djilali[74] presented a two-phase model for porous GDL and gas channel of a PEFC

while excluding the MEA. Water transport through MEA is thus completely ignored. Berning and Djilali also failed to address the effect of GDL hydrophobicity. None of these above-mentioned studies are intended to investigate and analyze two-phase transport in hydrophobic GDL. A brief review of this subject was given by Wang.[5]

The central question about the physics of liquid water transport through hydrophobic GDL has remained unexplored until recently. Nam and Kaviany[103] described a one-dimensional model for liquid water transport through hydrophobic GDL. In this model, the gas-phase pressure is assumed to be uniform, thereby rendering the liquid-phase transport governed by the gradient in capillary pressure. The model was used to assess the effects of GDL fiber diameter, porosity, and capillary pressure on the liquid water distribution. Independently, based on extensive experimental observations of liquid water flow in an operating PEFC, Pasaogullari and Wang[104] most recently proposed a systematic theory of liquid water transport through hydrophobic GDL. Condensation results in a tree-like liquid water percolation network in the porous GDL. Liquid water then reaches the interface of the porous GDL with the gas channel, forming liquid droplets. Inside GDL, liquid water is driven by capillary (wicking) action. In hydrophobic GDL, the capillary pressure is negative; hence, the liquid pressure is larger than the gas-phase pressure, whereas in hydrophilic media, the gas-phase pressure is higher than of the liquid phase.

In addition, the liquid pressure increases with liquid saturation; therefore, a liquid pressure gradient is formed from higher to lower liquid saturation regions. This pressure gradient becomes the driving force for liquid water flow, as schematically shown in Figure 19. In PEFC, the liquid saturation is higher at the catalyst layer, due to water generation and electro-osmotic drag, than the GDL–channel interface. Therefore, the liquid pressure gradient formed in the GDL drives liquid water from the reaction sites toward the gas channel. Figure 19 also displays a nearly constant gas pressure profile across the two-phase zone due to much lower gas-phase viscosity.
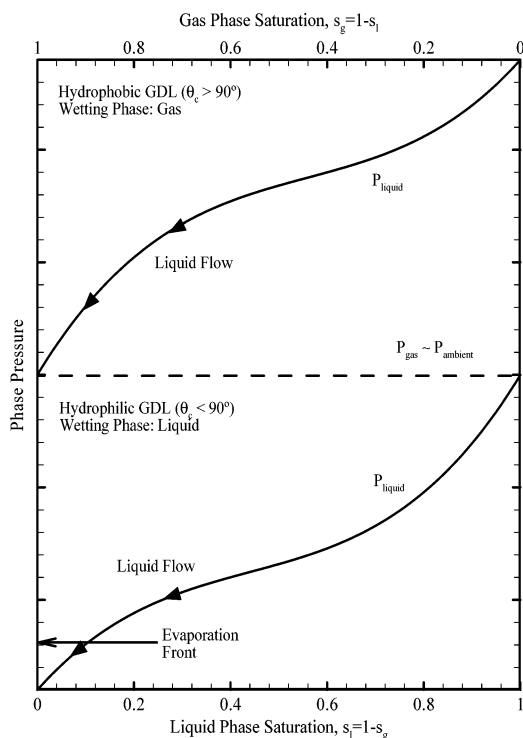
Figure 19. Schematic illustration of liquid- and gas-phase pressure profiles in hydrophilic and hydrophobic porous media.[104]

That is, it does not incur much gas pressure drop to drive the gas flow through thin GDL.

It is interesting to note from Figure 19 that although the relative magnitude of the liquid to gas pressure is different in hydrophobic GDL than in hydrophilic GDL, both media provide capillary action to drive liquid water from the inside to the surface. However, the slope of the capillary pressure (i.e., the driving force) is different depending on whether water is the wetting or nonwetting phase. The greater slope of the capillary pressure near the evaporation front (i.e., $s \approx 0$) in hydrophobic GDL is indicative of increased effectiveness of this type of medium for water removal. Furthermore, the liquid pressure buildup in the hydrophobic cathode likely sets up a hydraulic pressure differential to drive water flow back through the membrane into the anode.

The shape of liquid droplets emerging at the GDL/channel interface is governed by the wetting char-

acteristics of the GDL surface. On a hydrophilic surface, which has a contact angle less than 90°, liquid will spread, whereas on a hydrophobic surface, which has a contact angle greater than 90°, the droplet will be of a more spherical shape, covering less pore entry, as depicted in Figure 20.[105]

Both theories of liquid water transport through hydrophobic GDL proposed by Nam and Kaviany[103] and Pasaogullari and Wang[104] require a boundary value of liquid saturation at the GDL/channel interface. This interfacial saturation should not be equal to the immobile saturation (and hence no liquid flow) but depends on the break-off (or detachment) diameter of liquid droplets and population density, both of which are, in turn, strong functions of the GDL surface contact angle and the gas velocity in the flow channel. Nothing has been formally published on this problem, although it is under intensive investigation in industry.

To summarize, to properly model liquid water transport and ensuing flooding effect on cell performance, one must consider four submodels: (1) a model of catalytic surface coverage by liquid water inside the catalyst layer, (2) a model of liquid water transport through hydrophobic microporous layer and GDL, (3) an interfacial droplet model at the GDL surface, and last (4) a two-phase flow model in the gas channel. Both experimental and theoretical works, in academia and industry alike, are ongoing to build models for the four key steps of water generation, transport, and removal from a PEFC.

Pasaogullari and Wang[67] further developed a 3-D, isothermal, full-cell numerical model for PEFC by integrating the above-described theory of liquid water transport in hydrophobic GDL with other submodels described in sections 3.1–3.3. Figure 21 compares the current density profiles along the flow direction from a two-channel serpentine fuel cell with the anode and cathode in co-flow, as predicted by the single- and two-phase models. The effect of flooding is clearly visible, although the difference in the average current density amounts to only 6% between the two model predictions. It is seen that the current density near the channel inlet is much higher in the single-phase model than the two-phase model, where it suffers from severe flooding of the cathode. Liquid water limits oxygen transport and covers a portion of the active catalyst particles, resulting in lower perfor-
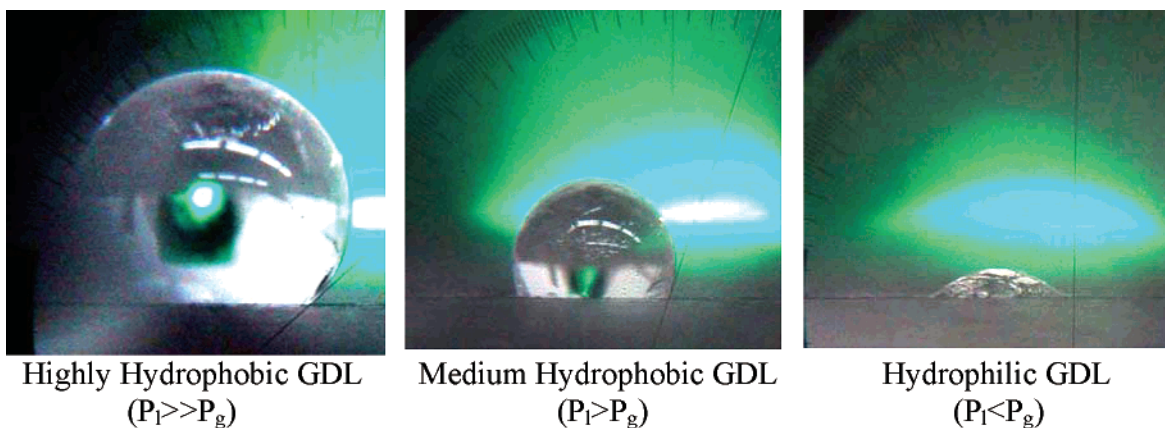

Figure 20. Liquid water droplets on GDL of different wettability at 70 °C.[105]
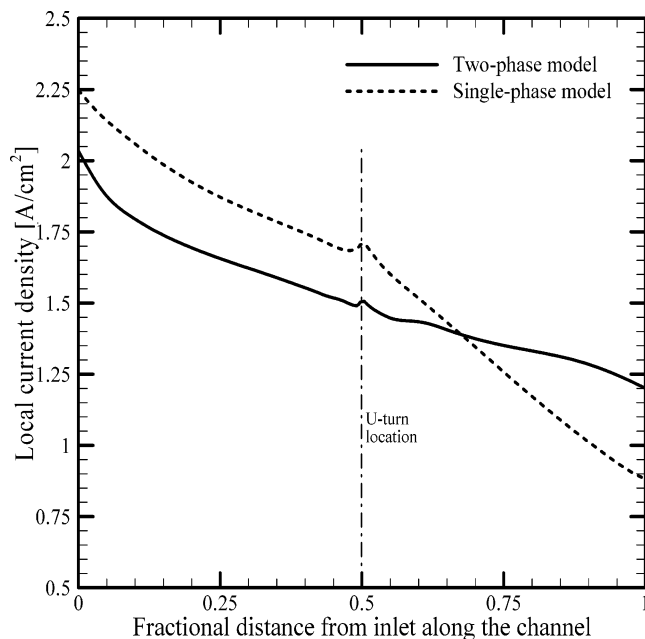
Figure 21. Comparison of local current density distributions in a two-channel serpentine PEFC at V_{cell} = 0.4 V.[67]

Figure 22. Local current density profiles along the channel direction for different humidification levels at V_{cell} = 0.65 V. Anode and cathode stoichiometries are 1.4 at 1.0 A/cm^2.[67]

mance near the inlet. In addition, the current distribution predicted from the two-phase model is more uniform because flooding upstream tends to limit cell performance there as well as oxygen consumption. This leaves a higher oxygen concentration downstream to enhance the current density. Another interesting feature of the current density profiles shown in Figure 21 is seen around the U-turn location, especially with the single-phase model prediction. Due to the mixing effect and secondary flows around the U-turn of serpentine flow channels, the convective transport of oxygen to the catalyst layer is enhanced; hence, a localized spot of higher performance appears in the single-phase results. The same phenomenon is also seen in the two-phase results but at a smaller magnitude, because liquid water in GDL hampers the gas flow and reduces the level of oxygen-transport enhancement under very small gas velocities. In industrial-scale fuel cells, the gas-feed velocities through channels would be much higher, and this phenomenon may also be expected at a larger magnitude even in flooded GDL.

Operating parameters such as humidification and flow rates of inlet reactant streams have a substantial influence on PEFC performance and transport characteristics. A two-dimensional numerical study was performed to investigate these effects.[67] In Figure 22 the local current density distributions at 0.65 V for different humidification levels are given. It is seen that in the fully humidified case, the local current density monotonically decreases along the flow direction as a result of mass transfer limitations due to both oxygen depletion and flooding. In the case of 70% anode and 20% cathode inlet relative humidity, the membrane stays relatively dry throughout the cell and shows a membrane ionic resistance limited behavior. The current density increases along the flow direction, since the membrane water content is increasing due to ORR. In this case, oxygen depletion is not severe because the current density
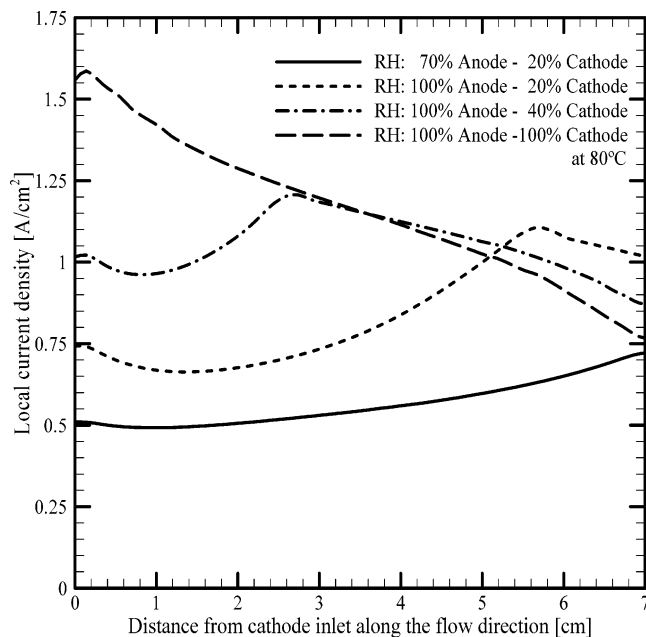
overall is small. However, for the lower cathode humidity cases with fully humidified anode inlet (i.e., 20% cathode/100% anode and 40% cathode/100% anode cases), there exist three distinct regimes of the current distribution: (i) the ionic resistance limitation due to membrane dry out in the first part, (ii) a middle section with highest performance where the membrane is fully humidified, and (iii) mass transfer limitations due to flooding and/or oxygen depletion in the last part of the cell. It is seen that even with low cathode inlet humidification levels, i.e., 20% and 40%, the water concentration in porous GDL exceeds the saturation value and flooding takes place in the regions near the channel exit. In these cases the cell suffers from membrane dry out near the inlet, especially on the anode side, due to the electro-osmotic drag of water to the cathode. Near the inlet, the cathode water concentration is lower; therefore, back-diffusion of water from the cathode to anode does not compensate for the electro-osmotic drag, resulting in the anode dry out.

As shown in Figure 23, the fully humidified case shows a maximum liquid saturation around 10% near the inlet and decreases in the flow direction due to decreasing reaction rate in the cathode catalyst layer. The 10% level of liquid saturation results from using a realistic GDL permeability on the order of 10^{-12} m^2.[67] Higher liquid saturation values reported in the literature were obtained only by using unrealistically small permeability, i.e., 95% maximum liquid saturation with GDL permeability of 7.3 $\times \cdot 10^{-15}$ m^2.[70]

In the low humidity cases, the cell does not produce liquid water immediately but after the water vapor concentration in the gas reaches the saturation value; therefore, the condensation front is pushed downstream, and its location is directly related to cathode inlet relative humidity. In the 20% cathode relative humidity case, it is found that the first two-thirds of
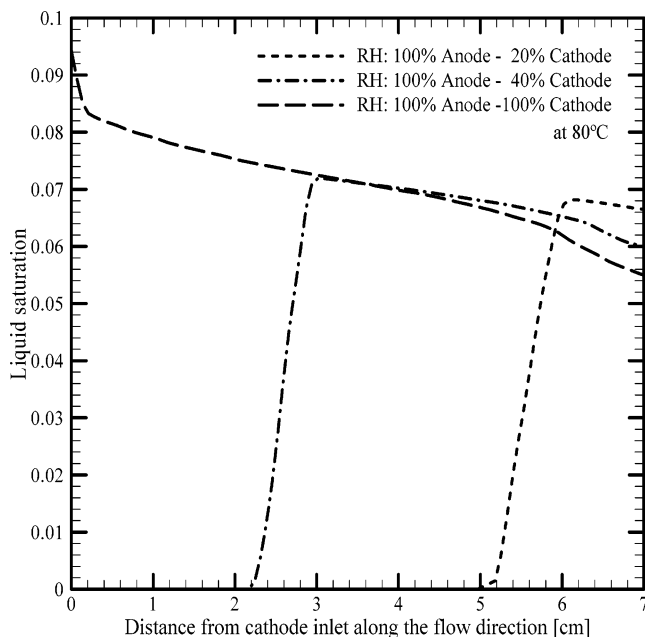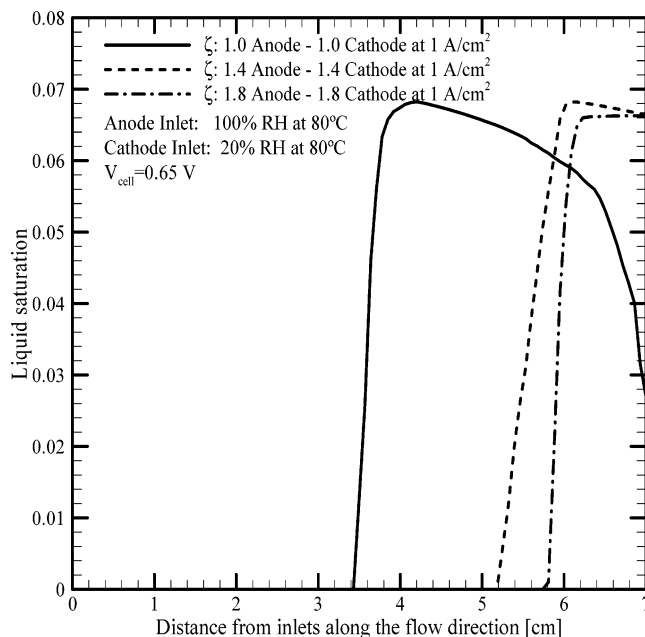
Figure 23. Liquid saturation profiles at cathode GDL–catalyst layer interface along the channel direction for different humidification levels at $V_{cell} = 0.65$ V. Anode and cathode stoichiometries are 1.4 at 1.0 A/cm². [67]
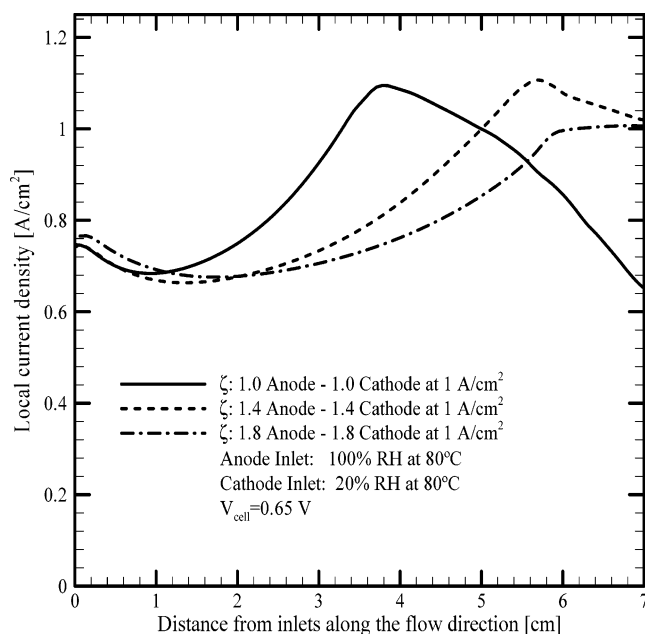
Figure 24. Local current density profiles along the channel direction of single-channel PEFC for different inlet stoichiometric ratios at $V_{cell} = 0.65$V at the inlet relative humidity: 20% cathode and 100% anode at 80 °C. [67]

the cell is free from liquid water, whereas it is predicted that liquid water starts to appear around one-third of the channel length in the 40% cathode relative humidity case.

The effect of inlet stoichiometry on transport characteristics and performance of PEFC was also investigated by Pasaogullari and Wang. [67] In Figure 24 the local current density distributions along the flow direction are displayed at a cell voltage of 0.65 V. As explained earlier, the membrane is hydrated much faster in lower flow rates, and therefore, the performance peak is seen earlier in lower stoichio-

Figure 25. Liquid saturation profiles at cathode GDL–catalyst layer interface along the channel direction of single-channel PEFC for different inlet stoichiometric ratios at $V_{cell} = 0.65$ V and inlet relative humidity: 20% cathode and 100% anode at 80 °C. [67]

metric ratios. However, as the GDL gets saturated with water vapor, water starts to condense and the cell starts to suffer from flooding of GDL as well as oxygen depletion, which result in performance decline. The liquid saturation profiles given in Figure 25 show that with decreasing gas flow rate, the condensation front moves closer to the channel inlet.

Latent heat associated with phase change in two-phase transport has a large impact on the temperature distribution and hence must be included in a nonisothermal model in the two-phase regime. The temperature nonuniformity will in turn affect the saturation pressure, condensation/evaporation rate, and hence the liquid water distribution. Under the local interfacial equilibrium between the two phases, which is an excellent approximation in a PEFC, the mass rate of phase change, $\dot{m}_{fg}$, is readily calculated from the liquid continuity equation, namely

$$\dot{m}_{fg} = \epsilon \frac{\partial(\rho_l s)}{\partial t} + \nabla(\rho_l \vec{u}_l) \qquad (22)$$

Since the liquid-phase velocity is obtained, for example, from the M² model as follows

$$\rho_l \vec{u}_l = \vec{j}_l + \lambda_l \rho \vec{u} \qquad (23)$$

Substituting eq 23 into eq 22 yields

$$\dot{m}_{fg} = \epsilon \frac{\partial(\rho_l s)}{\partial t} + \nabla(\vec{j}_l + \lambda_l \rho \vec{u}) \qquad (24)$$

The heat release or adsorption due to condensation or evaporation is simply given by

$$S_T = h_{fg} \dot{m}_{fg} \qquad (25)$$

where h_{fg} is the latent heat of vapor–liquid phase change.

Last, all models describing liquid water transport through GDL can be categorized into two approaches: the M² model and unsaturated flow theory (UFT). UFT assumes a constant gas phase pressure, thus effectively decoupling the liquid water transport from gas flow. The models of Nguyen and co-workers,[69,70] Berning and Djilali,[74] Nam and Kavinay,[103] and Pasaogullari and Wang[104] belong to UFT. In contrast, the M² model is a more complete two-phase model in which motions of both liquid and gas phases are accounted for. The work of Wang et al.,[68] You and Liu,[72] Mazumder and Cole,[73] and Pasaogullari and Wang[67] are based on the M² model. Most recently, Pasaogullari and Wang[75] fully elaborated the differences between the M² and UFT models for PEFC GDLs and revealed an interesting new mechanism for oxygen transport that results from the gas counterflow to the liquid water motion. In addition, the roles of a microporous layer played in two-phase transport in a PEFC were elucidated.[75]

3.8. Experimental Diagnostics and Model Validation

Experimental diagnostics not only help develop a fundamental understanding of fuel cell dynamics but also provide benchmark-quality data for CFCD model validation. Motivated by both needs, diagnostic efforts are presently directed toward local distribution measurements (vs global), multiple and simultaneous measurements, in-situ and nonintrusive measurements, as well as simple and well-defined cell configurations rather than experimentation involving various complex configurations of direct interest to the industry. This section reviews work published in the literature on current distribution, high-frequency resistance distribution, mass distribution, temperature distribution, and two-phase visualization for elucidation of the flooding process.

3.8.1. Current, Species, and High-Frequency Resistance Distribution Measurements

Quantification of current, specie, and membrane resistance distributions in a PEFC is critical to understanding key phenomena, such as water management, CO poisoning, and flow-field design effect, and providing valuable data for validation of CFCD models. As indicated by Wang,[4,5] it is this type of detailed validation that will permit an ultimate understanding of the physicochemical phenomena in PEFC as well as development of computer-aided tools for design and development.

To measure the current distribution in a hydrogen PEFC, Brown et al.[106] and Cleghorn et al.[107] employed the printed circuit board approach using a segmented current collector, anode catalyst, and anode GDL. This approach was further refined by Bender et al.[108] to improve ease of use and quality of information measured. Weiser et al.[109] developed a technique utilizing a magnetic loop array embedded in the current collector plate and showed that cell compression can drastically affect the local current density. Stumper et al.[110] demonstrated three methods for the determination of current density distribution of a hydrogen PEFC. First, the partial membrane electrode assembly (MEA) technique involves either masking different areas or partially catalyzing segments of the MEA to determine local current density behavior. Second, the subcell technique involves electrically isolating individual locations of catalyzed anode and opposing cathode from the main cell in order to measure the performance of the desired location. In the passive current mapping technique, an array of shunt resistors normal to an unmodified MEA surface are located between the flow field and a buss plate. Voltage sensors passively determine the potential drop across each resistor, and via Ohm's law, current distribution through the flow plate is determined. While each of the described methods for determination of current distribution has advantages, it is desirable to utilize a nonsegmented MEA in order to preserve true fuel cell operation characteristics and avoid highly individualized specialty membranes. Note also that all predictive models are developed for nonsegmented MEA.

In addition to the use of conventional MEAs and good spatial resolution, the ability to determine transient effects from sudden changes in operating conditions is desired. The nonsegmented passive current mapping technique of Stumper et al.[110] allows transient measurement and has good spatial resolution but requires an array of embedded and highly precise shunt resistors. The magnetic loop method of Weiser et al.[109] also allows transient measurements with unaltered MEAs and flow fields but is more difficult to implement than the other methods and cannot be applied to stacks. Recently, Mench and Wang demonstrated an improved technique for accurate current distribution measurements first on a DMFC[111] and later on a H₂/air PEFC.[112] Independently, Noponen et al.[113,114] developed and demonstrated a similar technique.

A common problem prevailing in much of the published work on use of the segmented cell is inability to produce a similar level of current density expected from a nonsegmented single cell. Lower performance originates from the difficulty that a segmented cell, if not well designed, fabricated, and assembled, exhibits much higher electric contact resistance between the segmented flow-field plate and GDL. As a result, the measured current distribution is more reflective of the contact resistance distribution than the intrinsic distribution of water and reactants inside the cell. Such an artifact due to intrusiveness of the measurement must be minimized in order for the segmented cell technique to produce truly useful data of current distribution. A future goal for this field is to produce current distribution data representative of automotive operating conditions, such as a temperature level of 80 °C, average current density level of 1 A/cm², and voltage level of 0.6 V. Only then will the segmented cell technique have the potential to become a standard diagnostic tool for fuel cell research and development.

Localized AC impedance and current distributions were measured by Brett et al.[115] on a single linear channel with the segmented cathode current collector plate. Figure 26 shows their measured current density and membrane resistance distributions along the
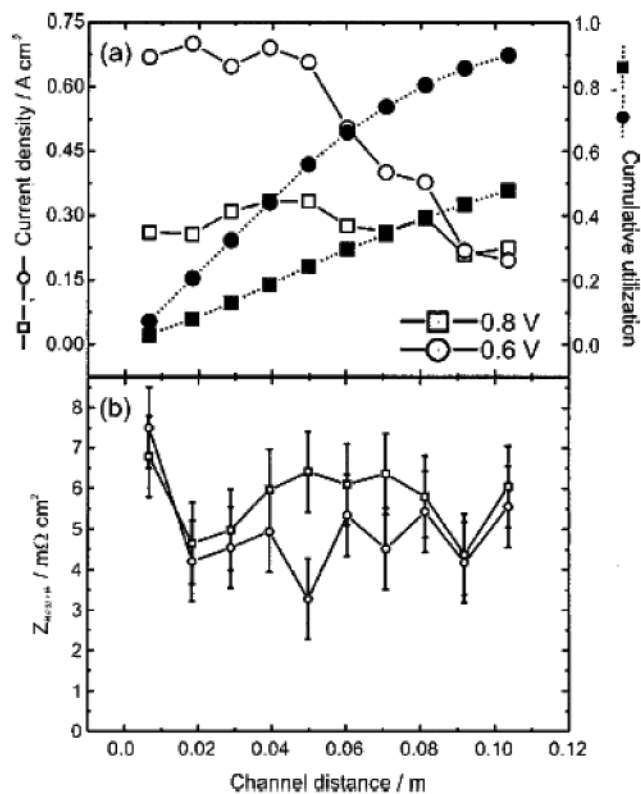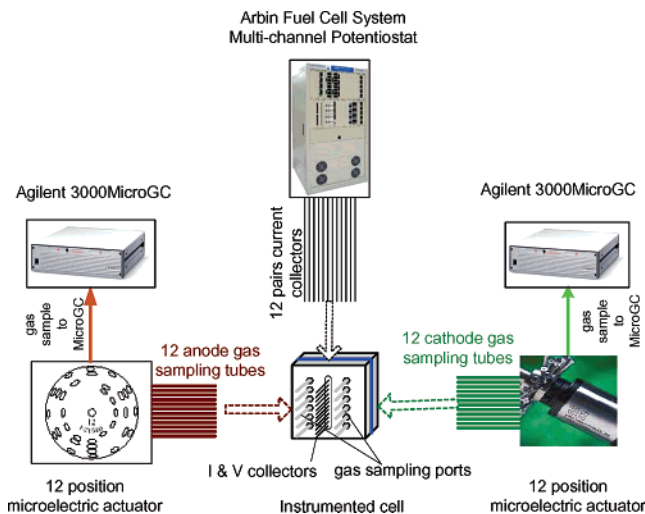
Figure 26. Current (a) and high-frequency resistance (b) distributions at cell potentials of 0.8 and 0.6 V as measured by Brett et al.[115]
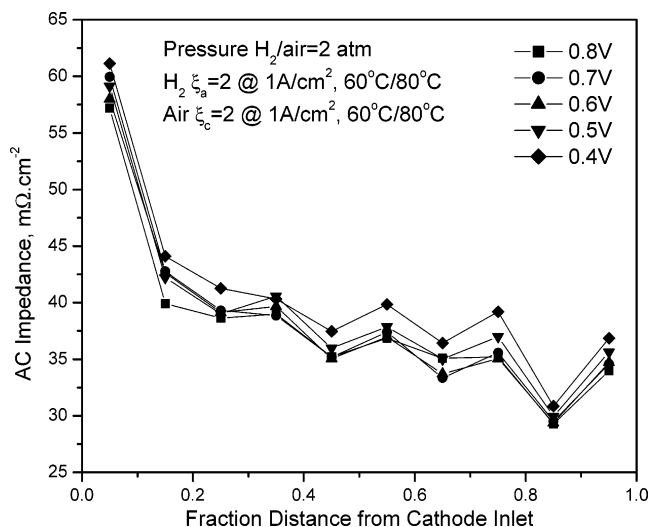
Figure 27. Distribution of high-frequency resistances measured at 1.5 kHz in a low humidity PEFC using 30 μm membrane (EW < 1000).

channel for two cell potentials. Carbon paper along with Nafion 112 was used to construct a MEA in this experimental cell. Interestingly, there is no significant variation between the membrane resistance along the channel length or between the two set potentials, despite a dry cathode feed and the fully humidified anode feed. Figure 27 displays another example of high-frequency resistance (HFR) distributions measured in a low humidity cell with Gore PRIMEA membrane (30 μm, EW < 1000) and carbon cloth as GDL. These measurements also show little variation for different cell potentials. However, the


Figure 28. Schematic diagram of the experimental setup for simultaneous measurements of anode/cathode species, current, and high-frequency resistance (HFR) distributions in an operating cell.[120]

higher HFR is clearly seen near the inlet where the membrane is dehydrated by dry inlet gases.

Distributions of water and reactants are of high interest for PEFCs as the membrane conductivity is strongly dependent on water content. The information of water distribution is instrumental for designing innovative water management schemes in a PEFC. A few authors have studied overall water balance by collection of the fuel cell effluent and condensation of the gas-phase water vapor.[116−118] However, determination of the in situ distribution of water vapor is desirable at various locations within the anode and cathode gas channel flow paths. Mench et al.[119] pioneered the use of a gas chromatograph for water distribution measurements. The technique can be used to directly map water distribution in the anode and cathode of an operating fuel cell with a time resolution of approximately 2 min and a spatial resolution limited only by the proximity of sample extraction ports located in gas channels.

More advanced capability exists in an apparatus to simultaneously measure species, current, and high-frequency impedance distributions using segmented fuel cells.[120] A schematic diagram of the experimental apparatus is shown in Figure 28. Two sets of 12-port electric microactuators and gas chromatographs are used to measure gas concentration distributions on the anode and cathode sides simultaneously. The arrays of multiple scalar distributions obtainable from this apparatus have been the basis for much improvement in CFCD modeling in our research program at Penn State. Figure 29 shows the typical current density distributions along the cathode flow path in a PEFC with fully humidified anode and cathode. It is seen that the level of average current density matches well with a realistic fuel cell under similar operating conditions. Moreover, the decline in the local current density along the flow path due to oxygen depletion is evident. This decline is more severe under lower cell voltage or higher average current density. To illustrate the species distribution measurement capability by microGC, Figures 30 and 31 display water mole fraction
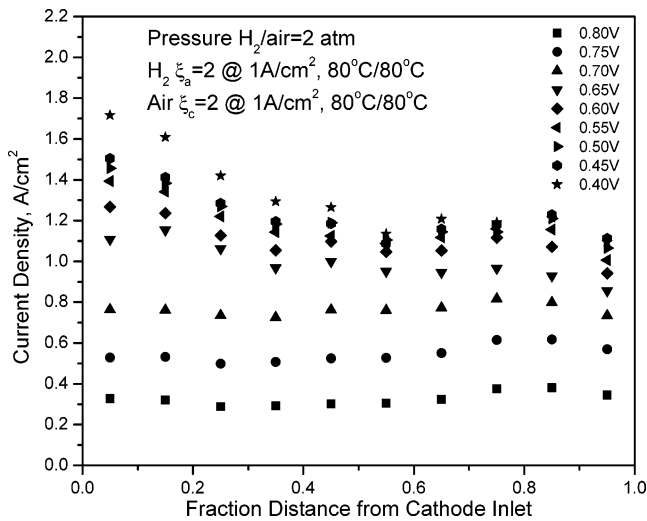
Figure 29. Current density distributions in a fully humidified PEFC using 30 μm membrane (EW < 1000) under various cell voltages.
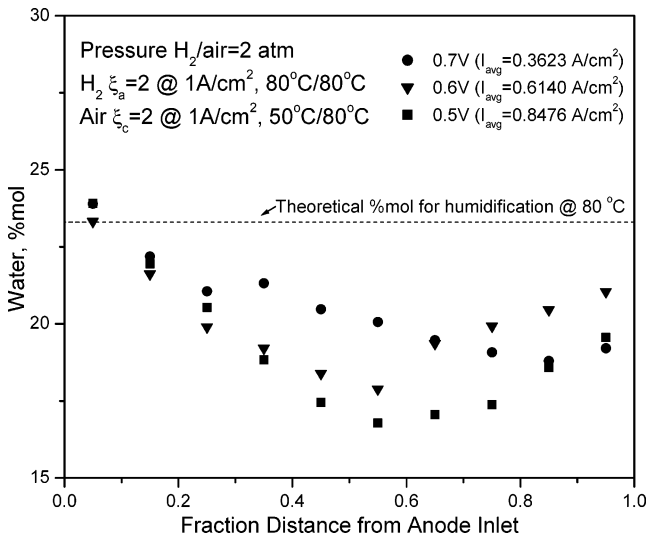
Figure 30. Water mole fraction profiles along the anode gas channel measured by a microGC in a cathode under-humidified PEFC using 30 μm membrane (EW < 1000).

distributions inside the anode and cathode gas channels, respectively, under the conditions that the anode inlet is fully humidified and the cathode humidification temperature is 50 °C relative to the cell temperature of 80 °C. It is seen from Figure 30 that the anode water mole fraction shows a decrease-then-increase trend. Beginning from the inlet, the anode gas loses water owing to both electro-osmotic drag and forward diffusion driven by the higher water concentration on the anode side. After a minimum point of water mole fraction at a certain location downstream of the anode channel, the water mole fraction begins to increase again once the water concentration on the cathode side increases and enhances back diffusion from the cathode to anode. It is interesting to note that the location of minimum water mole fraction shifts more downstream when the cell voltage is higher or the amount of water production is lower on the cathode side.

For a relatively dry cathode inlet (i.e., the humidification temperature of 50 °C versus the cell temperature of 80 °C), Figure 31 displays how the water
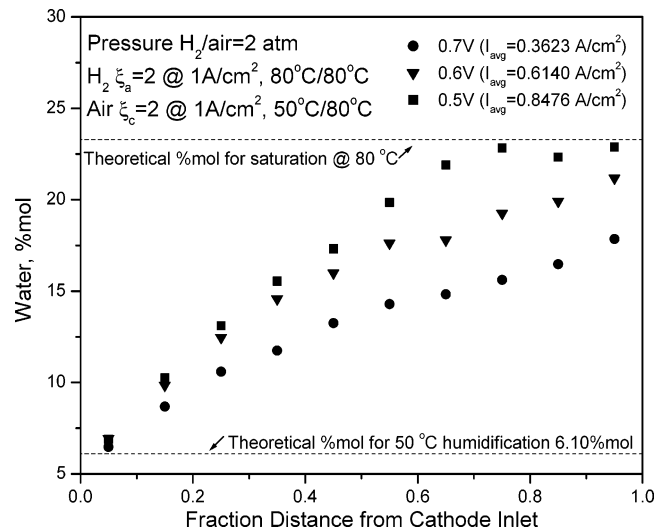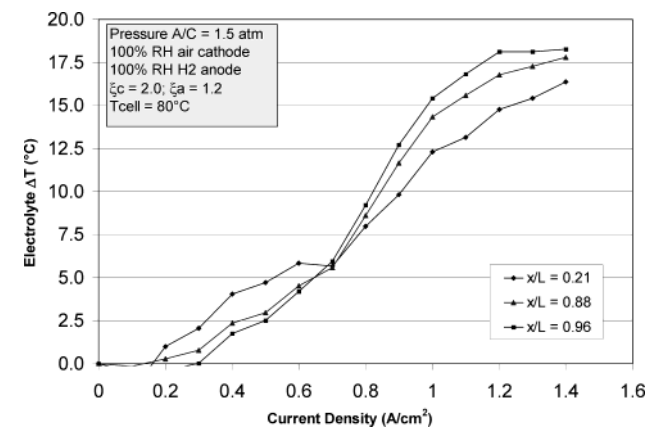

Figure 31. Water mole fraction profiles along the cathode gas channel measured by a microGC in a cathode under-humidified PEFC using 30 μm membrane (EW < 1000).

Figure 32. Rise of electrolyte temperature from the initial temperature at open circuit as a function of current density.[121]

mole fraction increases along the flow path of the cathode gas channel. This increase is nearly linear until approaching the saturation limit. The information from Figures 30 and 31 on water distributions in both the anode and cathode sides yielded the profile of the net water-transport rate through the membrane along the flow direction for the first time.

3.8.2. Temperature Distribution Measurements

Mench et al.[121] developed a technique to embed microthermocouples in a multilayered membrane of an operating PEM fuel cell so that the membrane temperature can be measured in situ. These microthermocouples can be embedded inside two thin layers of the membrane without causing delamination or leakage. An array of up to 10 thermocouples can be instrumented into a single membrane for temperature distribution measurements. Figure 32 shows the deviation of the membrane temperature in an operating fuel cell from its open-circuit state as a function of the current density. This new data in conjunction with a parallel modeling effort of Ju et al.[64] helped to probe the thermal environment of PEM fuel cells.

(a) Polarization behaviors

| Droplet emergence from hydrophobic GDL | Another droplet emerging on the left and more growth of existing droplet | More growth of both droplets | Coalescence, lifted up to the hydrophilic sidewall, and removed in liquid film |
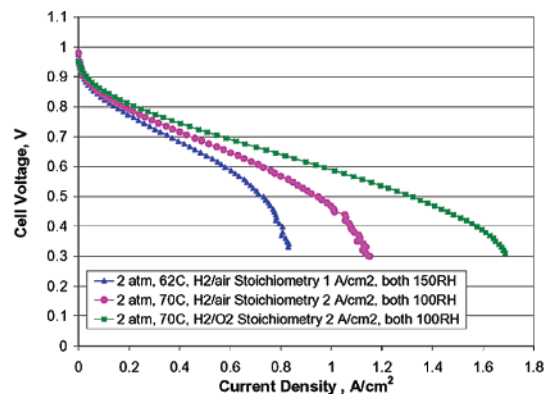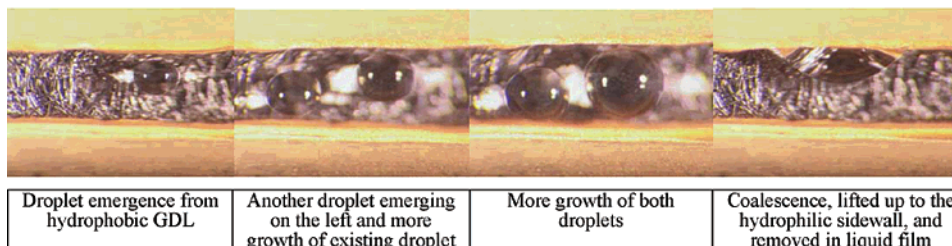
(b) Snapshots showing water droplet dynamics from GDL surface

Figure 33. Visualization of liquid water transport in an operating transparent PEFC (45 μm membrane with EW < 1000; GDL, Toray paper TGPH 090 with 20 wt % PTFE loading with a microporous layer).[125]

3.8.3. Two-Phase Visualization

To delineate the origin and development of flooding in PEFC, recent research has resorted to two-phase visualization techniques. This can be done either through a transparent cell based on optical diagnostics or a graphite/metal cell visualized by neutron transmission radiography (NR). Bellows et al.[122] made the first attempt to measure the water content profile within a polymer membrane using NR. Owing to the NR limitation in spatial resolution, a thick membrane of 500 μm was used. Geiger et al.[123] reported the two-phase flow patterns observed by NR in the flow field for the first time. Preliminary results of two-phase distributions in both PEFC and DMFC were given; however, the spatial resolution in the presented radiographs appeared inadequate. In addition, Geiger et al. discussed the NR limitation in temporal resolution due to the necessity to use a CCD camera to detect time-dependent processes instead of recording still images to a film with sufficiently long exposure time.

To achieve sufficient spatial and temporal resolution, critical to the capture of two-phase flow phenomena in PEFC that is transient in nature and controlled by surface forces, a parallel effort is currently being made in optical diagnostics. Tuber et al.[124] attempted to visualize two-phase flow using a transparent test cell made of plexiglass. The cell design and experimental technique are limited to room temperature (~30 °C) and low current density (~300 mA/cm²) conditions. Under these conditions it was observed that clogging of gas channels by liquid water is a major cause for low cell performance. In this operating regime a hydrophilic GDL tends to enhance the cell performance. It should be noted that the same conclusion cannot be extrapolated to auto-

motive fuel cells that feature quite different operating temperature and current density. It is more difficult to visualize two-phase flow and liquid water dynamics in an automotive PEFC operated at higher current densities (~1 A/cm²) and higher temperatures, due largely to severe fogging.[125] Figure 33a shows the polarization characteristics of this transparent fuel cell under typical automotive conditions.[125] Apparently the reasonable electrochemical performance is preserved in this transparent cell. Figure 33b shows a series of normal-view snapshots of water droplet emergence on the GDL surface, growth, coalescence, and removal as liquid film from the sidewall. Observations of the droplet formation on GDL surface reveal a highly transient, cyclic process—water droplets emerge from certain locations from the GDL surface, then grow and sometimes coalesce into a larger drop. When the large drop reaches a size comparable with the channel dimension, it touches the hydrophilic channel wall in the flow field and spreads laterally along it into a thin liquid film. The liquid film becomes continuous and flows toward the exit of the gas channel under the influence of gas shear force. New droplets then form and grow on nearly the same spots of GDL, repeating the cyclic process. However, on the cell scale, a large number of droplets would exist on a sufficiently large surface at any one time, each having its own history of emergence, growth, and removal. Thus, one can anticipate an average current density that is essentially at steady state for a given set of operating conditions.

The visualization study of Yang et al.[125] further revealed the profound effects of wetting properties of gas channel walls. In a gas channel surrounded by mixed hydrophilic channel surfaces and hydrophobic GDL surface, it was found that water conden-
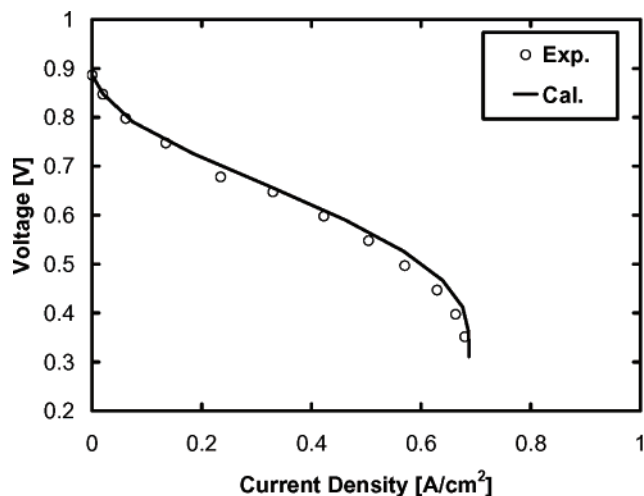
(a) comparison in average polarization curve
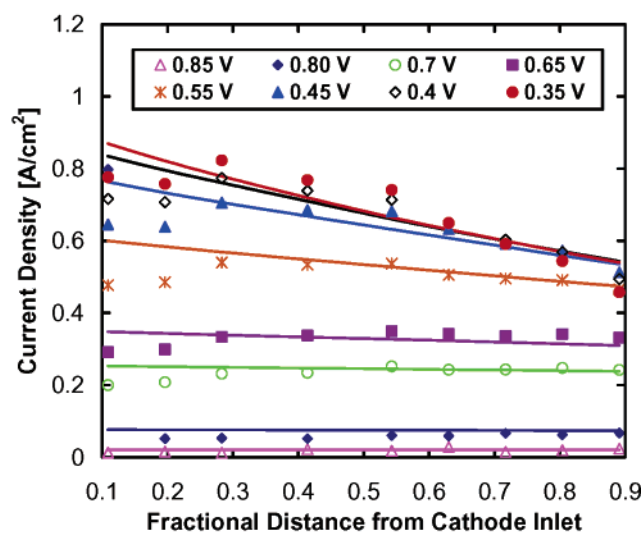
(b) comparison in the current distributions

Figure 34. Comparison of calculation (lines) and experimental (symbols) results for cathode stoichiometry of 2.0 at 0.75 A/cm² and fully humidified anode and cathode: (a) average polarization curve and (b) current distribution. Different colors in panel b represent various cell voltages as defined in the figure legend.[6]

sation occurs preferentially on hydrophilic surfaces, thus giving rise to an opportunity to keep condensation sites away from the GDL by properly tailoring the wetting characteristics of the channel walls and hence alleviate GDL flooding.

3.8.4. Experimental Validation

While highly sophisticated CFCD simulations are capable of predicting many details, to date model validation has been conducted mostly against the cell global polarization (or $I-V$) curve, which is an integral outcome of many interacting phenomena. Ju and Wang[6] made the first attempt to validate a three-dimensional, single-phase, isothermal PEFC model against current distribution data measured in a 50 cm² fuel cell operated with fully humidified gas feed. Figure 34 shows validation results with a cathode stoichiometry of 2.0 at 0.75 A/cm². An excellent match with the average $I-V$ curve can be seen between the
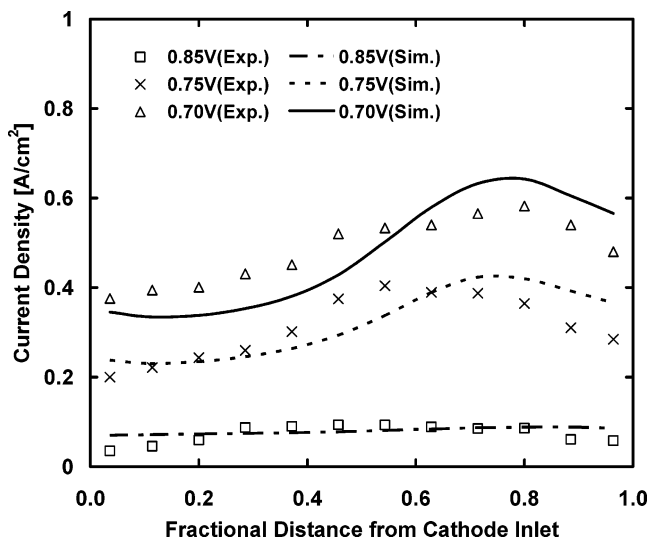
Figure 35. Comparison between simulated and measured current distributions in a PEFC with 15 μm membrane (EW < 1000) and under anode and cathode conditions of 3/3 bar, 1.2/2 stoichiometry, and 75%/0% relative humidity. The cell temperature is 80 °C.[100]

simulation and experiment; however, agreement with the current distribution remains unsatisfactory. Reasons for the discrepancy at the current distribution level were then analyzed, leading to improvement in the fundamental understanding of many complex, interacting phenomena occurring in a PEFC. Validation against global $I-V$ curves is insufficient and often misleading.

Detailed validation for low humidity PEFC, where the current distribution is of more interest and likely leads to discovery of optimal water management strategies, was performed most recently.[100] Figure 35 shows a comparison of simulated and measured current density profiles at cell potentials of 0.85, 0.75, and 0.7 V in a 50 cm² cell with anode and cathode RH of 75% and 0%. Both experimental data and simulation results display the characteristics of a low humidity cell: the local current density increases initially as the dry reactants gain moisture from product water, and then it decreases toward the cathode outlet as oxygen depletion becomes severe. The location of the peak current density is seen to move toward the cathode inlet at the lower cell potential (i.e., 0.7 V) due to higher water production within the cell, as expected.

The current state of experimental validation is to validate comprehensive CFCD models against distribution data of multiple parameters, such as current and species distributions. This possibility is becoming a reality as a new experimental technique to measure current and species (e.g., water) distributions simultaneously has emerged.[120] The trend will continue to validate CFCD models against multiple arrays of distribution data in order to develop a full understanding of PEFC fundamentals.

3.9. Modeling the Catalyst Layer at Pore Level

The catalyst layer of thickness around 10 μm is a critical component of a PEFC and requires more elaborative treatment. Gottesfeld and Zawodzinski[30]

provided a good overview of the catalyst layer structure and functions. The oxygen reduction reaction (ORR) occurs in the cathode catalyst layer, and the hydrogen oxidation reaction (HOR) takes place in the anode catalyst layer. Both reactions require active catalyst sites to break the molecular bond in the diatomic gaseous reactant molecules because of the low-temperature environment of a PEFC. HOR has orders of magnitude higher reaction rate than ORR, which leaves ORR as a source of large voltage loss in PEFC. Due to the acid nature of the polymer electrolyte and low-temperature operation, Pt- or Pt-alloys are the best-known catalysts. To enable ORR in the cathode catalyst layer, the layer must provide access for oxygen molecules, protons, and electrons. Therefore, the catalyst layer usually consists of: (1) the ionomer (its amount is also called Nafion content, ϵ_e) to provide a passage for protons to be transported in or out, (2) metal catalysts supported on carbon (the electronic phase volume fraction, ϵ_s) to provide a means for electron conduction, and (3) sufficient porosity (ϵ_g) for the O_2 gas to be transferred to catalyzed sites. The sum of all volume fractions is equal to unity, and individual volume fractions must be optimized to provide the best overall performance of a catalyst layer.

The important processes occurring in a catalyst layer include interfacial ORR at the electrochemically active sites, proton transport in the electrolyte phase, electron conduction in the electronic phase (i.e., Pt/C), and oxygen diffusion through the gas phase, liquid water, and electrolyte phase.

In most of the macroscopic models reported in the literature the active catalyst layer was not the main point of interest but rather treated either as an infinitely thin interface or a macrohomogeneous porous layer. There were a few detailed models specifically developed for PEFC catalyst layers based on the theory of volume averaging. In this field distinction is further made between a homogeneous approach, a film model, and an agglomerate model. The homogeneous model assumes the catalyst layer to be a two-phase system consisting of ionic and electronic phases only, without gas voids. The gaseous reactant transports through the catalyst layer via the electrolyte phase as a dissolved species, and thus the diffusion rate is poor. In the film model gas pores are assumed to exist along with the electronic particles covered by a thin film of polymer electrolyte. On the other hand, the agglomerate model considers gas pores to surround agglomerates consisting of electrolyte films and electronic particles, i.e., a three-phase system. Depending on the pore geometry, agglomerates are planar, cylindrical, and spherical. Nonetheless, all three models belong to the macroscopic theory for multiphase systems in which there is neither resolution to capture pore-level phenomena nor ability to assess the morphological effects.

Springer and Gottesfeld,[126] Perry et al.,[127] and Eikerling and Kornyshev[128] presented several analytical and numerical solutions for the cathode catalyst layer under various conditions. Perry et al. studied the effects of mass-transport limitations on the polarization characteristics of a reaction obeying

Tafel kinetics and predicted a doubling of the Tafel slope as the current density increases or the mass-transport limitations set in. Eikerling and Kornyshev presented analytical expressions in the limiting cases of small currents, fast oxygen diffusion, fast proton transport, and high currents. To verify the theoretical finding regarding the existence of double Tafel slopes, Ihonen et al.[129] most recently performed an experimental study of mass-transport limitations in the PEFC cathode catalyst layer. A kinetic slope at low current densities and a second Tafel slope at higher current densities were indeed observed on the polarization curves. The experimental evidence appears to suggest that oxygen diffusion is limited in the agglomerates at the pore scale rather than by that in the gas phase across the thickness of the electrode.

However, the above-mentioned macroscopic models do not address localized phenomena on the pore level. To assess the profound effects of the catalyst layer pore structure on polarization performance, Pisani et al.[130] constructed a pore-level model by volume-averaging microscopic governing equations over an idealized, one-dimensional model geometry of pores. Wang and Wang[131] recently developed a direct numerical simulation (DNS) model to describe the transport of protons, electrons, oxygen, and product water at the pore level (on the order of 100 nm) within a random, microscopically complex catalyst layer. This DNS model is based on a numerical mesh created from either a digitized catalyst layer micrograph or a computer-generated random pore structure according to the prescribed porosity and average pore size. Subsequently, direct simulation of reactant and product transport with reaction is performed on this digital microstructure at the pore level. Such a DNS model can be used as an alternative to experimental trial-and-error for the optimization of compositions and microstructure of a high-performance catalyst layer. Figure 36 shows DNS predictions of the cathode voltage loss as a result of kinetic polarization, ohmic polarization, and mass-transport polarization for a commonly used catalyst layer composition (circles), an optimized design (squares), and a less optimal design (triangles). The three-dimensional contour of O_2 concentration on the right illustrates that the less optimized design exhibits restrictive oxygen transport into the catalyst layer due to a too small porosity.

3.10. Summary and Outlook

Table 2 summarizes and compares the main features of representative CFD models reviewed in this section for PEFCs. It is evident that rapid advances in PEFC modeling over the past 5 years have yielded considerable predictive capabilities. Fully three-dimensional, electrochemical−transport−thermal coupled, and realistic large-scale simulations are possible with today's computing power. A major focus of future research in PEFC modeling will be on liquid water transport and ensuing flooding phenomena. Much remains to be learned about the fundamental physical process of flooding occurrence. Advanced diagnostics, such as visualization by optical diagnostics and 3-D neutron tomography, as well as detailed
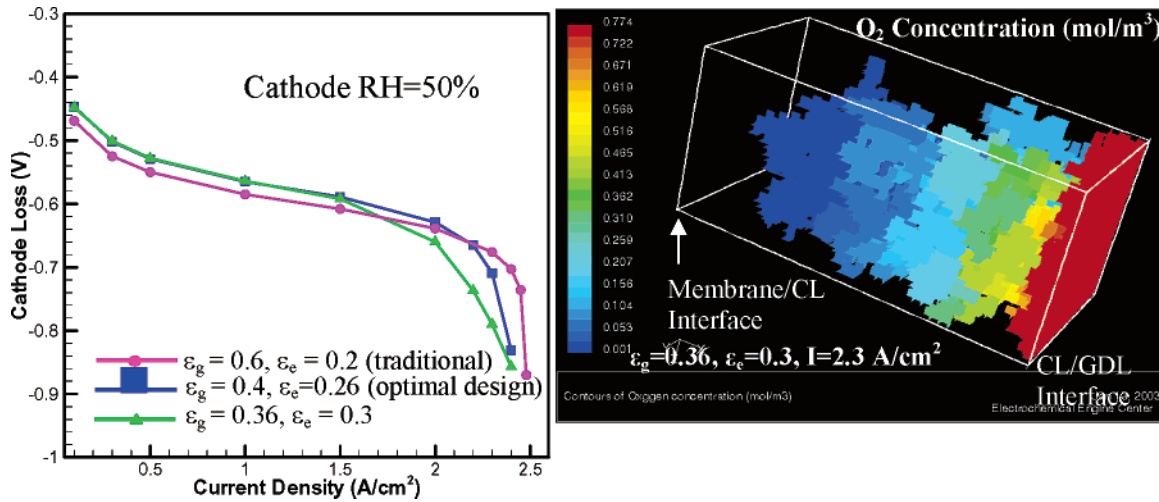
Figure 36. Cathode voltage loss as predicted by direct numerical simulation of proton, oxygen, and water transport in a catalyst layer at the pore level (left), and three-dimensional oxygen concentration contours in a random microstructure of the catalyst layer (right).[131]

**Table 2. Comparisons of Representative CFD Models for Polymer Electrolyte Fuel Cells (PEFCs)**

Model Features	CFDRC	Fluent	Penn State U.	STAR-CD Japan	STAR-CD N. America	U. Kansas	U. Miami	U. South Carolina	U. Victoria
Domain Meshed									
Catalyst layers	✓	✓	✓	✓	×	×	✓	×	×
Membrane	✓	✓	✓	✓	×	×	✓	×	✓
Gas diffusion layers	✓	✓	✓	✓	✓	✓	✓	✓	✓
Gas channels	✓	✓	✓	✓	✓	×	✓	✓	✓
Approach/Assumptions									
Species variable	mass fraction	mass fraction	molar conc./mass fraction	molar conc. /mass fraction	mass fraction	mole fraction	mole/mass fraction	mass fraction	mass fraction
Density	variable	variable	variable/constant	variable	variable	N/A	constant	variable	variable
Mass source/sink in continuity equation	×	✓	✓	✓	✓	×	×	✓	×
Physics Included									
CL ohmic loss	✓	✓	✓	✓	×	×	✓	×	×
CL transport loss	✓	✓	✓	✓	×	×	✓	×	×
Water transport thru membrane	×	×	✓	✓	✓ (w/ const. properties)	×	×	✓ (w/ const. properties)	×
Electron transport	✓	✓	✓	✓	×	×	×	×	×
Contact resistance	×	✓	✓	✓	×	×	×	×	×
Non-isothermal	×	×	✓	✓	✓·	×	✓	✓	✓
Two-phase flow in GDL	M^2 Model	×	M^2 Model	M^2 Model	×	UFT Model	M^2 Model	×	UFT Model
GDL hydrophobic effects	×	×	✓	✓	×	×	×	×	×
Two-phase flow model in channels	mist flow	×	mist flow & annular film	mist flow	×	×	×	×	un-specified
References/Notes	63, 73	90	55, 59, 14, 64, 67, 81	based on PSU model	based on SC model	69-71	54, 72	57, 58, 60	62, 74

distribution measurements, are critically needed in order to paint a clear picture of how flooding occurs and what are the controlling factors. Once a physical understanding of the flooding process is established, the challenge will turn to how to model and simulate such a complex two-phase flow process with strong interactions with the GDL surface and channel walls.

4. Direct Methanol Fuel Cells

A DMFC is an electrochemical cell that generates electricity based on the oxidation of methanol and reduction of oxygen. Figure 37 illustrates the cell construction and operating principle of a DMFC. An aqueous methanol solution of low molarity acts as the reducing agent that traverses the anode flow field. Once inside the flow channel, the aqueous solution diffuses through the backing layer, comprised of carbon cloth or carbon paper. The backing layer collects the current generated by the oxidation of aqueous methanol and transports laterally to a land in the current collector plate. The global oxidation reaction occurring at the platinum−ruthenium catalyst of the anode is given by

$$CH_3OH + H_2O \rightarrow CO_2 + 6H^+ + 6e^-$$
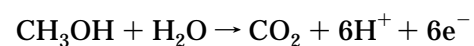
The carbon dioxide generated from the oxidation
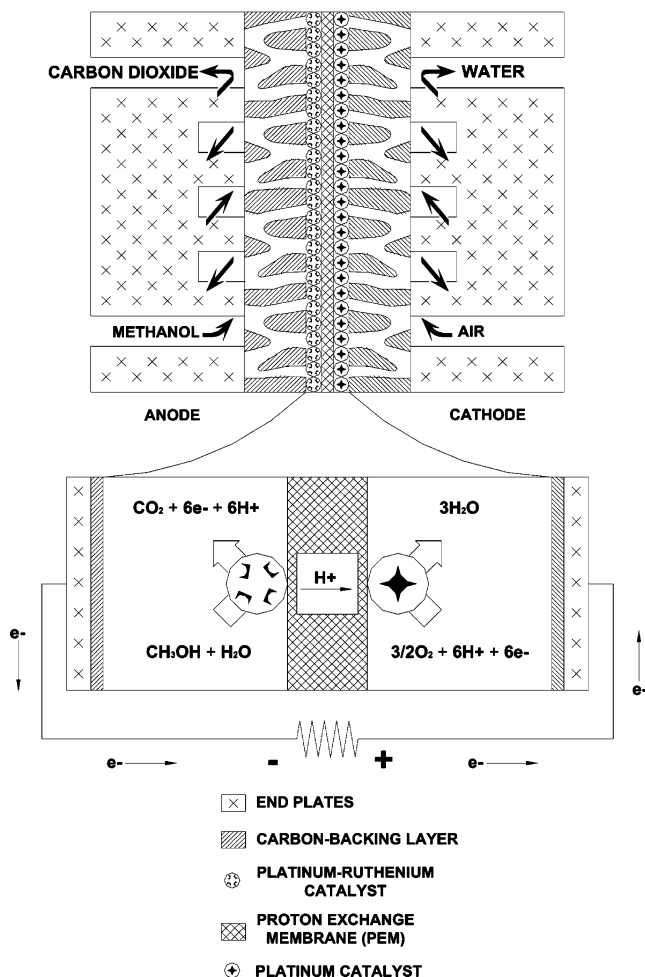
Figure 37. Operating schematic of a direct methanol fuel cell (DMFC).

reaction emerges from the anode backing layer as bubbles and is removed via the flowing aqueous methanol solution.

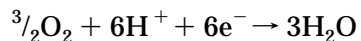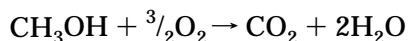Air is fed to the flow field on the cathode side. The oxygen in the air combines with the electrons and protons at the platinum catalyst sites to form water. The reduction reaction taking place on the cathode is given by

$$^3/_2O_2 + 6H^+ + 6e^- \rightarrow 3H_2O$$

The two electrochemical reactions are combined to form an overall cell reaction as

$$CH_3OH + {}^3/_2O_2 \rightarrow CO_2 + 2H_2O$$

Extensive work on DMFC has been conducted by many groups, notably Halpert et al.[132] of Jet Propulsion Laboratory (JPL) and Giner, Inc., Baldauf and Preidel[133] of Siemens, Ren et al.[134] of Los Alamos National Laboratory (LANL), Scott and co-workers[135-137] of the University of Newcastle upon Tyne, and Wang and co-workers[111,138-141] of the Pennsylvania State University. A comparative study of DMFC with hydrogen PEFC was presented by the LANL group.[134,142] A DMFC requires platinum−ruthenium and platinum loadings roughly five times higher to achieve power densities of 0.05−0.30 W/cm².

A number of extensive reviews have been published as the DMFC research activities has grown nearly exponentially worldwide in recent years. Gottesfeld and Zawodzinski[30] briefly summarized research at Los Alamos intended for transportation application and pointed out areas for improvement if DMFC technology is to become a serious power plant candidate for transportation. Among them, reducing catalyst loading to be competitive with reformed/air fuel cells is perhaps a great challenge and a difficult task for the foreseeable future. In a later book chapter, Gottesfeld and Wilson[142] discussed perspectives of DMFC for portable applications. Lamy et al.[143] provided an in-depth review of DMFC fundamentals, including the reaction mechanisms of methanol oxidation, use of various binary and ternary electrocatalysts, effects of electrode structure and composition on the activity of methanol oxidation, and development of proton conducting membranes with low methanol crossover. It was projected that DMFC will be first commercialized as portable power sources before the year 2010 and that there will be a quantum jump on the technology to be in a position to drive DMFC-powered vehicles 10 years thereafter. Arico et al.[144] reviewed recent advances in DMFC from both fundamental and technological (for portable power) aspects. The fundamental aspects of DMFC reviewed by Arico et al. were concerned with electrocatalysis of methanol oxidation and oxygen reduction in the presence of methanol crossed over from the membrane, and the technological aspects were focused on the proton conducting membranes as well as techniques for fabricating MEA. Neergat et al.[145] provided an excellent review of new materials for DMFC, including novel proton conducting membranes and electrocatalysts. Narayanan et al.[146] and Muller et al.[147] discussed, in detail, the paramount importance of water balance for a portable DMFC system.

4.1. Technical Challenges

As expected, a DMFC exhibits lower power densities than that of a H₂/air PEFC. At present, the H₂/air PEFC requires anode and cathode platinum loadings of less than 1 mg/cm² to achieve power densities of 0.6−0.7 W/cm². However, DMFC has the advantages of easier fuel storage, no need for cooling or humidification, and simpler design. Thus, DMFC is presently considered a leading contender for portable power. To compete with lithium-ion batteries, the first and foremost property of a portable DMFC system is a higher energy density in Wh/L. This requirement entails four key technical challenges to be overcome: (1) low rate of methanol oxidation kinetics on the anode, (2) methanol crossover through the polymer membrane, (3) innovative water management, and (4) heat management.

4.1.1. Methanol Oxidation Kinetics

Combined with methanol crossover, slow anode kinetics lead to a power density of a DMFC that is three to four times lower than that of a hydrogen fuel cell. Much work has been focused on the anodic oxidation of methanol.[148] The mechanism of the

electrocatalytic oxidation of methanol at anode was postulated.[149,150] Different anode catalyst structures of Pt−Ru were developed,[151] and several anode catalysts other than Pt−Ru were explored.[152−154] Additionally, the effects of the anode electrochemical reaction on cell performance were experimentally studied.[19,155,156] Lamy et al.[143] and Arico et al.[144] provided extensive reviews of the most recent work on electrocatalysis. More active catalysts for methanol oxidation enable a certain power density to be realized at higher cell voltage and hence directly impact the energy efficiency of the cell, which translates to the energy density if the amount of fuel carried by a DMFC system is fixed.

4.1.2. Methanol Crossover

Methanol crossover occurs due to the inability of the commonly used perfluorosulfonic acid (PFSA) membrane to prevent methanol from permeating its polymer structure. Diffusion and electro-osmotic drag are the prime driving forces for methanol to transport through the polymer membrane and eventually react with platinum catalyst sites on the cathode, leading to a mixed potential on the cathode. This mixed potential on the cathode causes a decrease in cell voltage. Methanol reaching the cathode also results in decreased fuel efficiency, thus lowering the energy density.

Methanol crossover in DMFC has been extensively studied both experimentally and theoretically. Narayanan et al.[157] and Ren et al.[158] measured the methanol crossover flux with different membrane thickness and showed that the methanol crossover rate is inversely proportional to membrane thickness at a given cell current density, thus indicating that diffusion is dominant. In addition, Ren et al.[159] compared diffusion with electro-osmotic drag processes and demonstrated the importance of electro-osmotic drag in methanol transport through the membrane. In their analysis, methanol electro-osmotic drag is considered a convection effect and the diluted methanol moves with electro-osmotically dragged water molecules. Valdez and Narayanan[160] studied the temperature effects on methanol crossover and showed that the methanol crossover rate increases with cell temperature. Ravikumar and Shukla[156] operated the liquid-feed DMFC at an oxygen pressure of 4 bar and found that cell performance is greatly affected by methanol crossover at methanol feed concentrations greater than 2 M and that this effect aggravates with the operating temperature. Wang et al.[161] analyzed the chemical compositions of the cathode effluent of a DMFC with a mass spectrometer. They found that the methanol crossing over the membrane is completely oxidized to CO_2 at the cathode in the presence of Pt catalyst. Additionally, the cathode potential is influenced by the mixed potential phenomenon due to simultaneous methanol oxidation and oxygen reduction as well as poisoning of Pt catalysts by methanol oxidation intermediates. Kauranen and Skou[162] presented a semiempirical model to describe the methanol oxidation and oxygen reduction reactions on the cathode and concluded that the oxygen reduction current is reduced in the presence of methanol oxidation due to surface poisoning.

Developing novel membranes with low methanol crossover would surely increase cell performance and fuel efficiency.[143,145] Alternatively, Wang and co-workers[139,140,163] proposed modifying the anode backing structure to mitigate methanol crossover. It was demonstrated that a compact microporous layer can be added in the anode backing to create an additional barrier to methanol transport, thereby reducing the rate of methanol crossing over the polymer membrane. Both practices to control methanol crossover by increasing mass-transfer resistance, either in the anode backing or in the membrane, can be mathematically formulated by a simple relation existing between the crossover current, I_c, and anode mass-transport limiting current, $I_{A,lim}$. That is

$$I_c = I_{c,oc}\left(1 - \frac{I}{I_{A,lim}}\right) \qquad (26)$$

where $I_{c,oc}$ is the crossover current at open circuit and I the operating current. In the conventional approach using thick membranes with low methanol crossover, $I_{c,oc}$ is low and $I_{A,lim}$ is set to be high. In contrast, setting up a barrier in the anode backing is essentially reducing the anode limiting current, $I_{A,lim}$, and making the open-circuit crossover current, $I_{c,oc}$, a significant fraction of $I_{A,lim}$, i.e., 50−80%. Two immediate advantages result from this latter cell design principle. One is that more concentrated fuel can be used, thus leading to the much higher energy density of the DMFC system. Lu et al.[140] successfully demonstrated the use of 8 M methanol solution as the anode feed, and Pan[163] most recently reported a DMFC operated with 10 M (or 30 vol %) methanol fuel solution. Second, this type of DMFC permits use of thin membranes such as Nafion 112, which greatly facilitates water back flow from the cathode to anode,[140,164] thus addressing another major challenge of portable DMFC to be discussed below.

4.1.3. Water Management

Water management emerges as a new significant challenge for portable DMFC systems. Constrained by the methanol crossover problem, the anode fuel solution has been very dilute, meaning that a large amount of water needs to be carried in the system, therefore reducing the energy content of the fuel mixture. In addition, for each mole of methanol, 1 mol of water is needed for methanol oxidation at the anode and 2.5×6 mol of water is dragged through a thick membrane such as Nafion 117 toward the cathode, assuming that the electro-osmotic drag coefficient of water is equal to 2.5 per proton. This then causes 16 water molecules lost from the anode for every mole of methanol. Water in the anode therefore must be replenished. On the other hand, inside the cathode, there are 15 water molecules transported from the anode and additionally 3 water molecules produced by consuming six protons generated from oxidation of one methanol. The presence of a large amount of water floods the cathode and reduces its performance. The difficult task of removing water from the cathode to avoid severe flooding and supplying water to the anode to make up water

loss due to electro-osmotic drag through the membrane is referred to as innovative water management in a portable DMFC.

Traditionally, a high cathode gas flow rate (high stoichiometry) is employed to prevent flooding. This strategy not only increases parasitic power consumption but also removes excessive water from the fuel cell, making external water recovery more difficult. How to minimize water removal from the cathode and subsequent recovery externally to replenish the anode without causing severe cathode flooding becomes an important engineering issue. A greater understanding and ability to tailor water flow in the cell is of fundamental interest for portable DMFC systems. This is an area where DMFC models play an important role.

4.1.4. Heat Management

Thermal management in a DMFC is intimately tied to water and methanol-transport processes. First, heat generation in a DMFC is much higher than a H$_2$/air PEFC due to a much lower energy efficiency (it is only 20−25% when the cell is operated between 0.3 and 0.4 V). That is, for a 20 W DMFC system, 60−80 W of waste heat is produced. The waste heat is typically removed from DMFC by liquid fuel on the anode side and water evaporation on the cathode side. The latter also determines the amount of water loss from a DMFC and the load of water recovery by an external condenser. Therefore, while a higher cell temperature promotes the methanol oxidation reaction, it may not be practically feasible from the standpoint of water evaporation loss. Moreover, the higher cell temperature increases the methanol crossover rate, thereby reducing the fuel efficiency and system energy density.

4.2. DMFC Modeling

4.2.1. Needs for Modeling

While attempts continue to elucidate the fundamental electrochemical reaction mechanisms, explore new compositions and structures of catalysts, and develop new membranes and methods to prevent methanol crossover, important system issues relevant to DMFC are emerging, such as water management, gas management, flow-field design and optimization, and cell up-scaling for different applications. A number of physicochemical phenomena take place in a liquid-feed DMFC, including species, charge, and momentum transfer, multiple electrochemical reactions, and gas−liquid two-phase flow in both anode and cathode. Carbon dioxide evolution in the liquid-feed anode results in strongly two-phase flow, making the processes of reactant supply and product removal more complicated. All these processes are intimately coupled, resulting in a need to search for optimal cell design and operating conditions. A good understanding of these complex, interacting phenomena is thus essential and can most likely be achieved through a combined mathematical modeling and detailed experimental approach. It is apparent that three of the four technical challenges discussed in section 4.1 for portable DMFC systems require a basic understanding of methanol, water, and heat-transport processes occurring in a DMFC. This provides a great opportunity to exercise fundamental modeling.

Another good problem for modeling is the micro-DMFC system. Both anode carbon dioxide blockage and cathode flooding are especially acute in micro-systems due to the small channel length scale involved, low operating temperature, dominance of surface tension forces, and requirement for low parasitic power losses in these systems.[165−169]

In addition, DMFC is a system requiring a high degree of optimization. There are a multitude of operating parameters affecting the performance of a DMFC. These variables include cell temperature, molarity of aqueous methanol solution, cathode pressure, anode and cathode stoichiometry, and flow-field design. Higher cell temperatures improve catalytic activity, but the water loss from the cathode increases. Efficient removal of carbon dioxide gas bubbles and liquid water produced on the anode and cathode, respectively, must be maintained to allow reactants to reach catalyst sites. Removal of carbon dioxide "slugs" and prevention of cathode "flooding" can be attained by increasing flow rates. However, increasing flow rates requires more pumping power. Too high a flow rate on the cathode will dry out the polymer membrane, decreasing proton conductivity and hence cell performance. An understanding of the interdependence of these parameters plays a key role in optimizing the performance of a DMFC.

DMFC modeling thus aims to provide a useful tool for the basic understanding of transport and electro-chemical phenomena in DMFC and for the optimization of cell design and operating conditions. This modeling is challenging in that it entails the two-phase treatment for both anode and cathode and that both the exact role of the surface treatment in backing layers and the physical processes which control liquid-phase transport are unknown.

4.2.2. DMFC Models

In the literature, Scott et al.[170−172] developed several simplified single-phase models to study transport and electrochemical processes in DMFC. Baxter et al.[173] developed a one-dimensional mathematical model for a liquid-feed DMFC anode. A major assumption of this study was that carbon dioxide is only dissolved in the liquid, and hence, their anode model is a single-phase model. Using a macrohomogeneous model to describe the reaction and transport in the catalyst layer of a vapor-feed anode, Wang and Savinell[174] simulated the effects of the catalyst layer structure on cell performance. Kulikovsky et al.[175] simulated a vapor-feed DMFC with a two-dimensional model and compared the detailed current density distributions in the backing, catalyst layer, and membrane of a conventional to a new current collector. In another paper, Kulikovsky[176] numerically studied a liquid-feed DMFC considering methanol transport through the liquid phase and in hydrophilic pores of the anode backing. In both publications of Kulikovsky the important phenomenon of methanol crossover was ignored. Dohle et al.[177] presented a one-dimensional model for the vapor-feed DMFC and

included the crossover phenomenon. The effects of methanol concentration on the cell performance were studied.

In a three-part paper[178−180] Meyers and Newman developed a theoretical framework that describes the equilibrium of multicomponent species in the membrane. The transport of species in the membrane based on concentrated-solution theory and membrane swelling were taken into consideration in their model. The transport phenomena in the porous electrodes were also included in their mathematical model. However, the effect of pressure-driven flow was not considered. In addition, the transport of carbon dioxide out of the anode was neglected by assuming that the carbon dioxide is dilute enough to remain fully dissolved in liquid. Nordlund and Lindbergh[181] studied the influence of the porous structure on the anode with mathematic modeling and experimental verification. In their model they also assumed that carbon dioxide does not evolve as gas within the electrode. Recently, Wang and Wang[182] presented a two-phase, multicomponent model. Capillary effects in both anode and cathode backings were accounted for. In addition to the anode and cathode electrochemical reactions, the model considered diffusion and convection of both gas and liquid phases in backing layers and flow channels. The model fully accounted for the mixed potential effect of methanol oxidation at the cathode as a result of methanol crossover caused by diffusion, convection, and electroosmosis. The model of Wang and Wang was solved using a finite-volume technique and validated against experimental polarization curves. The model results indicated the vital importance of gas-phase transport in the DMFC anode.

Divisek et al.[183] presented a similar two-phase, two-dimensional model of DMFC. Two-phase flow and capillary effects in backing layers were considered using a quantitatively different but qualitatively similar function of capillary pressure vs liquid saturation. In practice, this capillary pressure function must be experimentally obtained for realistic DMFC backing materials in a methanol solution. Note that methanol in the anode solution significantly alters the interfacial tension characteristics. In addition, Divisek et al.[183] developed detailed, multistep reaction models for both ORR and methanol oxidation as well as used the Stefan−Maxwell formulation for gas diffusion. Murgia et al.[184] described a one-dimensional, two-phase, multicomponent steady-state model based on phenomenological transport equations for the catalyst layer, diffusion layer, and polymer membrane for a liquid-feed DMFC.

Despite the fact that much effort has been made to model the DMFC system, considerable work remains, particularly in support of the emerging portable designs and systems. Few have treated the dominating effects of two-phase flow. No model to date has sufficient detail to provide a microfluidic theory for portable systems including effects of channel geometry and wettability characteristics of the GDL on fluid flow in the anode or cathode. Modeling studies are needed to fully elucidate the intricate couplings of methanol, water, and heat-transport processes. This understanding is key to successful design and operation of portable DMFC systems. Finally, the important role of a microporous layer in DMFC and its tailoring to control the flow of methanol and water remain unknown.

4.3. Experimental Diagnostics

Similarly, experimental diagnostics are an important component of advanced modeling and simulation of DMFCs. Diagnostic techniques for DMFCs have included the following: (1) cyclic voltammetry (CV) to determine the electrochemically active area of the cathode, (2) CO stripping to determine the electrochemically active area of the anode, (3) electrochemical impedance spectroscopy (EIS), (4) anode polarization characterization via a MeOH/H$_2$ cell as proposed by Ren et al.,[19] (5) methanol crossover rate measurement by CO$_2$ sensing in the cathode (via FITR, GC, or infrared CO$_2$ sensors) or measuring the limiting current in a MeOH/N$_2$ cell (Ren et al.[19]), (6) current distribution measurements via a segmented cell in conjunction with a multichannel potentiostat (Mench and Wang[111]), (7) material balance analysis of CH$_3$OH and H$_2$O (Narayanan et al.[146] and Muller et al.[147]), and (8) two-phase visualization of bubble dynamics[185−187] on anode and liquid droplet dynamics on cathode.[187] The work in the last three areas is briefly reviewed in this review as they are particularly pertinent to the fundamental modeling of DMFC for cell design and optimization.

Mench and Wang[111] described an experimental technique to measure current distribution in a 50 cm^2 instrumented DMFC based on multichannel potentiostat. In this method separate current collector ribs are embedded into an insulating substrate (e.g., Lexan plate) to form a segmented flow-field plate. The resulting flow-field plates for both anode and cathode are then assembled with a regular MEA to form a fuel cell with independently controllable subcells. All subcells are connected to a multichannel potentiostat to undergo potentiostatic experiments simultaneously. The subcell currents measured thus provide information on the current density distribution for the full-scale fuel cell. The spatial and temporal resolution of this method depends on the number of channels available and capabilities of the potentiostat. Current density distribution measurements were made for a wide range of cathode flow rates in order to elucidate the nature of cathode flooding in a DMFC. Figure 38 displays the current density distributions for high and low cathode air flow rates. In the case of high cathode stoichiometry (Figure 38a), it can be seen that the current distributes rather uniformly for all three levels of cell voltage. As expected, the current density increases as the cell voltage decreases. In the case of low cathode stoichiometry (still excessive for the oxygen reduction reaction), Figure 38b clearly shows that a portion of the cathode toward the exit is fully flooded, leading to almost zero current. The information provided in Figure 38 can be used to identify innovative cathode flow-field designs and enables the development of MEA structures with improved water management capabilities.
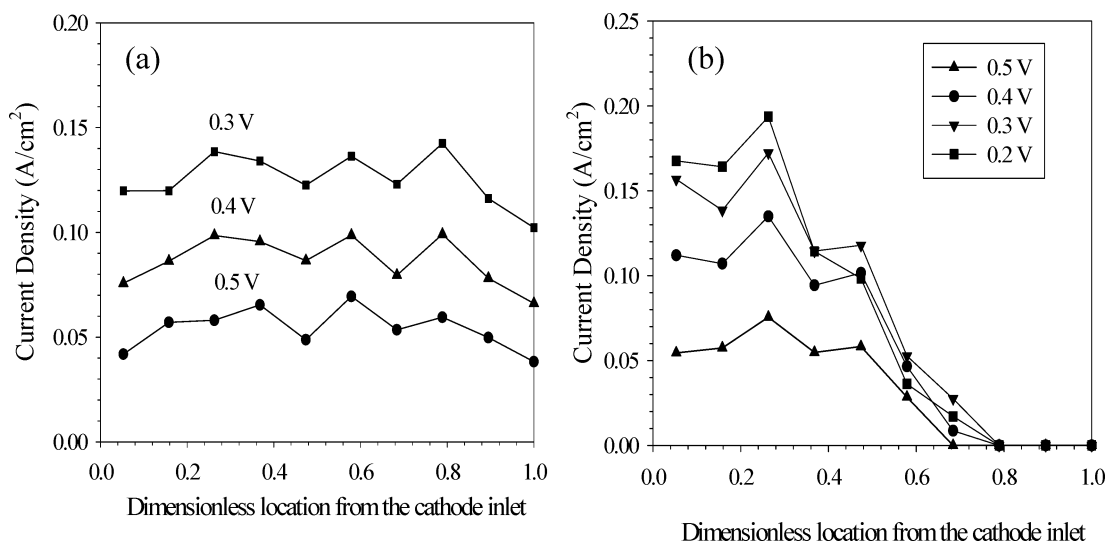
Figure 38. Current density distributions in a 50 cm² DMFC for (a) high cathode air flow rate (stoichiometry of 85 at 0.1 A/cm²) and (b) low cathode air flow rate (stoichiometry of 5 at 0.1 A/cm²).[111]

Material balance analysis proves to be a critical diagnostic tool for the development of portable DMFC systems. In this analysis methanol balance on the anode side along with the methanol crossover rate typically measured by an infrared CO_2 sensor is conducted. In addition, water balance on both anode and cathode sides is performed in which the cathode water amount is carefully collected by a moisture trap and measured.[146,147] From such analyses Müller et al.[147] revealed that the water balance on the DMFC anode is highly negative, thus calling for membrane development with low water crossover in addition to low methanol crossover.

Gas management on the anode side is an important issue in DMFC design. On the anode side, carbon dioxide is produced as a result of methanol electrochemical oxidation. If CO_2 bubbles cannot be removed efficiently, the anode channels will be blocked, leading to limited mass transport. Argyropoulos et al.[185,186] were perhaps the first to observe the two-phase flow pattern in the anode channel under various operating conditions. This flow visualization on the anode side yields a valuable understanding of bubble dynamics in DMFC. This study was, however, undertaken under low cell performance. Most recently, Lu and Wang[187] developed a carefully designed transparent DMFC to visualize bubble dynamics on the anode side and liquid droplet (and flooding) dynamics on the cathode. Moreover, Lu and Wang explored the profound effect of backing layer wettability on gas management in DMFC. Figure 39 shows a sequence of images taken at various times at a feed temperature of 85 °C and current density of 100 mA/cm². The images, 1 s apart, were captured from a movie with a time resolution of 1/30 s. The time of the first image was chosen arbitrarily due to the fact that two-phase flow is a regular, periodic event. As shown in Figure 39, the CO_2 bubbles emerge at certain locations and form large and discrete gas slugs in the channel. The bubble motion is governed by the momentum of liquid flow, force of buoyancy on the bubble, and surface tension between the bubble and substrate. It can be seen from Figure 39 that the bubbles are held on the carbon paper by strong surface tension until they
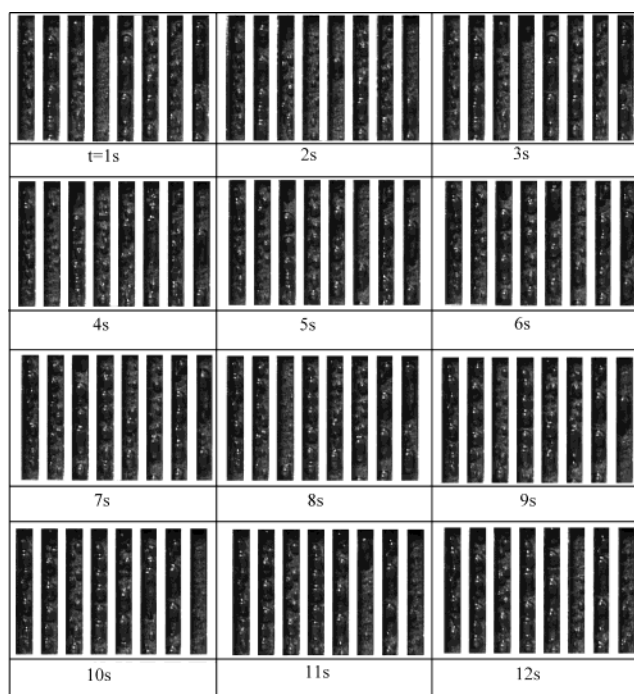

Figure 39. Images of bubble dynamics in the DMFC anode with carbon paper backing layer for 2 M MeOH feed and nonhumidified air at 100 mA/cm² and 85 °C.[187]

grow into larger slugs for detachment, clearly indicative of the dominant effect of surface tension in bubble dynamics in DMFC. Once the bubbles grow to a sufficient size, they detach and sweep along the backing surface in the channel. This sweeping process clears all small bubbles preexisting on the backing surface, making new bubbles grow from the smallest size to the full detachment diameter. As a result, the two-phase flow becomes regularly intermittent. The images shown in Figure 39, representative of most DMFC systems under commercial development, indicate the vital importance of considering two-phase flow and transport in a DMFC model.
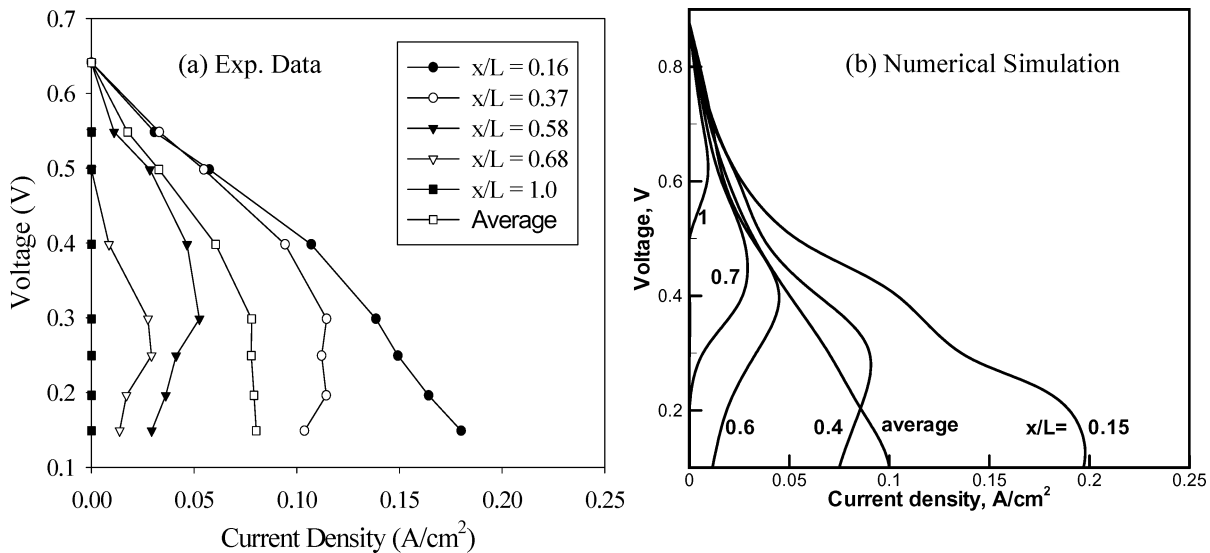
4.4. Model Validation

Experimental validation of the two-phase DMFC model of Wang and Wang[182] has been carried out for

(a) Temperature Effect

(b) Concentration Effect
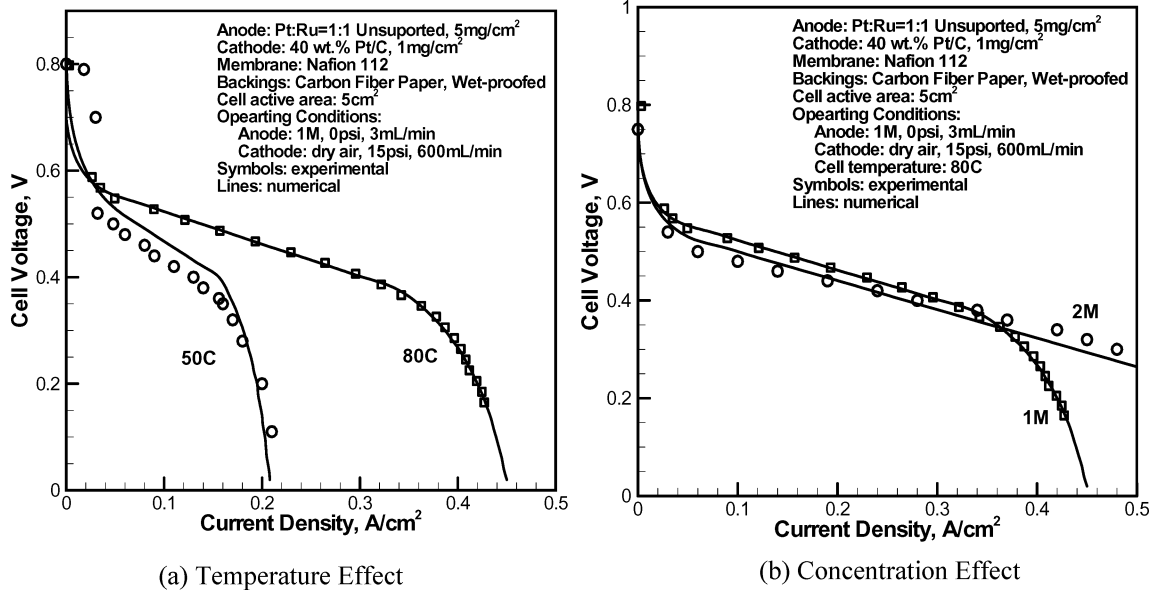
Figure 40. Comparisons of 2-D model predictions with experimental data for a DMFC with (a) temperature effect and (b) concentration effect.[182]


Figure 41. Comparison of localized polarization curves between experiments (a) and model predictions (b) for a 50 cm^2 DMFC with an anode flow stoichiometry of 27 and a cathode air stoichiometry of 5 at 0.1 A/cm^2.[5]

a 5 cm^2 graphite cell. A brief description of the cell geometry, MEA compositions, and operating conditions is given in Figure 40. Figure 40a illustrates the capability of the model to predict the polarization curves at two cell temperatures. Excellent agreement is achieved not only in the kinetic- and ohmic-controlled regimes of the polarization curves but also in the mass-transport-controlled regime, where the methanol oxidation kinetics is modeled as a zero-order reaction for molar concentrations above 0.1 M but a first-order reaction for a molarity below 0.1 M. This shift in the reaction order and molarity of transition is consistent with direct kinetics measurements. A lower mass-transport-limiting current density at 50 °C, seen in Figure 40a, is caused by the lower diffusion coefficients in both the liquid and gas phases and the lower saturation methanol vapor concentration in the gas phase at lower temperatures. Using the same model and property data, Figure 40b shows equally satisfactory agreement in

the polarization curves between numerical and experimental results for different methanol feed concentrations. In accordance with these experiments, the model prediction for the 2 M case shows a slightly lower performance (due primarily to higher methanol crossover) and an extended limiting current density. Similar success in validating global $I-V$ curves was also reported by Murgia et al.,[184] among others.

While the model validation against cell overall performance data has been satisfactory and encouraging, as evident from Figure 40, the ultimate test of these highly sophisticated two-phase models is comparison with detailed distribution measurements. Figure 41 presents such an attempt toward developing high-fidelity first-principles models for DMFC. Figure 41a shows a set of localized polarization curves measured using the current distribution measurement technique of Mench and Wang,[111] and Figure 41b displays the same set of polarization curves predicted from the DMFC two-phase model
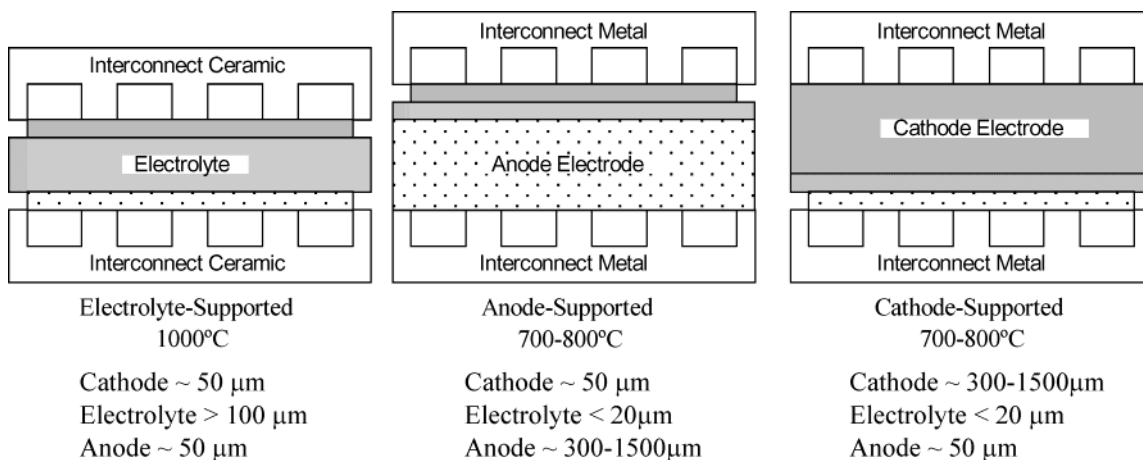
Figure 42. Various planar SOFC configurations (revised from ref 189).

of Wang and Wang.[182] A low air stoichiometry of 5 (although not low for the electrochemical reaction requirement) was deliberately chosen so that cathode GDL flooding may occur and a nonuniform current density distribution results.

The two graphs in Figure 41 share a qualitative similarity. For example, both experiment and model results indicate that the local polarization curves near the dry air inlet exhibit a monotonic function between the voltage and current. Also, the shape of the polarization curves near the exit, from both experiment and simulation, is clearly evidence of flooding in the cathode GDL. Another interesting observation is that the average cell polarization curves, measured and predicted, do not exhibit any sign of cathode flooding, indicating that detailed distribution measurements are absolutely required in order to discern complex physicochemical phenomena occurring inside the cell. Finally, it can be seen from Figure 41 that a satisfactory quantitative comparison between experiment and model is lacking on the detailed level.

Difficulties in obtaining good quantitative agreement between predicted and measured distribution results are indicative that model refinements as well as an improved property database will be needed before accurate quantitative predictions of not only overall polarization curve but also detailed distributions within a DMFC may be obtained.

4.5. Summary and Outlook

Two-phase modeling capabilities for DMFCs have emerged, which unravel the importance of gas-phase transport of methanol as compared to the liquid-phase transport. In addition, much effort is being directed toward developing a coupled model for methanol, water, and heat-transport processes occurring simultaneously in a DMFC. Such models are extremely useful for the discovery of unique design and operation regimes of the DMFC system for portable application, where the high energy density entails using highly concentrated methanol (preferably pure methanol), maintaining healthy water balance, controlling fuel crossover, and improving high-voltage performance. The latter two factors will result in high efficiency of a DMFC. It is expected

that the DMFC model development efforts will be directed less toward refining model accuracy and improving computational speed and more toward applying the models to invent new cell designs and pinpoint areas of improvement.

5. Solid Oxide Fuel Cells

A solid oxide fuel cell (SOFC) consists of two electrodes: anode and cathode, with a ceramic electrolyte between that transfers oxygen ions. A SOFC typically operates at a temperature between 700 and 1000 °C, at which temperature the ceramic electrolyte begins to exhibit sufficient ionic conductivity. This high operating temperature also accelerates electrochemical reactions; therefore, a SOFC does not require precious metal catalysts to promote the reactions. More abundant materials such as nickel have sufficient catalytic activity to be used as SOFC electrodes. In addition, the SOFC is more fuel-flexible than other types of fuel cells, and reforming of hydrocarbon fuels can be performed inside the cell. This allows use of conventional hydrocarbon fuels in a SOFC without an external reformer.

Planar SOFC systems have received much attention lately because of ease of manufacturing and higher performance as compared to tubular types.[188] Planar SOFCs are generally manufactured in three different configurations according to their operating temperatures. For cells operating around 1000 °C, the electrolyte-supported cell configuration is preferred. In this design, anode and cathode are very thin (i.e., 50 μm) and the electrolyte thickness is generally larger than 100 μm. The electrolyte ionic conductivity is a strong function of operating temperature in SOFCs. For SOFCs operating at lower operating temperatures, the ionic conductivity is lower and as such anode- or cathode-supported cell configurations are preferred. In the electrode-supported cell configuration, the electrolyte is usually very thin (i.e., 20 μm) and either anode or cathode is thick enough to serve as the supporting substrate for cell fabrication. The thickness of the supporting electrode varies between 0.3 and 1.5 mm, depending on the design. These three planar SOFC designs are sketched in Figure 42.[189]

For optimal design and operation of a SOFC, a fundamental and detailed understanding of transport and electrochemical kinetics is indispensable. Efforts are presently underway to understand the multiphysics and obtain the optimal design for SOFCs. For these purposes, a CFCD model, similar to those for PEFCs and DMFCs, becomes a valuable tool for design and operation of SOFCs.

5.1. SOFC Models

Unlike the comprehensive reviews provided in sections 3 and 4 for PEFC and DMFC, respectively, the present review on SOFC modeling will be brief and is not meant to be exhaustive. Instead, only major trends are indicated by way of representative studies.

For the purpose of modeling, consider a planar SOFC divided into anode gas channel, anode gas diffusion electrode, anode interlayer (active electrode), electrolyte, cathode interlayer (active electrode), cathode gas diffusion electrode, and cathode gas channel. The electrochemical reactions occur in the active regions of the porous electrodes (i.e., interlayers). In an SOFC, oxidant reduction occurs in the active cathode. The oxygen ions are then transported through the electrolyte, after which oxidation of the fuel occurs in the active anode by the following reactions.

Oxidation of fuel at the anode

$$H_2 + O^{2-} \rightarrow H_2O + 2e^-$$
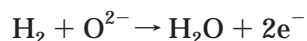
Reduction of oxidant at the cathode

$$\tfrac{1}{2}O_2 + 2e^- \rightarrow O^{2-}$$
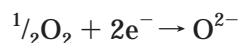
The anode is generally made of nickel/yttria-stabilized zirconia Cermet. The cathode is an LSM layer chemically expressed as $La_{1-x}Sr_xMnO_3$. The electrolyte is an Y_2O_3-doped zirconia called YSZ.

The activation overpotentials for both electrodes are high; therefore, the electrochemical kinetics of the both electrodes can be approximated by Tafel kinetics. The concentration dependence of exchange current density was given by Costamagna and Honegger.[190] The open-circuit potential of a SOFC is calculated via the Nernst equation.[190] The conductivity of the electrolyte, i.e., YSZ, is a strong function of temperature and increases with temperature. The temperature dependence of the electrolyte conductivity is expressed by the Arrhenius equation.[190]

Earlier modeling studies were aimed at predicting the current and temperature distributions,[188,190−192] as the nonuniform distributions contribute to stress formation, a major technical challenge associated with the SOFC system. Flow and multicomponent transport were typically simplified in these models that focused on SOFC electrochemistry. Recently, fundamental characteristics of flow and reaction in SOFCs were analyzed using the method of matched asymptotic expansions.[193−195]

With today's computing power and popular use of CFD codes, SOFC modeling is moving toward multiphysics, electrochemical-transport-coupled, and three-dimensional descriptions. Prinkey et al.[196] proposed a Fluent-based CFD model to describe reactant flow, transport, and electrochemical reaction in a SOFC. The charge transport was, however, simplified into an algebraic equation accounting for activation polarizations, electrolyte ohmic loss, and concentration polarizations. Moreover, the concentration polarizations were calculated empirically via a prescribed limiting current. This modeling framework is inconsistent in that the limiting current physically is the result of the mass-transport phenomena and thus should be calculated from the solution of species equations instead of being prescribed independently. Recknagle et al.,[197] on the other hand, employed STAR−CD code along with an electrochemistry module to simulate a SOFC with three flow configurations: cross-flow, co-flow, and counter-flow. The effects of cell flow configurations on the distribution of temperature, current, and reactant species were investigated. It was found that for similar fuel utilization and average cell temperature, the co-flow case had the most uniform temperature distribution and the smallest thermal gradients. This study, however, treated the positive electrode−electrolyte−negative electrode (PEN) as a single solid component. Such an approximation is inappropriate to model the latest generation of electrode-supported SOFC where mass diffusion through a thick anode or cathode constitutes a major limitation. Most recently, Ackmann et al.[198] performed a two-dimensional numerical study of mass and heat transport in planar SOFC with focus on elucidating the mass diffusion limitation across the thickness of electrodes as well as in the in-plane direction between the channel and interconnect rib areas. This model of Ackmann et al. also included methane/steam reforming and water−gas shift reaction in addition to the SOFC electrochemical kinetics.

A self-consistent SOFC model was developed based on the same single-domain modeling framework that has been applied to PEFC and DMFC, as elaborated above. This model of Pasaogullari and Wang[199] solves the continuum equations for conservation of mass, momentum, species, thermal energy, and electric charge along with electrochemical kinetics in anode and cathode of a SOFC. The governing equations for the SOFC model of Pasaogullari and Wang[199] were exactly the same as those in Table 1 except that water transport by either electro-osmotic drag or diffusion through the electrolyte becomes irrelevant. The species transport equation was solved for three species: H_2, O_2, and H_2O.[199] However, the model is applicable to multiple fuels such as H_2 and CO given that kinetic expressions for co-oxidation of H_2 and CO on Ni catalysts are provided. N_2 was considered as an inert gas in this model.

To illustrate typical simulation results from such multiphysics SOFC models, consider a co-flow and a cross-flow electrolyte-supported cell. The cross-flow geometry is of particular interest because of the complex transport phenomena offered in this cell configuration, a configuration able to provide detailed understanding of mass-transfer limitations. Structured, orthogonal meshes were used for all compu-
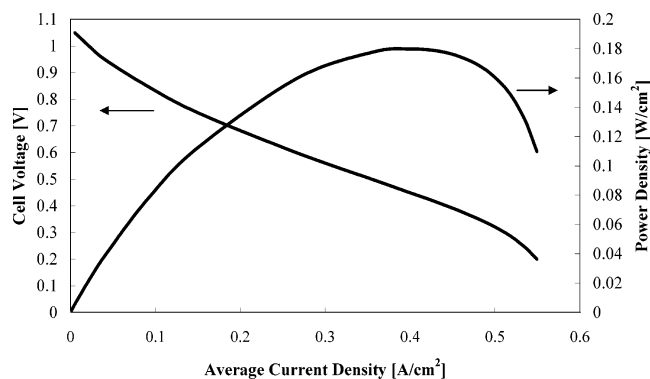
Figure 43. Calculated current−voltage characteristics and power density curve of electrolyte-supported co-flow SOFC at an operating temperature of 1000 °C and anode and cathode stoichiometry of 1.5 and 2.0 at 0.4 A/cm², respectively.[199]
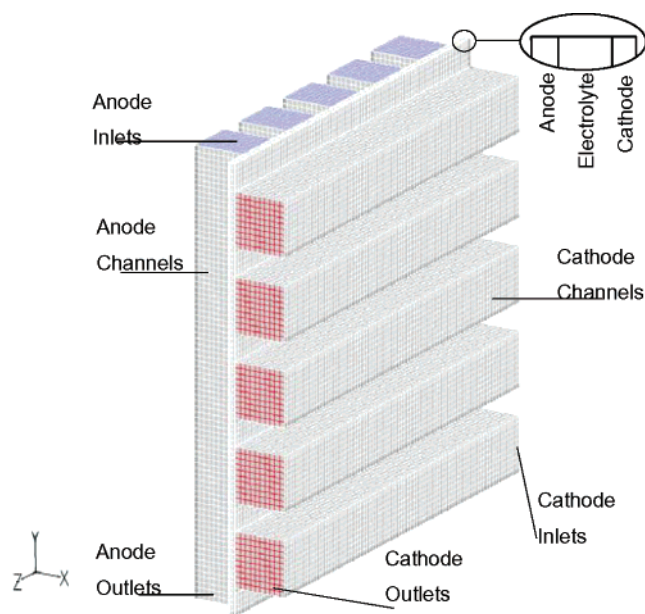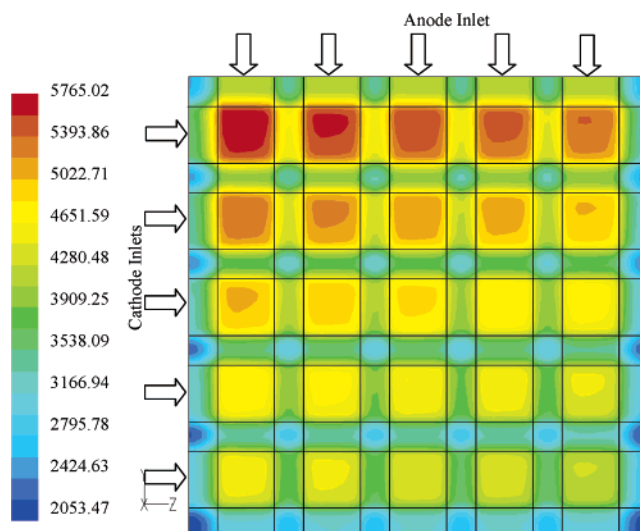

Figure 44. Geometry and mesh of a five-channel cross-flow electrolyte-supported SOFC.

Figure 45. Current distribution (A/m²) at a cell potential of 0.4 V in the five-channel cross-flow electrolyte-supported SOFC (A/m²) under anode and cathode stoichiometries of 1.5 and 2.0, respectively, and a cell temperature of 1000 °C.

tational meshing. It was found that a $80 \times 80 \times 35$ mesh is sufficient for 3-D, five-channel geometry.[199] It takes ~300 iterations to converge a 3-D simulation of the five-channel cross-flow geometry (i.e., 224 000 cells). Figure 43 shows a sample calculation of the polarization behavior of the co-flow cell.

To understand the cross-flow-transport characteristics in a planar SOFC, consider a five-channel cross-flow-type electrolyte-supported SOFC shown in Figure 44 and the simulated current distribution in this cell, shown in Figure 45.[199] It is clearly seen from Figure 45 that the regions facing the channels have much higher current density. This is clearly seen at the zones, where the corresponding anode and cathode gas channels meet. In those regions both of the electrodes receive enough reactant, thereby producing higher current. This 3-D calculation explicitly illustrates the effect of flow-field design on cell performance.

Experimental validation of SOFC models has been quite scarce. Khaleel and Selman[200] presented a comparison of 1-D electrochemical model calculations with experimental polarization curves for a range of

hydrogen concentrations in the anode feed. Clearly, this is an area requiring much attention in the future of SOFC modeling, and model validation at a detailed distribution level (e.g., against current and species distribution data) is equally essential.

5.2. Summary and Outlook

A single-domain, self-consistent formulation has been available to describe the electrochemistry, gas dynamics, and multicomponent transport in SOFC. Both Fluent and STAR−CD codes can be adapted for implementation of SOFC models. In addition to predicting the current−voltage characteristics, these CFD models provide valuable insight into the reactant and product distributions, current distribution, and fuel utilization, making it possible to analyze SOFC operation in detail. The latest SOFC models also have the energy equation built in to predict the temperature distribution. The temperature distribution can be coupled to stress analyses, thereby providing a comprehensive computer-aided engineering (CAE) tool for SOFC design and operation. The CFD models are easily extendable to include multiple fuels such as H_2 and CO. In such a case, co-oxidation of H_2 and CO on Ni catalyst must be considered following a similar approach already developed for PEFC in the presence of CO poisoning. Finally, The CFD-based SOFC models can be combined with internal reforming models on the anode. In such a situation, a catalytic chemical reaction is needed as well.

SOFC modeling is the simplest among all three systems reviewed in this paper, since a SOFC does not involve transport phenomena as complex as in a PEFC and DMFC. In addition, SOFC modeling can draw largely upon tremendous existing experiences from combustion and fuel-processing fields. Future directions of SOFC modeling research are toward (1) coupled modeling of SOFC and fuel reforming (whether external or internal), (2) comprehensive

modeling of direct hydrocarbon DOFC systems where spray and evaporation of liquid fuels play important roles, (3) model validation against detailed distribution data, and (4) direct numerical simulation of SOFC electrodes, similar to what is described in section 3.9, to establish a quantitative relationship of electrode microstructure and compositions with cell performance.

6. Closing Remarks

Automotive, stationary, and portable applications place an ever-increasing demand to develop advanced fuel cell technologies with high performance, low cost, and excellent durability. Computer-aided engineering is indispensable in this development process and can dramatically reduce the expensive and time-consuming trial-and-error experimentation currently required. The complexity of fuel cells requires many interacting physicochemical submodels in order for CFCD models to be successful. Therefore, a fundamental understanding of the electrochemical and transport processes in fuel cells continues to be necessary. This can be best achieved through a combination of fundamental modeling and detailed diagnostics, as shown in the present review. In addition, further developments in numerical algorithms will eventually allow the use of CFCD models in design, optimization, and control of fuel cell systems, thereby significantly accelerating the commercial deployment of fuel cell technologies.

Computational modeling of fuel cells is an important and physically rich subject. Despite emergence of significant experimental and modeling capabilities, much remains to be done before the knowledge of multiscale phenomena occurring in fuel cells can be directly utilized in cell design and product development. Further challenges and research directions have been pointed out at the end of each section for PEFC, DMFC, and SOFC. An upsurge of research activities in this field worldwide is expected in years to come.

7. Acknowledgments

8. References

(1) Kreuer, K. D. *J. Membr. Sci.* **2001**, *185*, 29.
(2) Paddison, S. J. In *Handbook of Fuel Cells*; Vielstich, W., Gasteiger, H. A., Lamm, A., Eds.; John Wiley and Sons Ltd.: England, 2003; Vol. 3, p 397.
(3) Koper, M. T. M. In *Handbook of Fuel Cells*; Vielstich, W., Gasteiger, H. A., Lamm, A., Eds.; John Wiley and Sons Ltd.: England, 2003; Vol. 2, p 348.
(4) Wang, C. Y. *Int. J. Transport Phenom.* **2001**, *3*, 131.
(5) Wang, C. Y. In *Handbook of Fuel Cells*; Vielstich, W., Gasteiger, H. A., Lamm, A., Eds.; John Wiley and Sons Ltd.: England, 2003; Vol. 3, p 337.
(6) Ju, H.; Wang, C. Y. *J. Electrochem. Soc.*, in press.
(7) Bird, R. B.; Stewart, W. E.; Lightfoot, E. N. *Transport Phenomena*, 2nd ed.; Wiley: New York, 2002.
(8) Newman, J. *Electrochemical Systems*, 2nd ed.; Prentice Hall: Englewood Cliffs, NJ, 1991.
(9) Patankar, S. V. *Numerical Heat Transfer and Fluid Flow*; Hemisphere Publishing Corp.: New York, 1980.
(10) Oran, E. S.; Boris, J. P. *Numerical Simulation of Reactive Flow*; Cambridge University Press: Cambridge, 2001.
(11) Wu, J.; Srinivasan, V.; Xu, J.; Wang, C. Y. *J. Electrochem. Soc.* **2002**, *149*, A1342.
(12) Pisani, L.; Murgia, G.; Valentini, M.; D'Aguanno, B. *J. Electrochem. Soc.* **2002**, *149*, A31.
(13) Pisani, L.; Murgia, G.; Valentini, M.; D'Aguanno, B. *J. Electrochem. Soc.* **2002**, *149*, A898.
(14) Meng, H.; Wang, C. Y. *J. Electrochem. Soc.* **2004**, *151*, A358.
(15) Meng, H.; Wang, C. Y. *Chem. Eng. Sci.* **2004**, *59*, 3331.
(16) Springer, T. E.; Zawodzinski, T. A.; Gottesfeld, S. *J. Electrochem. Soc.* **1991**, *138*, 2334.
(17) Zawodzinski, T. A.; Derouin, C.; Radzinsksi, S.; Sherman, R. J.; Smith, V. T.; Springer, T. E.; Gottesfeld, S. *J. Electrochem. Soc.* **1993**, *140*, 1041.
(18) Zawodzinski, T. A.; Springer, T. E.; Davey, J.; Jestel, R.; Lopez, C.; Valerio, J.; Gottesfeld, S. *J. Electrochem. Soc.* **1993**, *140*, 1981.
(19) Ren, X.; Springer, T. E.; Gottesfeld, S. *J. Electrochem. Soc.* **2000**, *147*, 92.
(20) Walsby, N.; Hietala, S.; Maunu, S. L.; Sundhold, F.; Kallio, T.; Sundholm, G. *J. Appl. Polym. Sci.* **2002**, *86*, 33.
(21) Feterko, P.; Hsing, I.-M. *J. Electrochem. Soc.* **1999**, *146*, 2049.
(22) Hinatsu, J. T.; Mizuhata, M.; Takenaka, H. *J. Electrochem. Soc.* **1994**, *141*, 1493.
(23) Zawodzinski, T. A.; Davey, J.; Valerio, J.; Gottesfeld, S. *Electrochim. Acta* **1995**, *40*, 297.
(24) Ren, X.; Gottesfeld, S. *J. Electrochem. Soc.* **2001**, *148*, A87.
(25) Ren, X.; Henderson, W.; Gottesfeld, S. *J. Electrochem. Soc.* **1997**, *144*, L267.
(26) Ise, M.; Kreuer, K. D.; Maier, J. *Solid State Ionics* **1999**, *125*, 213.
(27) Motupally, S.; Becker, A. J.; Weidner, J. W. *J. Electrochem. Soc.* **2000**, *147*, 3171.
(28) Parthasarathy, A.; Srinivasan, S.; Appleby, A. J. *J. Electrochem. Soc.* **1992**, *140*, 2178.
(29) Lee, S. J.; Mukerjee, J.; McBreen, Y.; Rho, W.; Kho, Y. T.; Lee, T. H. *Electrochim. Acta* **1998**, *43*, 3693.
(30) Gottesfeld, S.; Zawodzinski, T. A. In *Advances in Electrochemical Science and Engineering*; Tobias, C., Ed.; Wiley and Sons: New York, 1997; Vol. 5.
(31) Gasteiger, H. A.; Gu, W.; Makharia, R.; Mathias, M. F.; Sompalli, B. In *Handbook of Fuel Cells*; Vielstich, W., Gasteiger, H. A., Lamm, A., Eds.; John Wiley and Sons Ltd.: England, 2003; Vol. 3, p 594.
(32) Mathias, M. F.; Roth, J.; Flemming, J.; Lehnert, W. In *Handbook of Fuel Cells*; Vielstich, W., Gasteiger, H. A., Lamm, A., Eds.; John Wiley and Sons Ltd.: England, 2003; Vol. 3, p 517.
(33) Lim, C.; Wang, C. Y. *Electrochim. Acta* **2004**, *49*, 4149.
(34) Chapman, S.; Cowling, T. G. *Mathematical Theory of Non-Uniform Gases*; Cambridge University Press: Cambridge, 1951.
(35) Reid, R. C.; Prausnitz, J. M.; Poling, B. E. *The Properties of Gases and Liquids*; McGraw-Hill: New York, 1987.
(36) Singhal, S. C. *MRS Bull.* **2000**, 16.
(37) Minh, N. Q.; Takahashi, T. *Science and Technology of Ceramic Fuel Cells*; Elsevier: Amsterdam, 1995.
(38) Yokokawa, H. *Key Eng. Mater.* **1998**, *153*, 37.
(39) Virkar, A. V. *Introduction to Solid Oxide Fuel Cells (SOFC): Science and Technology*; Lecture notes from SOFC Workshop, National Energy Technology Laboratory (NETL), summer 2001.
(40) Todd, B.; Young, J. B. *J. Power Sources* **2002**, *110*, 186.
(41) Khee, R. J.; Rupley, F. M.; Miller, J. A. *The Chemkin Thermodynamic Data Base*; SAND87−8215B, UC-4; Sandia National Laboratories, Albuquerque, 1987.
(42) Prater, K. B. *J. Power Sources* **1994**, *51*, 129.
(43) *Handbook of Fuel Cells*; Vielstich, W., Gasteiger, H. A., Lamm, A., Eds.; John Wiley and Sons Ltd.: England, 2003; Vol. 3, Part 3.
(44) Bernardi, D. M.; Verbrugge, M. W. *AIChE J.* **1991**, *37*, 1151.
(45) Bernardi, D. M.; Verbrugge, M. W. *J. Electrochem. Soc.* **1992**, *139*, 2477.
(46) Springer, T. E.; Zawodzinski, T. A.; Gottesfeld, S. *J. Electrochem. Soc.* **1991**, *138*, 2334.
(47) Springer, T. E.; Wilson, M. S.; Gottesfeld, S. *J. Electrochem. Soc.* **1993**, *140*, 3513.
(48) Fuller, T. F.; Newman, J. *J. Electrochem. Soc.* **1993**, *140*, 1218.
(49) Nguyen, T.; White, R. E. *J. Electrochem. Soc.* **1993**, *140*, 2178.

(50) Yi, J. S.; Nguyen, T. V. *J. Electrochem. Soc.* **1999**, *146*, 38.

(51) Yi, J. S.; Nguyen, T. V. *J. Electrochem. Soc.* **1998**, *145*, 1149.

(52) Promislow, K.; Stockie, J. M. *SIAM J. Appl. Math.* **2001**, *62*, 180.

(53) Stockie, J. M.; Promislow, K.; Wetton, B. R. *Int J. Numer. Methods Fluids* **2003**, *41*, 577.

(54) Gurau, V.; Liu, H.; Kakac, S. *AIChE J.* **1998**, *44*, 2410.

(55) Um, S.; Wang, C. Y.; Chen, K. S. *J. Electrochem. Soc.* **2000**, *147*, 4485.

(56) Um, S.; Wang, C. Y. In *Proceedings of the ASME Heat Transfer Division*; Orlando, FL, 2000; Vol. 1, pp 19−25.

(57) Dutta, S.; Shimpalee, S.; Van Zee, J. W. *J. Appl. Electrochem.* **2000**, *30*, 135.

(58) Dutta, S.; Shimpalee, S.; Van Zee, J. W. *Int. J. Heat Mass Transfer* **2001**, *44*, 2029.

(59) Um, S.; Wang, C. Y. *J. Power Sources* **2004**, *125*, 40.

(60) Lee, W.-K.; Shimpalee, S.; Van Zee, J. W. *J. Electrochem. Soc.* **2003**, *150*, A341.

(61) Zhou, T.; Liu, H. *Int. J. Transport Phenom.* **2001**, *3*, 177.

(62) Berning, T.; Lu, D. M.; Djilali, N. *J. Power Sources* **2002**, *106*, 284.

(63) Mazumder, S.; Cole, J. V. *J. Electrochem. Soc.* **2003**, *150*, A1503.

(64) Ju, H.; Meng, H.; Wang, C. Y. *Int. J. Heat Mass Transfer*, submitted for publication.

(65) Wang, Y.; Wang, C. Y. *Int. J. Heat Mass Transfer*, submitted for publication.

(66) Wang, Y.; Wang, C. Y. *Electrochim. Acta*, in press.

(67) Pasaogullari, U.; Wang, C. Y. *203rd Electrochemical Society Meeting*, Paris, May 2003; Abstract 1190. Also *J. Electrochem. Soc.*, in press.

(68) Wang, Z. H.; Wang, C. Y.; Chen, K. S. *J. Power Sources* **2001**, *94*, 40.

(69) He, W.; Yi, J. S.; Nguyen, T. V. *AIChE J.* **2000**, *46*, 2053.

(70) Natarajan, D.; Nguyen, T. V. *J. Electrochem. Soc.* **2001**, *148*, 1324.

(71) Natarajan, D.; Nguyen, T. V. *J. Power Sources* **2003**, *115*, 66.

(72) You, L.; Liu, H. *Int. J. Heat Mass Transfer* **2002**, *45*, 2277.

(73) Mazumder, S.; Cole, J. V. *J. Electrochem. Soc.* **2003**, *150*, A1510.

(74) Berning, T.; Djilali, N. *J. Electrochem. Soc.* **2003**, *150*, A1598.

(75) Pasaogullari, U.; Wang, C. Y. *Electrochim. Acta*, in press.

(76) Wang, C. Y.; Gu, W. B. *J. Electrochem. Soc.* **1998**, *145*, 3407.

(77) Kaviany, M. *Principles of Heat Transfer in Porous Media*; Springer-Verlag: New York, 1991; p 598.

(78) Plumb, O. A. In *Handbook of Porous Media*; Vafai, K., Hadim, H. A., Eds.; Marcel Dekker: New York, 2000; p 754.

(79) Wang, C. Y.; Cheng, P. *Adv. Heat Transfer* **1997**, *30*, 93.

(80) Kulikovsky, A. A. *J. Electrochem. Soc.* **2003**, *150*, A1432.

(81) Wang, Y.; Wang, C. Y. Comparing variable density with constant density models for polymer electrolyte fuel cells. *ECEC Technical Report 2003-02*; Penn State University: University Park, PA, 2003. See also: Modeling polymer electrolyte fuel cells with large density and velocity changes. *J. Electrochem. Soc.*, in press.

(82) Berger, C. *Handbook of Fuel Cell Technology*; Prentice-Hall: New Jersey, 1968.

(83) Gu, W. B.; Wang, C. Y. *J. Electrochem. Soc.* **2000**, *147*, 2910.

(84) Okada, T.; Xie, G.; Gorseth, O.; Kjelstrup, S.; Nakamura, N.; Arimura, T. *Electrochim. Acta* **1998**, *43*, 3741.

(85) Okada, T.; Xie, G.; Meeg, M. *Electrochim. Acta* **1998**, *43*, 2141.

(86) Hsing, I.-M.; Futerko, P. *Chem. Eng. Sci.* **2000**, *55*, 4209.

(87) Janssen, G. J. M. *J. Electrochem. Soc.* **2001**, *148*, A1313.

(88) Janssen, G. J. M.; Overvelde, M. L. J. *J. Power Sources* **2001**, *101*, 117.

(89) Buchi, F.; Scherer, G. G. *J. Electrochem. Soc.* **2001**, *148*, A183.

(90) Prinkey, M. T.; Shahnam, M.; Rogers, W. A.; Gemmen, R. S. In *Proceedings of the 2002 Fuel Cell Seminar*; Palm Springs, CA, 2002; p 913.

(91) Um, S. Ph.D. Thesis, The Pennsylvania State University, 2002.

(92) Wohr, M.; Bolwin, K.; Schnurnberger, W.; Fischer, M.; Neubrand, W. *Int. J. Hydrogen Energy* **1998**, *23*, 213.

(93) Rowe, A.; Li, X. *J. Power Sources* **2001**, *102*, 82.

(94) Maggio, G.; Recupero, V.; Mantegazza, C. *J. Power Sources* **1996**, *62*, 167.

(95) Shimpalee, S.; Dutta, S. *Numerical Heat Transfer A* **2000**, *38*, 111.

(96) Costamagna, P. *Chem. Eng. Sci.* **2001**, *56*, 323.

(97) Meng, H.; Wang, C. Y. Multidimensional modeling of polymer electrolyte fuel cells under current density boundary condition. Submitted for publication.

(98) Ishikawa, M. Private communication, 2003.

(99) Qi, Z.; Kaufman, A. *J. Power Sources* **2002**, *109*, 469.

(100) Ju, H.; Wang, C. Y.; Cleghorn, S. J.; Beuscher, U. *J. Electrochem. Soc.*, submitted for publication.

(101) Baschuk, J. J.; Li, X. *J. Power Sources* **2000**, *86*, 181.

(102) Weisbrod, K. R.; Grot, S. A.; Vanderborgh, N. E. *Electrochem. Soc. Proc.* **1995**, *23*, 153.

(103) Nam, J. H.; Kaviany, M. *Int. J. Heat Mass Transfer* **2003**, *46*, 4595.

(104) Pasaogullari, U.; Wang, C. Y. *J. Electrochem. Soc.* **2004**, *151*, A399.

(105) Lim, C.; Wang, C. Y. Measurement of contact angles of liquid water in PEM fuel cell gas diffusion layer (GDL) by sessile drop and capillary rise methods. *Penn State University Electrochemical Engine Center (ECEC) Technical Report no. 2001-03*; Penn State University: State College, PA, 2001.

(106) Brown, C. J.; Pletcher, D.; Walsh, F. C.; Hammond, J. K.; Robinson, D. *J. Appl. Electrochem.* **1992**, *22*, 613.

(107) Cleghorn, S. J. C.; Derouin, C. R.; Wilson, M. S.; Gottesfeld S. *J. Appl. Electrochem.* **1998**, *28*, 663.

(108) Bender, G.; Wilson, M. S.; Zawodzinski, T. A. *J. Power Sources* **2003**, *123*, 163.

(109) Wieser, Ch.; Helmbold, A.; Gülzow, E. *J. Appl. Electrochem.* **2000**, *30*, 803.

(110) Stumper, J.; Campell, S.; Wilkinson, D.; Johnson, M.; Davis, M. *Electrochim. Acta* **1998**, *43*, 3773.

(111) Mench, M. M.; Wang, C. Y. *J. Electrochem. Soc.* **2003**, *150*, A79.

(112) Mench, M. M.; Wang, C. Y.; Ishikawa, M. *J. Electrochem. Soc.* **2003**, *150*, A1052.

(113) Noponen, M.; Mennola, T.; Mikkola, M.; Hottinen, T.; Lund, P. *J. Power Sources* **2002**, *106*, 304.

(114) Noponen, M.; Hottinen, T.; Mennola, T.; Mikkola, M.; Lund, P. *J. Appl. Electrochem.* **2002**, *32*, 1081.

(115) Brett, D.; Atkins, S.; Brandon, N. P.; Vesovic, V.; Vasileiadis, N.; Kucernaka, A. *Electrochem. Solid-State Lett.* **2003**, *6*, A63.

(116) Ren, X.; Gottesfeld, S. *J. Electrochem. Soc.* **2001**, *148*, A87.

(117) Janssen, G. J.; Overvelde, M. L. *J. Power Sources* **2001**, *101*, 117.

(118) Lee, W. K.; Van Zee, J. W.; Shimpalee, S.; Dutta, S. *Proc. ASME Heat Transfer Div.* **1999**, *1*, 339.

(119) Mench, M. M.; Dong, Q. L.; Wang, C. Y. *J. Power Sources* **2003**, *124*, 90.

(120) Yang, X. G.; Burke, N.; Wang, C. Y.; Tajiri, K.; Shinohara, K. *J. Electrochem. Soc.*, in press.

(121) Mench, M. M.; Burford, D.; Davis, T. In *Proceedings of the 2003 International Mechanical Engineering Congress and Exposition*; Washington, D.C., ASME, Nov 2003.

(122) Bellows, R. J.; Lin, M. Y.; Arif, M.; Thompson, A. K.; Jacobsob, D. *J. Electrochem. Soc.* **1999**, *146*, 1099.

(123) Geiger, A. B.; Tsukada, A.; Lehmann, E.; Vontobel, P.; Wokaun, A.; Scherer, G. G. *Fuel Cells* **2002**, *2*, 92.

(124) Tuber, K.; Pocza, D.; Hebling, C. *J. Power Sources* **2003**, *124*, 403.

(125) Yang, X. G.; Zhang, F. Y.; Lubawy, A.; Wang, C. Y. *Electrochem. Solid-State Lett.*, in press.

(126) Springer, T. E.; Gottesfeld, S. In *Modeling of Batteries and Fuel Cells*; White, R. E., Ed.; 1991; Electrochemical Society Proc. *91−10*, p 197.

(127) Perry, M. L.; Newman, J.; Cairns, E. J. *J. Electrochem. Soc.* **1998**, *145*, 5.

(128) Eikerling, M.; Kornyshev, A. A. *J. Electroanal. Chem.* **1998**, *453*, 89.

(129) Jaouen, F.; Lindbergh, G.; Sundholm, G. *J. Electrochem. Soc.* **2002**, *149*, A448.

(130) Pisani, L.; Valentini, M.; Murgia, G. *J. Electrochem. Soc.* **2003**, *150*, A1558.

(131) Wang, G. Q.; Wang, C. Y. Presented at 204th Electrochemical Society Meeting, Orlando, FL, Oct 2003.

(132) Halpert, G.; Narayanan, S. R.; Valdez, T.; Chun, W.; Frank, H.; Kindler, A.; Surampudi, S.; Kosek, J.; Cropley, C.; LaConti, A. In *Proceedings of the 32nd Intersociety Energy Conversion Engineering Conference*; AIChE: New York, 1997; Vol. 2, p 774.

(133) Baldauf, M.; Preidel, W. *J. Power Sources* **1999**, *84*, 161.

(134) Ren, X.; Zelenay, P.; Thomas, S.; Davey, J.; Gottesfeld, S. *J. Power Sources* **2000**, *86*, 111.

(135) Scott, K.; Taama, W. M.; Argyropoulos, P. *Electrochim. Acta* **1999**, *44*, 3575.

(136) Scott, K. In *Handbook of Fuel Cells*; Vielstich, W., Gasteiger, H. A., Lamm, A., Eds.; John Wiley and Sons Ltd.: England, 2003; Vol. 1, p 70.

(137) Murgia, G.; Pisani, L.; Shukla, A. K.; Scott, K. *J. Electrochem. Soc.* **2003**, *150*, A1231.

(138) Mench, M.; Boslet, S.; Thynell, S.; Scott, J.; Wang, C. Y. In *Direct Methanol Fuel Cells*; The Electrochemical Society Proceedings Series: Pennington, NJ, 2001.

(139) Lim, C.; Wang, C. Y. *J. Power Sources* **2003**, *113*, 145.

(140) Lu, G. Q.; Wang, C. Y.; Yen, T. J.; Zhang, X. *Electrochim. Acta* **2004**, *49*, 821.

(141) Yen, T. J.; Fang, N.; Zhang, X.; Lu, G. Q.; Wang, C. Y. *Appl. Phys. Lett.* **2003**, *83*, 4056.

(142) Gottesfeld, S.; Wilson, M. S. In *Energy Storage Systems for Electronics Devices*; Osaka, T., Datta, M., Eds.; Gordon and Breach Science Publishers: Singapore, 2000; p 487.

(143) Lamy, C.; Leger, J.-M.; Srinivasan, S. In *Modern Aspects of Electrochemistry*; Bockris, J. O'M, Conway, B. E., White, R. E., Eds.; Kluwer Academic/Plenum Publishers: New York, 2001; p 53.

(144) Arico, A. S.; Srinivasan, S.; Antonucci, V. *Fuel Cells* **2001**, *1*, 133.

(145) Neergat, M.; Friedrich, K. A.; Stimming, U. In *Handbook of Fuel Cells*; Vielstich, W., Gasteiger, H. A., Lamm, A., Eds.; John Wiley and Sons Ltd.: England, 2003; Chapter 63, p 856.

(146) Narayanan, S. R.; Valdez, T. I.; Rohatgi, N. In *Handbook of Fuel Cells*; Vielstich, W., Gasteiger, H. A., Lamm, A., Eds.; John Wiley and Sons Ltd.: England, 2003; Chapter 65, p 894.

(147) Müller, J.; Frank, G.; Colbow, K.; Wilkinson, D. In *Handbook of Fuel Cells*; Vielstich, W., Gasteiger, H. A., Lamm, A., Eds.; John Wiley and Sons Ltd.: England, 2003; Chapter 62, p 847.

(148) Wasmus, S.; Kuver, A. *J. Electroanal. Chem.* **1999**, *461*, 14.

(149) Lin, W. F.; Wang, J. T.; Savinell, R. F. *J. Electrochem. Soc.* **1997**, *144*, 1917.

(150) Hamnett, A. *Catal. Today* **1997**, *38*, 445.

(151) Thomas, S. C.; Ren, X.; Gottesfeld, S. *J. Electrochem. Soc.* **1999**, *146*, 4354.

(152) Liu, L.; Pu, C.; Viswanathan, R.; Fan, Q.; Liu, R.; Smotkin, E. S. *Electrochim. Acta* **1998**, *43*, 3657.

(153) Hayden, E. *Catal. Today* **1997**, *38*, 473.

(154) Page, T.; Johnson, R.; Hormes, J.; Noding, S.; Rambabu, B. *J. Electroanal. Chem.* **2000**, *485*, 34.

(155) Arico, S.; Creti, P.; Modica, E.; Monforte, G.; Baglio, V.; Antonucci, V. *Electrochim. Acta* **2000**, *45*, 4319.

(156) Ravikumar, M. K.; Shukla, A. K. *J. Electrochem. Soc.* **1996**, *143*, 2601.

(157) Narayanan, S. R.; Frank, H.; Jeffries-Nakamura, B.; Smart, M.; Chun, W.; Halpert, G.; Kosek, J.; Cropley, C. In *Proton Conducting Membrane Fuel Cells I*; Gottesfeld, S., Halpert, G., Landgrebe, A., Eds.; The Electrochemical Society Proceedings Series: Pennington, NJ, 1995; PV 95−23, p 278.

(158) Ren, X.; Zawodzinski, T. A.; Uribe, F.; Dai, H.; Gottesfeld, S. In *Proton Conducting Membrane Fuel Cells I*; Gottesfeld, S., Halpert, G., Landgrebe, A., Eds.; The Electrochemical Society Proceedings Series: Pennington, NJ, 1995; PV 95−23, p 284.

(159) Ren, X.; Springer, T. E.; Zawodzinski, T. A.; Gottesfeld, S. *J. Electrochem. Soc.* **2000**, *147*, 466.

(160) Valdez, T. I.; Narayanan, S. R. In *Proton Conducting Membrane Fuel Cells II*; Gottesfeld, S., Fuller, T. F., Halpert, G., Eds.; The Electrochemical Society Proceedings Series: Pennington, NJ. 1998; PV 98−27, p 380.

(161) Wang, J. T.; Wasmus, S.; Savinell, R. F. *J. Electrochem. Soc.* **1996**, *143*, 1233.

(162) Kauranen, P. S.; Skou, E. *J. Electroanal. Chem.* **1996**, *408*, 189.

(163) Pan, Y. Ph.D. Thesis, The Pennsylvania State University, 2004.

(164) Peled, E.; Blum, A.; Aharon, A.; Philosoph, M.; Lavi, Y. *Electrochem. Solid-State Lett.* **2003**, *6*, A268.

(165) Kelley, S. C.; Deluga, G. A.; Smyrl, W. H. *AIChE J.* **2002**, *48*, 1071.

(166) Mench, M. M.; Wang, Z. H.; Bhatia, K.; Wang, C. Y. In *Proceedings of IMECE2001*, Vol. 3, ASME, New York, 2001.

(167) Pavio, J.; Bostaph, J.; Fisher, A.; Hallmark, J.; Mylan, B. J.; Xie, C. G. *Adv. Microelectron.* **2002**, *29*, 1.

(168) Dyer, C. K. *J. Power Sources* **2002**, *106*, 31.

(169) Lee, S. J.; Chang-Chien, A.; Cha, S. W.; O'Hayre, R.; Park, Y. I.; Saito, Y.; Prinz, F. B. *J. Power Sources* **2002**, *112*, 410.

(170) Scott, K.; Argyropoulos, P.; Sundmacher, K. *J. Electroanal. Chem.* **1999**, *477*, 97.

(171) Sundmacher, K.; Scott, K. *Chem. Eng. Sci.* **1999**, *54*, 2927.

(172) Argyropoulos, P.; Scott, K.; Taama, W. M. *J. Appl. Electrochem.* **2000**, *30*, 899.

(173) Baxter, S. F.; Battaglia, V. S.; White, R. E. *J. Electrochem. Soc.* **2000**, *146*, 437.

(174) Wang, J.; Savinell, R. F. In *Electrode Materials and Processes for Energy Conversion and Storage*; Srinivasan, S., Macdonald, D. D., Khandkar, A. C., Eds.; The Electrochemical Society Proceedings Series: Pennington, NJ, 1994; PV 94−23, p 326.

(175) Kulikovsky, A. A.; Divisek, J.; Kornyshev, A. A. *J. Electrochem. Soc.* **2000**, *147*, 953.

(176) Kulikovsky, A. A. *J. Appl. Electrochem.* **2000**, *30*, 1005.

(177) Dohle, H.; Divisek, J.; Jung, R. *J. Power Sources* **2000**, *86*, 469.

(178) Meyers, J. P.; Newman J. *J. Electrochem. Soc.* **2002**, *149*, A710.

(179) Meyers, J. P.; Newman J. *J. Electrochem. Soc.* **2002**, *149*, A718.

(180) Meyers, J. P.; Newman J. *J. Electrochem. Soc.* **2002**, *149*, A729.

(181) Nordlund J.; Lindbergh G. *J. Electrochem. Soc.* **2002**, *149*, A1107.

(182) Wang, Z. H.; Wang, C. Y. *J. Electrochem. Soc.* **2003**, *150*, A508.

(183) Divisek J.; Fuhrmann, J.; Gartner, K.; Jung R. *J. Electrochem. Soc.* **2003**, *150*, A811.

(184) Murgia, G.; Pisani, L.; Shukla, A. K.; Scott, K. *J. Electrochem. Soc.* **2003**, *150*, A1231.

(185) Apgyropoulos, R.; Scott, K.; Taama, W. M. *Electrochim. Acta* **1999**, *44*, 3575.

(186) Apgyropoulos, R.; Scott, K.; Taama, W. M. *J. Appl. Electrochem.* **1999**, *29*, 661.

(187) Lu, G. Q.; Wang, C. Y. *J. Power Sources*, **2004**, *134*, 33.

(188) Yakabe, H.; Ogiwara, T.; Hishinuma, M.; Yasuda, I. *J. Power Sources* **2001**, *102*, 144.

(189) Singhal, S. C. *Presentation at INDO−US Fuel Cell Workshop*; Washington, D.C., 2002.

(190) Costamagna, P.; Honegger, K. *J. Electrochem. Soc.* **1998**, *145*, 3995.

(191) Ahmed, S.; McPheeter, C.; Kumar, R. *J. Electrochem. Soc.* **1991**, *138*, 2712.

(192) Bessette, N. F., II; Wepfer, W. J.; Winnick, J. *J. Electrochem. Soc.* **1995**, *142*, 3792.

(193) Billingham, J.; King, A. C.; Copcutt, R. C.; Kendall, K. *SIAM J. Appl. Math.* **1999**, *60*, 574.

(194) Cooper, R. J.; Billingham, J.; King, A. C. *J. Fluid Mech.* **2000**, *411*, 233.

(195) King, A. C.; Billingham, J.; Cooper, R. J. *Combust. Theory Model.* **2001**, *5*, 639.

(196) Prinkey, M.; Gemmen, R. S.; Rogers, W. A. In *Proceedings of IMECE 2001*; ASME: New York, 2001; Vol. 369−4, p 291.

(197) Recknagle, K. P.; Williford, R. E.; Chick, L. A.; Rector, D. R.; Khaleel, M. A. *J. Power Sources* **2003**, *113*, 109.

(198) Ackmann, T.; Haart, L. G. J. de; Lehnert, W.; Stolten, D. *J. Electrochem. Soc.* **2003**, *150*, A783.

(199) Pasaogullari, U.; Wang, C. Y. *Electrochem. Soc. Proc.* **2003**, *2003−07*, 1403.

(200) Khaleel, M. A.; Selman, J. R. In *High-Temperature Solid Oxide Fuel Cells−Fundamentals, Design and Applications*; Singhal, S. C., Kendall, K., Eds.; Elsevier Ltd.: Oxford, U.K., 2003; p 293.